Karolina Sokołowska

Study of Water-Soluble p-MBA-Protected Gold Nanoclusters and Their Superstructures

UNIVERSITY OF JYVÄSKYLÄ

FACULTY OF MATHEMATICS
AND SCIENCE

Karolina Sokołowska

Study of Water-Soluble
p-MBA-Protected Gold Nanoclusters
and Their Superstructures

Esitetään Jyväskylän yliopiston matemaattis-luonnontieteellisen tiedekunnan suostumuksella
julkisesti tarkastettavaksi yliopiston Ylistönrinteen salissa YlistöKem4
joulukuun 13. päivänä 2019 kello 12.

Academic dissertation to be publicly discussed, by permission of
the Faculty of Mathematics and Science of the University of Jyväskylä,
in Ylistönrinne, auditorium YlistöKem4, on December 13, 2019 at 12 o'clock noon.

JYVÄSKYLÄN YLIOPISTO
UNIVERSITY OF JYVÄSKYLÄ

JYVÄSKYLÄ 2019

Editors

Tanja Lahtinen

Department of Chemistry, University of Jyväskylä

Timo Hautala

Open Science Centre, University of Jyväskylä

This is a printout of the original online publication.

ABSTRACT

The development of gold nanoclusters has made remarkable progress enriching the research field of nanomaterial science. The breakthroughs in synthetic chemistry enable the preparation of functional materials using gold nanoclusters. The assembly of gold nanoclusters into well-defined structures creates a system with new optical and electronic properties and functionalities, often sensitive to single atom or single electron in the system. Assembly of superstructures with molecular precision requires not only mastering the size and structural uniformities of building blocks but also understanding reaction kinetics and the interplay between competing reaction mechanisms. In the light of this, a robust synthesis of covalently linked nanoscale constructs from gold nanoclusters with atomically precise structures was developed, using common thiolation chemistry. The generality of the synthesis was proven by using various molecules connecting the particles, producing in high yield a large number of geometrical structures of linked gold clusters. The successful gel electrophoresis separation of dimers, trimers, and tetramers allowed detailed characterization and systematic studies of reaction mechanism of the created systems. Multimers of linked structures exhibit additional transitions in their UV-vis spectrum at 630 nm and 810 nm, indicating the presence of hybridized localized surface plasmon resonance (LSPR) modes. Nearly constant distances observed in transmission electron microscope (TEM) between singular gold clusters and the analysis of the oligomer yields supported with MD simulations suggest that gold nanoclusters are covalently bound by formation of singular molecular bridges. The molecular bridge is most likely formed by formation of an S-S bond between the terminal sulfurs of two (or more) dithiols connecting the particles. The successful disulfide bonding was also observed spectroscopically by X-ray photoelectron (XPS) and electron energy-loss spectroscopy (EELS). The scanning electron microscope (STEM) combined with EELS experiment gives spatial insight into the linked structures. The measurements confirm the molecular bridge between clusters by producing images with chemical contrast indicating the presence of molecules between particles. This achievement of making well-defined metallic nanoscale superstructures allows detailed engineering of the materials with atomic precision.

Keywords: Gold nanocluster, Covalent linking, $Au_{102}(p\text{-MBA})_{44}$,
para-mercaptobenzoic acid, Transmission electron microscope

Author   Karolina Sokołowska
                    Department of Chemistry
                    Nanoscience Center
                    University of Jyväskylä
                    Jyväskylä, Finland
                    karolina.x.sokolowska@jyu.fi

Supervisors   Adjunct Professor Tanja Lahtinen
                    Department of Chemistry
                    Nanoscience Center
                    University of Jyväskylä
                    Jyväskylä, Finland
                    tanja.m.lahtinen@jyu.fi

                    Dr. Lauri Lehtovaara
                    Department of Chemistry
                    Nanoscience Center
                    University of Jyväskylä
                    Jyväskylä, Finland
                    lauri.lehtovaara@gmail.com

Reviewers   Professor Tatsuya Tsukuda
                    Department of Chemistry
                    University of Tokyo
                    Tokyo, Japan
                    tsukuda@chem.s.u-tokyo.ac.jp

                    Adjunct Professor Nonappa
                    Department of Bioproducts and Biosystems
                    Aalto University School of Chemical Engineering
                    Helsinki, Finland
                    nonappa@aalto.fi

Opponent   Associate Professor Jianping Xie
                    Department of Chemistry and Biomolecular Engr.
                    National University of Singapore
                    Singapore
                    chexiej@nus.edu.org

PREFACE

My journey towards this book has started long ago, at the early stage of my undergraduate studies at the Department of Chemistry, University of Jyväskylä. There are many people who helped me at various stages of my research to achieve this milestone and to whom I owe a lot of gratitude and appreciation. Therefore, I would like to thank all of you. I am glad I had a chance to be a part of this community, learn from working with others in multidisciplinary projects and make choices that would not have been possible otherwise.

First and foremost, I would like to thank my main supervisor Adjunct Professor Tanja Lahtinen who guided me through the process of developing confidence as an academic. It has been a pleasure to work with Tanja, and never need to worry that something is going to be missed. I want to send my gratitude to Dr.Lauri Lehtovaara, my co-supervisor for coaching me through the project with complementary expertise and for his inspiration and never-ending scientific excitement. In particular, I would like to thank Eero Hulkko for spending all the extra time and effort in helping me with research, for encouragement, friendship and being a role model in many ways. I also want to acknowledge the staff at the NSC and Aalto University Nanomicroscopy Center for helping me with training, instruments and technical support.

This work could not have been done without the collaboration with other researchers. Thanks go to my collaborators who helped me to answer the questions and contributed their ideas to this work. I am also grateful that I had support and the possibility to always ask for help from my colleague Satu Mustalahti.

I could not work with a full throttle all these years without having closest people around. From the bottom of my heart, I would like to thank Ville for being present at every little stage of my career; patience, endless (scientific and other) support, and laughter every day. I also appreciate the debates about my scientific problems with my friends and family. Their interest in my work (sometimes forced) really kept me motivated. Thanks to Nisha and Ewa for being such fun lunch mates and your friendship. Thanks to all the NSC people and colleagues for many wonderful moments.

I hope you enjoy reading my thesis.

Jyväskylä, December 13th 2019

Karolina Sokołowska

LIST OF INCLUDED ARTICLES

I   Tanja Lahtinen, Eero Hulkko, Karolina Sokołowska, Tiia-Riikka Tero, Ville Saarnio, Johan Lindgren, Mika Pettersson, Hannu Häkkinen and Lauri Lehtovaara, Covalently Linked Multimers of Gold Nanoclusters $Au_{102}(p\text{-MBA})_{44}$ and $Au_{\sim250}(p\text{-MBA})_{n}$, *Nanoscale*, **2016**, 8, 18665–18674.

II   Karolina Sokołowska, Eero Hulkko, Lauri Lehtovaara, and Tanja Lahtinen, Dithiol-Induced Oligomerization of Thiol-Protected Gold Nanoclusters, *Journal of Physical Chemistry C,* **2018,** 122, 12524−12533.

III   Karolina Sokołowska, Sami Malola, Manu Lahtinen, Ville Saarnio, Perttu Permi, Katariina Koskinen, Matti Jalasvuori, Hannu Häkkinen, Lauri Lehtovaara and Tanja Lahtinen, Towards Controlled Synthesis of Water-Soluble Gold Nanoclusters: Synthesis and Analysis, *Journal of Physical Chemistry C,* **2019**, 123, 2602−2612.

IV   Karolina Sokołowska, Zhongyue Luan, Eero Hulkko, Christoph Rameshan, Noelia Barrabés, Vartkess Ara Apkarian and Tanja Lahtinen, Chemically Selective Imaging of Individual Bonds Through Scanning Electron Energy Loss Spectroscopy: Disulfide Bridges linking Gold Nanoclusters, *Submitted manuscript.*

Author's contribution

The author is the primary author of papers **III** and **IV** and she was the primary contributor to papers **I** and **II**. She carried out all of the synthetic work presented in papers **I, II, III** and **IV**. The author contributed to UV-vis spectroscopy analysis in paper **I**, performed TEM in papers **I, II** and **III** and subsequent analyses of the results in papers **I**, **II** and **III** and **IV**. The author has performed UV-vis spectroscopy, scanning method analysis, contributed to development of scanning approach, and development of theory, presented in papers **II** and **III**.

ABBREVIATIONS

MPC	Monolayer-protected cluster
NC	Nanocluster
NP	Nanoparticle
m-MBA	*meta*-mercaptobenzoic acid
p-MBA	*para*-mercaptobenzoic acid
PET	Phenylethylthiolate, HSC_2H_4Ph
ButSH	Butanethiol
MPA	Mercaptopropionic acid
PAGE	Polyacrylamide gel electrophoresis
TEM	Transmission electron microscopy
STEM	Scanning transmission electron microscopy
EELS	Electron energy-loss spectroscopy
EDX	Energy Dispersive X-ray spectroscopy
NMR	Nuclear magnetic resonance
ESI	Electrospray ionization
UV	Ultra-violet
vis	Visible
TGA	Thermogravimetric analysis
XRD	X-ray diffraction
PXRD	Powder X-ray diffraction
XPS	X-ray photoelectron spectroscopy
SEC	Size exclusion chromatography
MD	Molecular dynamics
FCC	Face centered-cubic
DFT	Density function theory
MD	Molecular dynamics
LSPR	Localized surface plasmon resonance
tCTP	Tunneling charge-transfer plasmon
HOMO	Highest occupied molecular orbital
LUMO	Lowest unoccupied molecular orbital

CONTENTS

1 INTRODUCTION

In the bulk state, gold is recognized as a shiny, chemically inactive metal, which does not rust or tarnish, has a face-cubic structure and melts at 1336 K.[1] Gold has been used as a symbol of wealth and power and shape the course of human history. At nanoscale gold´s behavior differs substantially when compared to its bulk counterpart. As the relative number of surface atoms is increased, the reactivity of the material is significantly affected. Nanoscale gold has a distinctly different structure, bonding characteristics and therefore different chemical and physical properties.

In modern nanotechnology, gold is being researched in a form of nanoparticles and nanoclusters at the dimensions between approximately 1 to 100 nm. Gold nanoparticles represent a different form of matter both from bulk form and molecular structures. These materials are made by varying the number of metal atoms and can be made from a variety of elements, including gold. In fact, gold nanoparticles and their absorption properties are not new and they have been used for centuries, for example to make color stained glasses.[2,3] The recent leaps in microscopy and synthetic chemistry have given a lot of possibilities to better understand the phenomena of these systems.

A nanocluster is composed of small number of gold atoms, typically measuring less than 2 nm. In comparison to nanoparticles, they do have distinctive features separating them from other materials.[4] They are well-defined, atomically precise objects. In many nanoscopic systems, atomic precision is nearly impossible to achieve due to sheer size of the system and inability to accurately control the molecules forming the nanostructures. In this regard, nanoclusters are one of the largest atomically defined molecules. The unusual features and distinctive properties of nanoclusters became a subject of considerable interest in fundamental science and life-science application. Given the fact that most of the unusual properties of nanoclusters are closely related to their composition, producing a homogeneous sample with atomic precision and customization of the properties to achieve desired function and good performance is crucial.

The core idea of my work presented in this thesis was to develop a robust synthesis to covalently link individual atomically precise thiolate-protected gold nanoclusters and study the properties of newly developed systems. To understand the optical phenomena of a completely novel class of atomically precise nanomaterials, detailed knowledge of electronic and atomic structures and the forces governing the formation mechanism of the system is necessary. Therefore, the study presented here is an experimental work of nanoclusters with special emphasis on surface modification methods, allowing detailed engineering of these materials, which have potential for use with molecular electronics and sensing applications. The experimental outcomes in this thesis are supported with complementary theoretical work, providing an explanation to a scale unreachable in the observations.

2 SELECTED PROPERTIES OF GOLD NANOCLUSTERS

Gold nanoclusters (NCs) are small (usually < 2 nm) nanoparticles composed of a metallic core varying from a few to less than a few hundred metal atoms.[5] They constitute the special class of materials, mostly due to their unusual properties, which can be tuned as a function of nanocluster size and composition. This behavior is significantly different from bulk or atomic structures.[6,7] The structures of clusters divide them into two size regimes, depending on the number of atoms they contain and hence their size, as shown in Figure 1. The structure ranges from small more molecular-like species with quantized electronic transitions[7] to larger more nanoparticle-like clusters with hundreds of metal atoms,[8] exhibiting localized surface plasmon resonances (LSPR).[4,6,8,9]
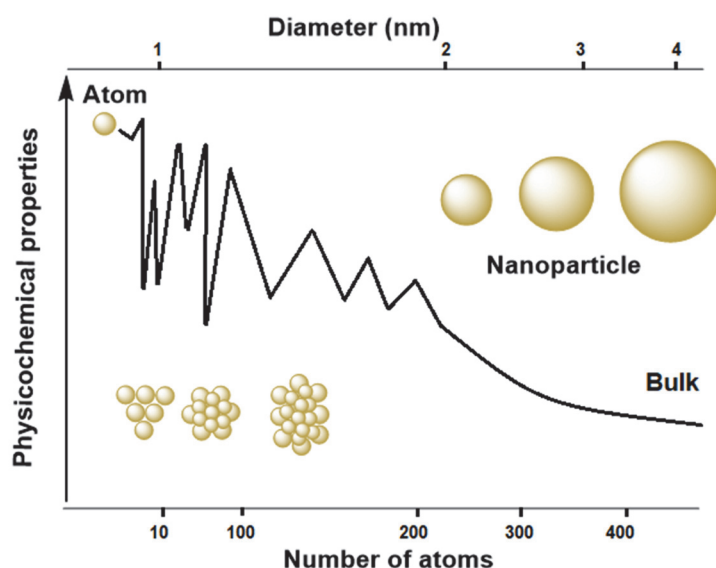

FIGURE 1   A graph highlighting the transition from a single gold atom, to a gold nanocluster, and finally to a gold nanoparticle dictated by the number of constituent atoms.[4]

For the fundamental study of many phenomena in nanoscale systems, gold nanoclusters are an ideal class of compounds due to their accurately known atomic structures.[6] They are extremely important as prototypes for a deepening understanding of larger particle systems.[8] Due to limited size and known atomic precision, they can be modeled with ab initio (DFT) level of theory to study evolvement of the bulk properties from the properties of individual atoms.[10]

Gold nanoclusters have garnered a lot of interest due to the unique properties, which can change radically by changing the size, shape, surface chemistry, or aggregation state. Even a minor change in the system, such as the addition of a single atom, may lead to the new features.[6,11] Because of their entirely different behavior, they hold a potential for a wide range of applications.[6] In fact, they have already been used in several high technology applications such as sensory probes, therapeutic agents, and drug delivery in biological and medical applications, electronic conductors and catalysis.[12,13]

2.1 Thiolate-protected gold nanoclusters

The stability of gold nanoclusters is typically enhanced by adding a protective ligand-layer, consisting of organic molecules or polymers on the gold core surface.[14,15] The metal-core surface is commonly passivated by molecules such as thiolates, selenolates, tellurolates or phosphines.[8,4,16,17] The ligand covalently binds to the cluster surface, protecting the metallic core from aggregation and forming an electronically stable system. Such species are commonly called monolayer-protected gold nanoclusters (MPCs).[18] The strong gold-thiol interaction plays an important role in structural stability of thiolate protected nanoclusters, yielding many stable nanocluster sizes.[7,19,20] In this thesis, gold NCs protected by thiolates are studied.

The studies of thiol-protected gold nanoclusters were initiated by the synthetic work of Brust and Schiffrin and the detection of atomically precise species by Whetten et al. in the late 1990s.[21,22] The chemical composition of stable, glutathione protected atomically precise species of Au_n clusters (n=10-39) was determined in 2005 by electrospray ionization (ESI) mass spectrometry.[15] A significant impact on the nanocluster field was made by first single-crystal X-ray structure determination of water-soluble $Au_{102}(p\text{-MBA})_{44}$-cluster.[23] This work revealed a unique atomistic structure and geometry of the thiolate-protected clusters, opening the field to DFT calculations and theoretical structural prediction of water-soluble gold nanoclusters.[20,24–27]

The recent progress in synthetic methods of gold MPCs made it possible to control the size and dispersity of the products.[28–33] This is achieved by development of synthetic *one-pot-for-one-size* synthesis, in addition to many size-focusing methods yielding monodisperse particles.[5,34] So far, more than 30 atomically precise thiolate cluster sizes ranging from Au_{15} to Au_{333} have been synthesized by the method introduced by Brust and Schiffrin.[4,34] $Au_{25}(SR)_{18}$ was one of the earliest discovered clusters. Since then the research has revealed

several stable sizes, including $Au_{36}(SR)_{24}$, $Au_{38}(SR)_{24}$, $Au_{55}(SR)_{31}$, $Au_{68}(SR)_{32}$, $Au_{102}(SR)_{44}$, $Au_{130}(SR)_{50}$, $Au_{144}(SR)_{60}$.[34] Water-soluble clusters are commonly passivated by, *para-* or *meta-* mercaptobenzoic acids (MBA), glutathione (GSH) or mercaptopropionic acid (MPA).

The ligand layer not only coats the cluster metal core preventing two nanoclusters to come into contact, but it also determines the interaction of the cluster with the environment. Therefore, it participates in cluster's solubility and controls its reactivity. For water-soluble clusters, biocompatibility is of special advantage in many applications.[35–37] One of the benefits of the ligand shell is the possibility to functionalize it. The protective layer can be modified, conjugated with various molecules or used for site-specific covalent or non-covalent binding. For example, Au_{102}(*p*-MBA)$_{44}$-cluster was used as a contrast agent in the virus imaging.[38,39] Engineering the nanocluster surface provides new functionality and enables tuning the properties of the original cluster.[4,40–43] Surface modification approaches have been used to assemble gold nanoclusters together, forming a functional nanocluster-based material with tunable plasmonic and mechanical properties.[42,43]

2.1.1   General properties and applications

The structural determination of water-soluble Au_{102}(*p*-MBA)$_{44}$-cluster, and later several other sizes with different protecting ligands, have advanced the field greatly, utilizing the remarkable properties and stability of MPCs.[5,20,24,25,44–49] General structures of gold MPCs consist of an inner gold core, protected by a gold-sulfur layer and an outermost protecting surface ligand layer.[50,51] The inner gold core is usually metallic with the formal charge 0. In the protecting gold-sulfur layer, gold atoms have a formal charge +1 and sulfur atoms -1. The gold-sulfur motifs have often different geometries and arrangements on the gold core surface. The structural arrangement, where the metallic gold core is covered by additional layers of gold-sulfur motifs, is referred to as the divide and protect model.[51] The outer protecting ligand layer consists of organic molecules, for example, water-soluble Au_{102} or Au_{146}-clusters protected by *p*-mercaptobenzoic acid or Au_{68} and Au_{144} protected by *m*-mercaptobenzoic acid.[32,52,53]

The geometry and spatial arrangement of the gold core vary with cluster size. The gold core of nanoclusters larger than 144 gold atoms tends to adapt a face-center cubic (fcc) structure, while for smaller nanoclusters icosahedral or dodecahedral core structures are reported.[10] For example, Au_{146}(*p*-MBA)$_{57}$ is a fcc-based cluster and the Au_{102}(*p*-MBA)$_{44}$-cluster adapts a Marks decahedron based core.

The structure and composition of the metallic core have a significant impact on the electronic structure of gold MPCs. To illustrate, their energy states of atoms and molecules are discrete, whereas bulk metals have continuum energy states with overlapping valence and conduction bands (Figure 2).[7] In between the two extremes, classes of materials exist with size-dependent properties. Gold nanoclusters are divided into different size regimes, depending on the number

of constituent atoms. Larger, bulk-like species feature metallic character, whereas smaller molecular-like clusters with a large band-gap (~2.1 eV) are often classified as insulators.[54] This means that even minor changes in cluster size lead to significant changes in their electronic properties.
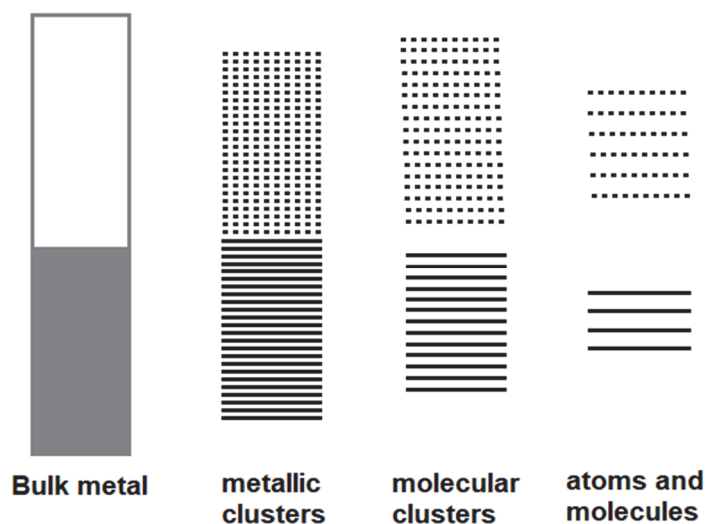

FIGURE 2 The effect of nanocluster size on the electronic structure. As the nanocluster's number of constituent atoms decreases, its energy level structure becomes discretized. As a result, the nanocluster evolves from being metallic to insulator-like.

In the case of thiolate-protected nanoclusters, ligands also induce minor effects on the electronic levels, which has to be taken into account.[24] The localized states of the ligand molecules contribute to the overall gold nanocluster system, withdrawing or localizing the free electrons. The electronic spectra of the same structures using different ligand molecules are very similar. Due to the well-defined structure of gold nanoclusters, electronic energy levels and ligand contribution of structurally known thiolate-protected clusters can be studied in detail by utilizing DFT calculations.[8]

The optical properties of gold MPCs are dominated by the structure (i.e. composition and geometry) that gives rise to the electronic state structure and density of the states. Studies have concluded that for thiolate-protected gold clusters the transitions between molecular and bulk properties converge between 130 and 144 gold atoms.[55-57] Nanoclusters containing more than 144 gold atoms are capable of sustaining collective conduction electron oscillations known as localized surface plasmon resonances (LSPR).[10] The oscillation of the conduction electrons leads to a strong extinction of light at the plasmon resonance. The extinction cross-section is a sum of the absorption and scattering cross-sections. The plasmon resonance for gold nanoparticles is size-dependent, and is typically centered at ~530 nm.[8] This property has attracted a lot of interest in various

applications based on field-enhancement effects such as chemically selective sensors.

Small nanoclusters with a large energy gap usually feature a strong optical absorption.[45,58] The electrons can be optically excited from occupied to unoccupied states, resulting in characteristic spectra of the clusters.

2.1.2 Structure and properties of Au$_{102}$(*p*-MBA)$_{44}$ nanocluster

The single-crystal structure of Au$_{102}$(*p*-MBA)$_{44}$-cluster has revealed that part of the gold atoms are located in the ligand layer. Some of the atoms protect the inner core by forming a gold-sulfur interface, known as the "staple" unit.[19,20,23] DFT calculations of several different thiolate-protected gold NCs have shown that the unique gold-sulfur staples protection and geometric arrangement of Au atoms is a general structural feature among gold MPCs.[20]

A closer experimental structure determination of the Au$_{102}$(*p*-MBA)$_{44}$-cluster has revealed that the staple units have different lengths (Figure 3). The gold atoms in both, short Au(RS)$_2$ and long Au$_2$(RS)$_3$ staple-units, are anchored by thiolates at both ends and covalently bonded to the outer ligand layer. The short-staple, with one gold and two sulfur atoms, resembles a rectangular shape, presented in Figure 3(2). The longer units, however, can contain two or more gold and three sulfur atoms forming a V-shape, commonly observed with smaller clusters, presented in Figure 3(3).[7]

The gold core of Au$_{102}$(*p*-MBA)$_{44}$-cluster is symmetric and consists of 79 gold atoms packed in a Marks decahedron, decorated with 19 short Au(*p*-MBA)$_2$ and 2 long Au$_2$(*p*-MBA)$_3$ staple units, as presented in Figure 3.[19] The diameter of the gold core is approximately 1.4 nm and the diameter of the whole cluster with ligand layer is 2.6 nm. The HOMO-LUMO gap of the cluster was determined both experimentally and computationally to be ~0.5 eV.[45] The nature of the Au$_{102}$-cluster was investigated in many other studies, in all of them showing the molecular behavior of the cluster.[57,59]
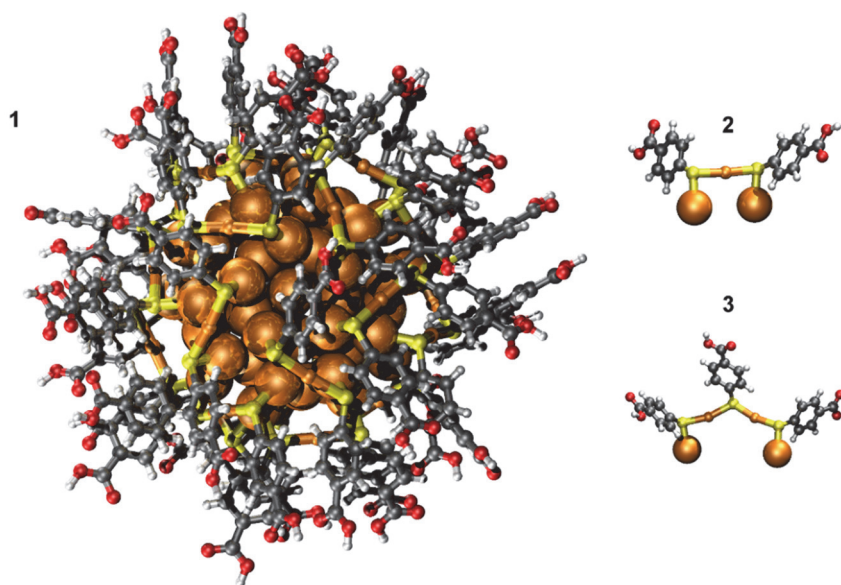
FIGURE 3 (**1**) Structure of $Au_{102}(p\text{-}MBA)_{44}$ nanocluster. Au atoms are in gold, C in grey, O in red, S in yellow, and H in white (**2**) short staple unit (**3**) long staple unit. Courtesy of Sami Malola. The structure this cluster is significant due to its precise composition, unique arrangement of atoms and stability described by filling of electron shell. For $Au_{102}(p\text{-}MBA)_{44}$-cluster the superatom model gives 58 free electrons corresponding with the closing of the superatom 1G shell.

The crystal structure of $Au_{102}(p\text{-}MBA)_{44}$ revealed that the cluster is in the fully protonated form. Nevertheless, the carboxylic group of the *p*-MBA-molecule is easily deprotonated.[52] As a result, the nature of the interface depends on the protonation state of the ligand layer molecules.[60] The experimental studies on protonation behavior and charge distribution of *p*-MBA-protected cluster Au_{102} reveal the cluster is water-soluble when more than half of the 44 ligands are deprotonated and soluble in methanol when completely protonated. [60]

Many studies have shown that the $Au_{102}(p\text{-}MBA)_{44}$-cluster undergoes ligand-exchange and site-specific conjugation with molecules containing reactive thiol[61] or hydroxyl[38,39] groups. For instance, $Au_{102}(p\text{-}MBA)_{44}$-cluster was reactive towards exposed cysteine residue in proteins or on virus surfaces and thiol-modified DNA-strands.[28,38]

2.2 Methodologies towards atomically precise gold nanoclusters

Almost all the properties of thiolate protected gold nanoclusters are governed by their composition, hence gaining synthetic control over the size and composition of the product are essential in the nanocluster field. The first efficient synthesis to produce monodisperse thiol-protected clusters was introduced in 1994 by Brust and Schiffrin.[21] Nowadays, the synthesis has been modified to produce

different sizes of clusters with a variety of thiolate ligands that are both soluble in organic or water-based solvents.[10,15,28,52,62] Thiols with alkyl chains or aryl thiols containing carboxylic groups are often used.

One of the challenges faced in nanocluster synthesis is the dispersity of the product. Among existing synthetic procedures, many produce polydisperse samples in terms of cluster size. Producing homogenous products by optimizing experimental conditions is highly desirable; however it often requires understanding reaction mechanisms.[14,63] Control over nanoparticle size and uniformity is achieved through post-synthetic treatments or by applying analytical separation techniques. Post-synthetic treatments such as fractional precipitation or core-etching reactions have been used to isolate final product or narrow down the size distribution, respectively (see Figure 4).[29,62,52,64,65] The method of choice depends on the chemical nature of particles.
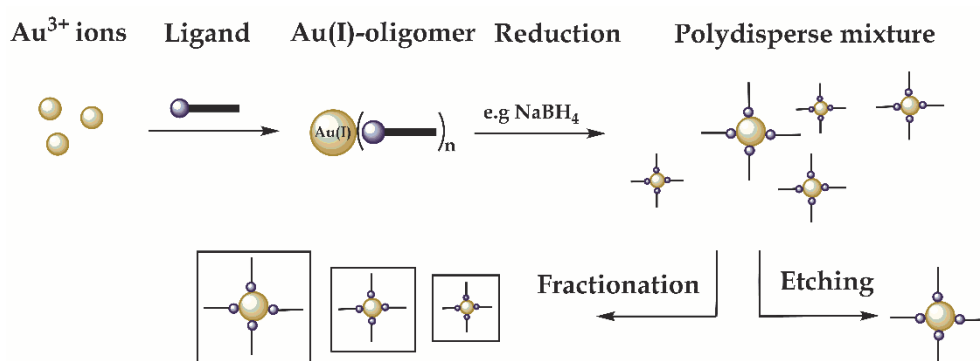

FIGURE 4   Schematic illustration of strategies for the size-controlled synthesis of gold MPCs. The synthesis starts by reduction of gold salt (Au(III)) in the presence of thiol to gold polymer (Au(I)) and final reduction to the metallic polydisperse ligand-protected gold cluster by using NaBH$_4$. The final product is obtained through post-synthetic treatments such as fractional precipitation or core-etching reactions. The elements in the image are not proportionally scaled.

Many of the existing strategies towards obtaining atomically precise gold MPCs are well developed for organo-soluble nanoclusters, whereas synthesis and separation methods for water-soluble ones are deficient. Particularly, the synthetic routes of plasmonic, water-soluble nanoclusters are underdeveloped. In this thesis, the synthesis and separation methods of large, water-soluble thiolate-protected clusters are studied.

2.2.1   Synthesis of thiolate gold nanoclusters

The typical Brust-Schiffin synthesis is based on a fast reduction of the gold polymer complex and slow core-etching, leading to the final nanocluster product. The synthesis starts by reduction of precursor metal ions Au(III) to Au(I) forming a polymer in presence of protecting thiolate ligands, illustrated in Figure 4. The next step of the synthesis involves fast reduction of the polymer to metallic Au(0)

and formation of the clusters in the presence of a strong reducing agent such as sodium borohydride (NaBH$_4$).[21] The last step involves the slow seed growth of the final product. Modified versions of the original synthesis usually include changes in thiol-to-gold molar ratio, solvent system, pH or time.[30,63,66] Studies have shown longer reaction times and smaller amounts of reducing agent provide controllable reduction kinetics and growth of particles.[63]

The synthesis of water-soluble gold MPCs is especially difficult to control. Often, obtaining a highly pure sample is challenging due to the similar solubility of products and impurities. Only a few water-soluble, thiol-protected clusters were synthesized by direct protocols, yielding one discrete size of particles.[28,53,67–70] Among them, Au$_{68}$(*m*-MBA)$_{32}$ and Au$_{144}$(*m*-MBA)$_n$ – clusters were obtained by changing the thiol-to-gold molar ratio,[53] while Au$_{102}$(*p*-MBA)$_{44}$ and Au$_{144}$(*p*-MBA)$_{60}$–clusters were synthesized by pH-controlled syntheses.[28,70]

The solubility of the cluster is dictated by the solubility of the ligands. If the ligands are soluble in water, they form water-soluble clusters. In contrast, the ligand layer for lipophilic clusters is composed of organo-soluble ligands.[71] Considering the most common organo-soluble thiolate ligands, phenylethanethiol (PET) has been widely used, while for water-soluble clusters mercaptobenzoic acids (MBA) or glutathione (GSH) ligands have been employed as shown in Figure 5(a) — (d).[62,72,73]

Essentially, the choice of the surface ligand affects nanocluster chemical properties but also the smallest change in the ligand structure has an impact on the nucleation process, directly influencing the particle size and its properties. The isomeric structure of the MBA ligand was shown to have a distinct effect on nanocluster reactivity.[46] Larger or bulky thiolate ligands promote the formation of small particles. PET-protected clusters or straight-chained alkanethiolates-clusters are found to form a variety of cluster sizes.[30,57,74,54] Water-soluble *p*-MBA-protected Au nanoclusters have shown a higher selectivity, and only specific clusters are formed, such as Au$_{102}$, or Au$_{146}$-nanoclusters.[28,32]
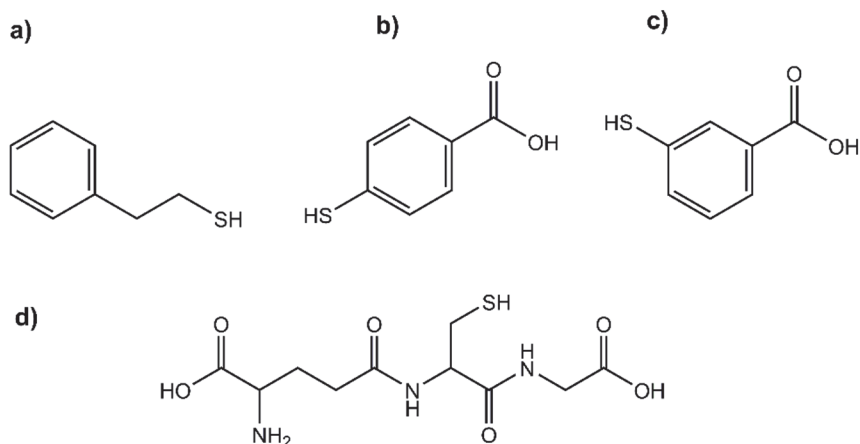

FIGURE 5   Structure of the commonly used thiolate ligands: (**a**) phenylethane thiol is used for organo-soluble products while (**b**) *para*-mercaptobenzoic acid, (**c**) *meta*-mercaptobenzoic acid and (**d**) glutathione are used for water-soluble products.

2.2.2 Purification

Given the synthetic challenges in obtaining single-sized clusters, often purification of the clusters from by-products is required in a form of additional post-synthetic treatment.

Etching or size focusing is one of the approaches for the cluster size control which utilizes external heating of excess thiol molecules.[29] The idea of this approach lies in the stability difference of different sizes of nanoclusters. Generally, the mixture of cluster sizes is heated leading to thermal etching. During the process, gold atoms are slowly being removed from the gold core until the metastable cluster converts into a more stable one, forming at the end a monodisperse product of a stable cluster size.

A promising approach for the selective synthesis of highly stable cluster sizes is etching, where a broad size distribution of clusters can be transformed into one stable cluster size.[75] The technique can be used to isolate many organo-soluble thiol-protected clusters, among them $Au_{25}(SR)_{18}$, $Au_{38}(SR)_{24}$, $Au_{144}(SR)_{60}$ and $Au_{333}(SR)_{79}$.[31,33,34,76,66]

Another method is to fractionate the desired cluster size from the cluster mixture. Fractional precipitation, commonly applied for water-soluble clusters, is based on different interactions of MPCs with solvent molecules, leading to different solubility. To isolate the desired product, the solvent composition must be tuned until separation is achieved. For instance, hydrophilic *p*-MBA-clusters are separated based on their solubility difference in methanol:water mixture.[28] Although fractional precipitation is based on interactions of the surface ligand with its environment, organo-soluble clusters protected by PET-molecules have been effectively fractionated by exploiting the differences in their core size.[62]

Gel electrophoresis is a type of fractionation where the desired size of the cluster is fractionated from a crude product mixture by applying an electric field across an acrylamide gel.[72,77,78] The negatively charged clusters migrate at different rates enabling a separation based on their size, shape or electric charge. Generally, smaller clusters have higher mobility and hence travel faster than the larger ones. This technique has been commonly used to separate small, water-soluble nanoclusters, e.g., those protected by GSH or *p*-MBA ligands.[71,73] Especially for clusters protected by ligands containing carboxylic functional groups the separation is very efficient. In the water-soluble nanocluster field, PAGE is applied to estimate the size or purity of the nanoclusters and for the preliminary analysis and separation of the reaction product.[72,73,79] For instance, the technique was applied to separate nanoclusters conjugated with proteins or oligonucleotides.[53] In this thesis, fractionation methods are applied and described in the experimental section.

Monolayer-protected gold nanoclusters are efficiently isolated by using several analytical tools. Chromatography is employed both for organo- and water-soluble clusters to separate a wide range of sizes.[80] The capability of high-performance liquid chromatography (HPLC) enables separating clusters with the same core size but dissimilar ligand types.[81,82] Size exclusion

chromatography (SEC) separates clusters based on their hydrodynamic volume (diameter), and can be used for larger-scale separation. SEC is successfully applied to separate both hydrophilic and hydrophobic thiolate-protected clusters.[83,74]

2.3   Functionalization

The properties of gold nanoclusters (NCs) are dictated by the nanocluster size, structure, and composition.[40,84,85] This section describes common modification methods of gold thiolate-protected clusters.

2.3.1   Metal core modification

The properties of gold MPCs can change radically when the composition of the parental cluster changes, even by a single atom. Inclusion of the foreign atom to the gold core of thiolate-NCs, commonly called doping, affects the electronic and photophysical properties of the final product.[84,86] The foreign metal atoms, for example Ag, Cu, Pd and Pt, dope the gold core of the nanocluster preserving its original number of metal atoms and ligands.[86]

The efficiency of doping depends on the properties of the dopant atom and the size and structure of the nanocluster. The foreign atom can be located at the center of the gold core or on the nanocluster surface. The level of doping was shown to depend on the size of the parental gold cluster.[87,88] As the size of the cluster increases, it can be mono-, bi- or multi-doped.

$Au_{38}(SR)_{24}$–clusters have been doped with several different metal atoms, inducing interesting effects.[84] Among them are charge stripping effects, where the charge of the cluster changed upon platinum doping from 0 to -2.[84] Bürgi and co-workers observed increased surface flexibility of the $Au_{38}(SR)_{24}$–cluster upon doping with palladium or silver atoms.[89] Silver or copper doping of Au_{25} has shown to enhance fluorescent properties and influence electronic structure, hence affecting the catalytic properties and enhancing general stability of the cluster.[86] In addition, reactivity of a ligand-exchange reaction increased dramatically upon doping $Au_{25}(SR)_{18}$ with palladium.[90]

2.3.2   Surface modification

Many factors in gold monolayer-protected clusters are affected by the surface ligands, including nanocluster growth during the synthesis, cluster stability and its optical properties. The protective ligand layer also determines the interaction of the functional material with its environment. In biological applications, the functional groups on the surface layer play a key role in determining their interaction with target molecules.[85]

Ligand-exchange is an efficient way to modify the nanocluster ligand surface by introducing new functionalities.[40,61,91,92] In principle, the already

existing ligand is replaced by another, incoming organic ligand carrying a new functionality, as shown in Figure 6(a). The incoming ligands change the solubility of the system or induce stronger binding affinity towards the gold surface, resulting in better stability.
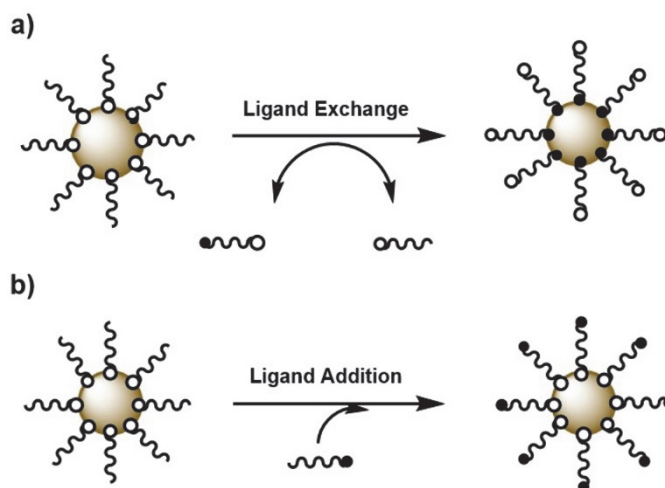

FIGURE 6   Surface modification strategies: (**a**) the surface is modified by exchanging the original ligand by new incoming one bearing new functionality, (**b**) addition of the ligand to the surface of parental cluster by conjugation chemistry approaches.

Typically, ligand-exchange processes are carried out at room temperature and can be roughly divided into three steps. Ackerson and co-workers studied the ligand-exchange mechanism based on the crystal structure of $Au_{102}(p\text{-MBA})_{44}$.[61] The kinetics of this process depends on the structure, reactivity and ratio between incoming and outgoing ligands, nanoparticle size and surface structure.[93] The first step is the rapid replacement of the most accessible ligands to the solvent by the incoming ones, resulting in a partially mixed shell. The second step is rather slow and involves the removal of the remaining ligands. The last step is the completion and optimization of the ligand shell.[63] The type of ligands used for the replacement (thiolate, phosphine, selenolate) often dictates the final mechanism and condition of the reaction.

One of the purposes of the ligand-exchange reaction is to transform less stable cluster sizes into more stable ones by exchanging the protective ligand layer.[41,94,95] Typically, phosphines are replaced by thiolate ligands or more recently thiolates to selenolates, yielding thiolate-protected or selenolate-protected gold nanoclusters of higher stability, respectively. Modification of the ligand layer can sometimes lead to a size change of parental cluster, where less stable clusters are transformed into more stable ones. If the modification synthesis is controllable, it is used as an alternative approach to form nanoclusters of increased stability, commonly called magic cluster sizes.[95-97]

Ligand-exchange between two thiolate ligands is an alternative to attain new properties.[98] For example, chirality or fluorescence properties were introduced to Au_{25}, Au_{38}, and Au_{40}-clusters by partial exchange of parental ligand

with chiral or dye molecules.[99–102] Using bifunctional ligands such as dithiol molecules is an effective strategy for nanocluster dimerization reactions. As a result, the functional groups on both sides undergo ligand-exchange resulting in chemically linked MPC superstructures.[103] This work utilizes ligand-exchange approaches to assemble gold nanoclusters into higher-order MPC structures.

The functional groups on the surface ligands are exploited in conjugation processes. Instead of exchanging the surface ligand, the conjugation techniques usually involves addition of the target molecule or surface to the nanocluster system creating a hybrid by covalent or non-covalent interactions, as shown in Figure 6(b).[38,39,69,53,85] The covalent conjugation yields more stable, site-specific bonding to the target component. It is achieved by exploiting functional groups such as -NH$_2$, -COOH, or -OH.[38,104] For instance, monolayer-protected gold clusters have been conjugated with small organic dye molecules to study fluorescence coupling.[13,105] Conjugation of biomolecules with nanoclusters creates a hybrid material that binds specifically to biological systems. This is highly specific binding, based on molecular recognition. Maleimide-functionalized Au$_{102}$(p-MBA)$_{44}$ nanoclusters were selectively bound to enterovirus cysteine to image virus capsid structures.[38,104]

The conjugation via weak electrostatic adsorption or hydrophobic interactions, where the attachment depends on the surface charge of conjugated components, has also been exploited.[39] This is a fast strategy to achieve desired functionality; however, the binding is non-specific, sometimes resulting in deficient control over chemistry.

2.3.3   Superstructure formation

Ligand-exchange reactions have been used to modify clusters by chemically binding them together, forming linked gold nanocluster assembles with new properties. In this case, gold nanoclusters serve as atomically precise building blocks and bifunctional ligands as connecting bridges. The pristine thiol-stabilized ligand layer is partially replaced by incoming bifunctional dithiol molecules, efficiently bridging clusters together.

Electromagnetic properties of nanoclusters are extremely sensitive to chemical environment. The localized surface plasmon resonance (LSPR) from one plasmonic nanoparticle hybridizes with the LSPR of a neighbouring particle.[106] This leads to changes in the excitation cross-section and electric field enhancement, which has found many sensor-based applications.[107,108] In addition, nanocluster assembly via molecular linkers enables control of interparticle distances, which is a promising and interesting alternative in molecular electronics.[109]

The assembly of gold MPCs by covalently binding clusters together has the advantage of having strong, specific, easy to control binding resulting in stable structures.[110] The studies have shown that in order to form a stable assembly of nanoclusters linear and rigid linker molecules are preferred.[111,112] Otherwise, short-chain of alkyl-dithiols lead to intra-cluster exchange, where short dithiol

molecules tend to connect with another molecule by a disulfide bond.[113] Formation of disulfide bonds between two connecting nanoclusters is known to break the electronic interaction between them.[103] Instead of linking, longer chains tend to form inter-staple bindings, forming "ring-like" structures on the nanocluster surface.

To study electron or energy transfer phenomena by connecting clusters together, a fully conjugated system needs to be assembled. In this regard, the communication between linked clusters is likely to happen through aromatic, conjugated molecules forming a conductive system. Aromatic dithiol molecules such as benzene-1,4-dithiol or p-terphenyl-4,4″-dithiol have been used to form a molecular bridge connecting gold MPCs, while maintaining a defined interparticle distance during assembly.[103] Another example of superstructure formation is the self-assembly of p-MBA-protected Au_{102} nanocluster into hexagonally packed 2D sheets and formation of spherical capsids of a colloidal superstructure.[114] Interestingly, such a structural organization was achieved by controlling the protonation state of the cluster upon a change of the solvent from methanol to water.

2.4   Characterization

Atomic structure of MPCs can be determined by X-ray crystallography and transmission electron microscopy (TEM) techniques in combination with quantum chemistry DFT.[23,32,47,48,115] Although water-soluble clusters have been crystallized, the structure determination of hydrophilic species is challenging. So far, the total structure of 10 thiolate gold nanoclusters have been determined,[97,116] among them water-soluble $Au_{102}(p\text{-MBA})_{44}$ and $Au_{146}(p\text{-MBA})_{57}$-nanoclusters.[23,32] Theoretical models and calculations support the experimentally determined structures, providing atomistic scale understanding on nanocluster electronic structures, stability and dynamics of the systems.[24,25,27,112]

Numerous other analytical tools have contributed significantly to a better understanding of these systems.[6] In the following chapter, some of the methods are described regarding their usability in the field of thiolate-protected gold nanoclusters.

2.4.1   Selected methods in nanocluster studies

Single-crystal X-ray is a straightforward and decisive analytical tool to solve the complex structure of gold MPCs. This achievement of solving the atomic structure of $Au_{102}(p\text{-MBA})_{44}$ has revolutionized the fundamental understanding of the thiol-protected gold nanocluster field.[23,27,20] The non-trivial problem with X-ray crystallography is growing a high-quality crystal.[4] Generally, growing the X-ray quality crystal requires a homogeneous sample and the cluster's ability to pack into a well-ordered lattice. This has been especially challenging for water-

soluble clusters, containing >100 gold atoms, due to this large surface charge. The crystallization of water-soluble clusters requires carefully chosen conditions such as pH, salt concentration, and other additives such as alcohols and glycols that may influence the crystal formation.

The structure determination of monolayer-protected gold clusters has been accomplished by combining aberration-corrected TEM and minimal electron dose imaging techniques.[47,48] Spherical-aberration (C_s)-corrected TEMs enable reaching an imaging resolution at the sub-angstrom level, which is highly advantageous in the structural characterization of small nanoclusters. For example, the structures of Au_{68} and Au_{144} m-MBA-protected nanoclusters were reconstructed by collecting images of different cluster orientations, averaging them for improved resolution and calculating the initial model.[47,48] Experimentally assigning gold atoms based on TEM with the support of theoretical models and calculations solved the complete structure of thiol-protected gold nanocluster.[115] The combination of electron microscopy with spectroscopic techniques such as electron energy-loss spectroscopy (EELS) or energy-dispersive X-ray spectroscopy (EDX) enables advanced analytical imaging techniques. A combination of high spatial resolution to record images and sensitive spectral signals from the same region of interest gives a possibility for detailed analysis and identification of specific features. The acquired data provide an atomic spatial composition, possibility to identify elements in the specimen, chemical bonding and electronic structure information.[117]

Mass spectrometry is an excellent method to measure chemical composition ($Au_n(SR)_m$) of monolayer protected clusters. Soft ionization techniques such as electrospray ionization (ESI)[118] or matrix-assisted laser desorption/ionization (MALDI)[119] methods have been widely used providing reliable molecular weight information for the nanoclusters. An advantage of these methods is the capability of measuring intact clusters without causing fragmentation. This is especially important for water-soluble clusters, where protonation or deprotonation of functional groups causes ionization of nanoclusters into multiple-charged ions, making the measurements and analysis significantly more challenging.[15]

UV/vis/IR spectroscopies are valuable tools in the nanocluster field to study light cluster interactions. The interactions are sensitive to size, shape, capping ligand, environment and agglomeration state of the nanoclusters.[10,11,45,54,120] The amount of absorbed light gives information about the optical properties and structural details of nanoclusters.[10,11]

UV-vis spectra allow estimating the molecular or metallic behavior of the clusters. The spectra of ultra-small gold nanoclusters feature multiple distinct absorption features characteristic to the specific band structure; therefore this method has been applied to study the electronic properties of small MPCs.[45,120] For example, the molecular behavior was studied by UV-vis spectroscopy in the following clusters: $Au_{25}(SR)_{18}$, $Au_{28}(SPh\text{-}^tBut)_{20}$, $Au_{36}(SPh\text{-}^tBu)_{24}$, $Au_{38}(SR)_{24}$ and $Au_{64}(SC_6H_{11})_{32}$.[7,34] In the larger species, a broad absorption at 530 nm dominates the spectrum. This spectroscopic feature is attributed to localized surface

plasmon resonance properties.[11] The UV-vis spectra allow monitoring the various nanocluster reaction processes and following the optical features, such as formation of additional prominent shoulders or by changes in the resonance band. For example, the appearance of absorption bands at around 800 nm have been assigned to electronic coupling effects between linked cluster units.[103]

The studies in the infrared region, are concentrated on the structural details of the ligand molecules, such as gold-thiol binding interaction.[11,121,122] The IR spectrum can identify vibrational modes of many functional groups in the molecule and gain information about the ligand layer of the cluster. For example, the structure and dynamics of *m*-MBA protecting ligand layer was studied, demonstrating dynamic interaction at the ligand-metal interface.[46]

Nuclear magnetic resonance (NMR) spectroscopy is widely applied for characterizing both the formation and final structures of gold nanoclusters.[49] It provides details about structure and dynamics of the organic ligand surrounding the cluster. For instance, full assignment of ^{1}H and ^{13}C NMR shifts to all ligands of a water-soluble Au_{102}(*p*-MBA)$_{44}$ was accomplished by NMR methods.[123] The same group also determined hydrodynamic radius of Au_{25}(PET)$_{18}$, Au_{38}(PET)$_{24}$, and Au_{144}(PET)$_{60}$-nanoclusters by NMR diffusion-ordered spectroscopy, in good agreement with previous studies.[124] Chemical resolution of NMR techniques are capable of monitoring reaction mechanisms and reaction rates of gold nanoclusters. Ligand-exchange reactions have been studied by using different NMR techniques to gain kinetic and thermodynamic insights into the processes. Salassa *et al.* monitored ligand-exchange in real-time and evaluated the affinity of a thiol exchange reaction between Au_{25}(PET)$_{18}$ and butanethiol (ButSH) molecule.[93]

3 EXPERIMENTAL METHODS

This chapter describes the main purification and analytical methods used by the author. The techniques include fractional precipitation, gel electrophoresis, gel densitometer analysis, UV-vis spectroscopy, and transmission electron microscopy.

3.1 Fractional precipitation

In this work, the fractional precipitation technique was applied to obtain two stable sizes of monodisperse particles, namely $Au_{102}(p\text{-MBA})_{44}$ and $Au_{\sim442}(p\text{-MBA})_{\sim115}$–nanoclusters, respectively labeled as Au_{102} and Au_{450} nanoclusters. The technique separates the clusters based on differences in solubility. The protecting p-mercaptobenzoic acid (p-MBA) organic ligands contain a protonatable functional group. Deprotonation of the carboxylic group makes the cluster more water-soluble, whereas protonation favors nanoclusters in methanol-soluble form. Larger nanoclusters precipitate first from the nanocluster mixture when high concentration of methanol solution is added.[28,52] Efficient and successful separation requires optimization of the solvent composition.[28] Due to similar solubility between impurities and clusters, optimizing the purification parameters can be challenging.

3.2 Separation and purification

Polyacrylamide gel electrophoresis (PAGE) was applied to separate the nanocluster oligomers linked with different thiols. The separation was performed by using BioRad Mini-Protean Tetra System apparatus operated at 130 V. Separation efficiency depends on the density of the gel network. In this work, polyacrylamide gels (15 w/v %, 29:1 acrylamide/bisacrylamide) with 1.0

mm thickness were used in separation. Dithiol-linked oligomer solutions are loaded into the gel sample wells and travel through the gel in response to the electric field, separating into several distinct bands. An example of electrophoretic separation of linked clusters is shown in Figure 7.

For the spectroscopic study and TEM imaging, the oligomer fractions were separated from the gel to obtain higher purity of the oligomer fractions. The separation was done by mechanically cutting the fractions out from the gel and soaking separately in a small amount of water. Clusters dissolve from the gel to the water solution. The solution was filtered through a centrifugal filter tube with a pore size of 0.22 µm and concentrated for further analysis. For higher purity, each separated fraction was run through the acrylamide gel and separation was repeated.
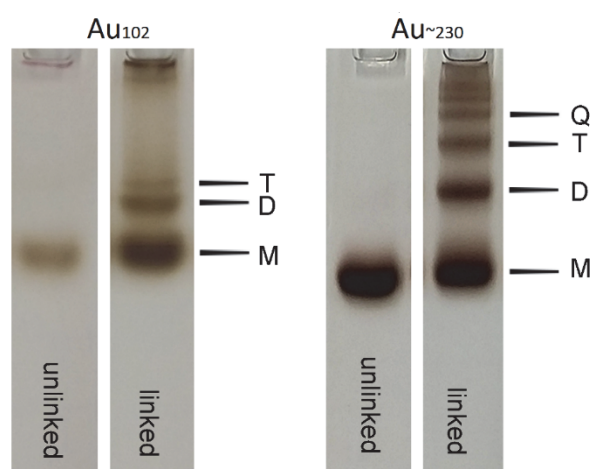

FIGURE 7   Electrophoretic separation of Au_{102} and $Au_{\sim 230}$ - clusters and their linked oligomers. Linked oligomers separate into several distinct bands based on the size of oligomer.[125]

3.3   Gel densitometry analysis

A novel method to analyze reaction yields of covalently linked gold nanoclusters was developed. The method was inspired by densitometry analysis of Western blot.[126] A standard desktop scanner was used to quantify electrophoretically separated oligomer fractions.

Calibration of the scanner was done against a set of neutral density filters. The absorbance of each filter was measured by UV-vis spectroscopy, followed by a desktop scan with Canon imageRUNNER. The grayscale values obtained from the scanned image are plotted against absorbance of each filter at 500 nm. A calibration curve from grayscale to absorbance values was obtained.

The gel image of separated fractions of covalently liked gold superstructures was converted into a grayscale image. The darkness maximum of each band was selected and the mean intensity of each pixel was calculated.

The greyscale values were converted to the absorbance value using the conversion curve obtained from calibration. The absorbance values were integrated over a band and directly converted to reaction yields, based on the known number of clusters per oligomer from TEM.

3.4   Absorption spectroscopy

UV-vis spectroscopy was used to study the optical properties of nanoclusters and the changes to the spectrum upon covalent linking and formation of gold superstructures.

Each of the gold nanoclusters was measured by UV-vis spectroscopy. The measurements were performed using deionized water with a Perkin Elmer Lambda 850 UV-vis-spectrometer with 2 nm resolution, using 1 mm quartz-cuvettes. The absorption of separated fractions of dithiol-linked oligomers was measured from a concentrated water solution or directly from wet PAGE gel. For the direct measurements from PAGE gel, each electrophoretically separated fraction of oligomers was sandwiched between two quartz slides and the light beam was accurately positioned on individual gel bands by maximizing the absorption using an micrometer-XYZ stage.

3.5   Basics of transmission electron microscopy

In this thesis, transmission electron microscopy (TEM) was used to provide information about particle size, shape and metal core structure.

A JEOL JEM-1400HC microscope with reduced exposure time and electron acceleration voltage of 80 kV or 120 kV was used for imaging gold nanoclusters. The samples were prepared by drop-casting 8 µL of deionized water solution of Au nanoclusters on a glow discharged 400 mesh holey carbon copper grid (Ted-Pella ultrathin c) or 3-5 Layer Graphene on 2000 copper grid. After 10 minutes of deposition, the excess solution was blotted from the side to remove excess liquid. The grid was submerged sequentially in methanol, water, and methanol, and dried.

The atomic composition of molecular bridge between linked structures was analyzed by combining STEM with electron energy-loss spectroscopy (EELS). The experiment was done using the JEM-ARM300F at 80 kV with Gatan TEM Analytical Holders using Gatan GIF Quantum detector. The EELS experimental data were recorded at the core-loss region showing characteristic features at given ionization energy for each element (S, C, N, and O). The sulfur characteristic ionization energies were used to record energy-filtered images, showing spatial distribution of sulfur signal in the sample. The challenge for such atomic-level analysis is due to low signal-to-noise ratio and the cluster's instability under constant electron scan. The outer organic ligand layer is

radiation sensitive, and usually composed of light elements, giving rise to weak image contrast.

A schematic illustration of the TEM imaging system is shown in Figure 8. The instrument can be divided into three separate parts, each responsible for specific functions. Starting from the top: illumination system, specimen, and the imaging system. The illuminating system consists of electron gun (typically thermionic or field emission sources) together with condenser lenses that focus the electrons onto the specimen. The specimen is located below the illumination system. The sample can be inserted or withdrawn using a sample holder. The lower part of the microscope consists of an imaging system. The sample is imaged with an objective lens, and several magnetic lenses produce the final magnified image or diffraction pattern depending on the imaging mode. Typically, the TEM are either conventional TEM (CTEM), where the sample is illuminated as a whole, or the sample is scanned point-by-point with a tightly focused e-beam. (STEM).
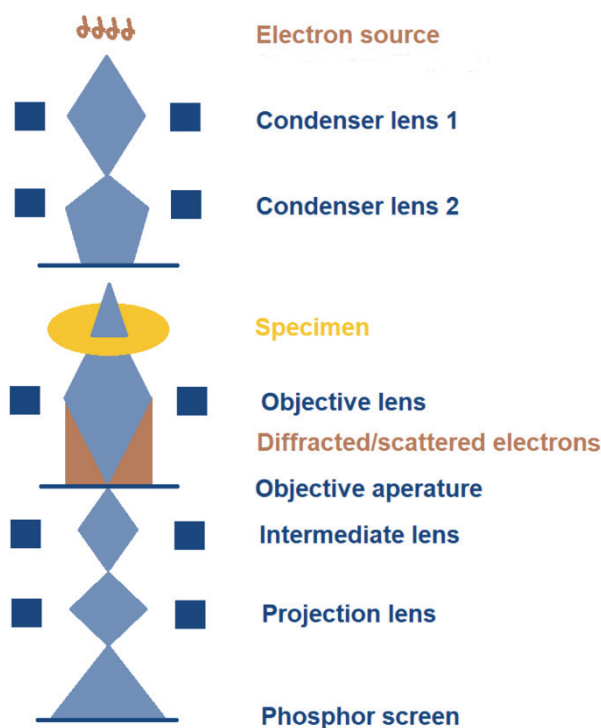

FIGURE 8   Basic components of a TEM.[4] The microscope is divided into three parts. Starting from the top, the illumination system, specimen stage where the sample is inserted or withdrawn, and the last part consists of an imaging system.

4 RESULTS AND DISCUSSION

In this chapter, the main results of the papers **I-III** along with unpublished results of electron energy-loss spectroscopy (EELS) and X-ray photoelectron spectroscopy (XPS) of atomically precise covalently linked clusters are presented.

Producing a homogenous sample is a prerequisite for understanding many fundamental phenomena in the nanocluster systems. In light of that, this thesis is a synthetic work, focusing on development of covalently linked individual constructs from water-soluble gold nanoclusters with accurately known atomic numbers. Formation of a bridge between two gold nanoclusters creates a new class of material, enabling the studies of electron coupling and electron transfer phenomena.

The foundation of my studies was to develop a synthesis to covalently link water-soluble gold nanoclusters. Connecting gold nanoclusters together creates a new family of atomically precise structures with new properties. The synthetic control over design and properties of superstructures requires fundamental understanding of newly developed systems, especially the role of the covalent bond. Answering a question whether linked structures are only mechanically linked together, or whether the bond formation also leads to changes in the electronic properties, was of primary interest in the studies.

The molecular mechanism leading to the formation of MPC superstructures was studied in detail in this thesis. Building a family of superstructure assemblies by varying nanocluster sizes or changing linked molecules forming the molecular bridges has enabled systematic studies of reaction conditions, deepening the understanding of the forces driving the reaction process. STEM-EELS and XPS measurements give spatial insight into the linked structures, confirming the molecular bridges between clusters (unpublished results). Studying the formation of the covalent bond, and finding how many linker molecules are needed to bridge the clusters, contribute to better understanding of plasmonic coupling through molecules.

This work yields covalently linked gold nanocluster constructs with accurately known atomic structures and present a study of their optical and structural properties. Furthermore, the synthetic work to form plasmonic,

water-soluble *p*-MBA-protected nanoclusters is presented. Structural studies and prediction of molecular composition of synthesized clusters were performed by combining experimental measurements with computational studies.

The MD simulations and DFT computations included in this work are important results complementing experimental information. They were achieved through in-house collaboration. STEM-EELS measurements were carried out at Irvine Materials Research Institute (Irvine, CA). XPS measurements were obtained via collaboration with the University of Vienna.

4.1   Water-soluble *p*-MBA-protected gold nanoclusters

Three distinct sizes of *p*MBA-protected gold nanoclusters were synthesized by a modified one-phase Brust-Schiffrin synthesis. $Au_{102}(p\text{-MBA})_{44}$-clusters were synthesized by previously published protocol.[28,52] The other two sizes of Au clusters were obtained under pH-controlled conditions, as shown in Scheme 1. The synthesis of the *cluster 1* [later assigned as $Au_{210-230}(p\text{-MBA})_{70-80}$][127] is a direct procedure, yielding only one discrete size of particles.[125] In this thesis, the synthesis of *cluster 2* was developed.[127] *Cluster 2* [later assigned as: $Au_{426-442}(p\text{MBA})_{112-115}$][127] was synthesized and purified by fractional precipitation.

All the synthesized clusters were characterized by several methods. The purified product of $Au_{102}(p\text{-MBA})_{44}$ synthesis was successfully identified at the University of Tokyo using a homemade time-of-flight (TOF) mass spectrometer.[125] The monodispersity was confirmed by PAGE, NMR, UV-vis, and TEM.[52,125] The size range of synthesized *cluster 1* and *cluster 2* was estimated from thermogravimetric analysis (TGA), HR-TEM and gel electrophoresis. The evolution of optical properties was followed by UV-vis spectroscopy.[127] Powder X-ray diffraction measurements were compared to theoretical reference powder diffraction curves of reference systems: $Au_{146}(p\text{-MBA})_{57}$, $Au_{246}(SC_6H_4CH_3)_{80}$, and $Au_{279}(TBBT)_{84}$-clusters. Based on experimental results the computational predictions were developed, representing structural features for water-soluble gold clusters.

4.1.1 Syntheses
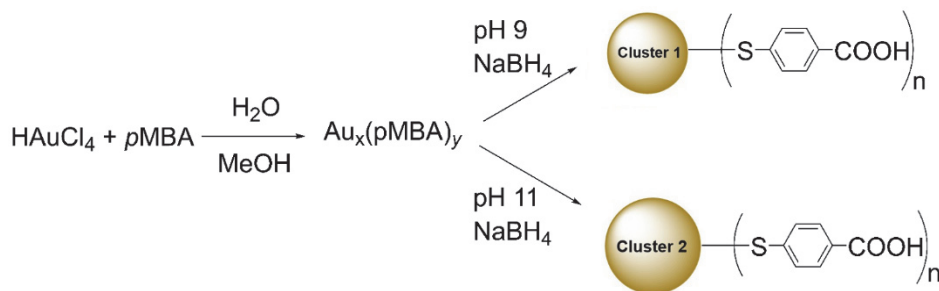
SCHEME 1 General schematic route for water-soluble p-MBA-protected gold nanoclusters. Both clusters were synthesized by pH-controlled synthesis. *Cluster 1* is synthesized in pH 9 and *Cluster* 2 in pH 11.

Modified Brust-Schiffrin synthesis of water-soluble $Au_{102}(p\text{-MBA})_{44}$ cluster was performed as follows: gold salt precursor ($HAuCl_4 \cdot 3\ H_2O$) and p-mercaptobenzoic acid (p-MBA) ligand were dissolved in water and methanol, respectively. Next, the gold salt and thiol were mixed in molar ratio 1:3, water was added, and the pH was adjusted to 13. The mixture was stirred at room temperature for 20 hours. The as-formed white polymer was then reduced by adding solid $NaBH_4$, followed by 5 hours of stirring. The product was precipitated by addition of ammonium acetate and methanol and collected in a microfuge at 35000 rpm for 15 minutes. The pellet was allowed to dry and purified by fractional precipitation.

The purification of the product was accomplished by first removal of the contaminant by precipitating the sample at 60% methanol. At this point, all the big particles and impurities stay in the pellet, while the supernatant contains the main product. The last step of purification involves adjusting the supernatant to 0.12 M ammonium acetate, 78% of methanol and centrifuging. The pellet from precipitation contains Au_{102} nanoclusters of approximately 1.4 nm in diameter in electron microscopy images.

The two other sizes of gold monolayer-protected clusters (MPCs) were synthesized by a similar approach. **The synthesis of cluster 1** starts by dissolving gold salt solution in water and p-MBA ligand in methanol immediately before use and mixed in molar ratio 1:6 (Table 1). Following the addition of water, pH was adjusted to 11 with NaOH. The mixture was equilibrated for 20 hours at room temperature. A freshly prepared solution of reducing agent $NaBH_4$ was added and the reaction proceeded for 4.5 hours at room temperature. The reaction was quenched by precipitating the product with addition of NaCl and methanol. The reaction yields monodisperse gold nanoclusters of approximately 1.8 nm in diameter from electron microscopy images.

The synthesis of cluster 2 was developed based on the synthetic protocols of $Au_{102}(p\text{-MBA})_{44}$ and *cluster 1* (see Table 1). The synthesis was carried out in a similar manner, only at a lower pH. The pH was adjusted to 9 by addition NaOH. The reaction product contains polydisperse clusters requiring fractional

precipitation. The sample is first precipitated with 25% methanol. The supernatant is adjusted to 80% methanol and centrifuged. After centrifugation, the pellet contains *cluster 2*. The reaction yields gold NCs of approximately 2.2 nm in diameter from electron microscopy images.

Table 1.   Synthesis protocols of *p*-MBA-protected gold nanoclusters. The values in columns 2, 3, 7 correspond to the molar ratios.[127]

	polymerization				reduction		purification
Nanoclusters	*p*MBA	HAuCl₄	MeOH %	pH	MeOH %	NaBH₄	MeOH %
Au102	3	1	47	13	47	1.1	60
Cluster 1	6	1	28	11	26	1.8	pure product without fractional precipitation
Cluster 2	6	1	25	9	25	1.8	25

4.1.2   Analysis of synthesized clusters

Dispersity and size range of the synthesized products were initially acquired from PAGE, as shown in Figure 8(a). The previous studies have shown that thiolate-protected gold nanoclusters appear as a single, distinct band in a PAGE.[72,120] Both products formed an individual band, indicating a monodisperse cluster size, shown in Figure 9(a). The product synthesized at pH 11 (*cluster 1*) had lower mobility compared to reference $Au_{102}(p\text{-MBA})_{44}$, indicating a larger size of the cluster. Nanocluster synthesized at pH 9 (*cluster 2*) formed a single band slightly above the previous products. Retention factors were determined to be 0.77, 0.64 for *cluster 1* and *cluster 2*, respectively. The dispersity was also verified by HR-TEM, yielding a core diameter of the smaller cluster of 1.7±0.1 nm and of the larger one of 2.2±0.1 nm.

The UV-vis spectra of the synthesized clusters were measured in D_2O and are shown in Figure 9(b). The spectra show size-dependent evolution of surface plasmon resonance of three distinct sizes of monodisperse *p*-MBA-protected gold nanoclusters. In contrast to the broad absorption of $Au_{102}(p\text{-MBA})_{44}$-cluster in the entire UV-vis region, *cluster 1* and *cluster 2* exhibit a distinct absorption band at 530 nm, which is consistent with the surface plasmon resonance (SPR). Based on the literature, the SPR feature begins to appear when the cluster consists of at least 200 gold atoms and becomes more prominent with the size increase. Therefore, these three clusters are good candidates to study threshold size for the emergence of surface plasmon properties. The prediction of the nanocluster's symmetry, molecular composition and structure is discussed in the next subsection.
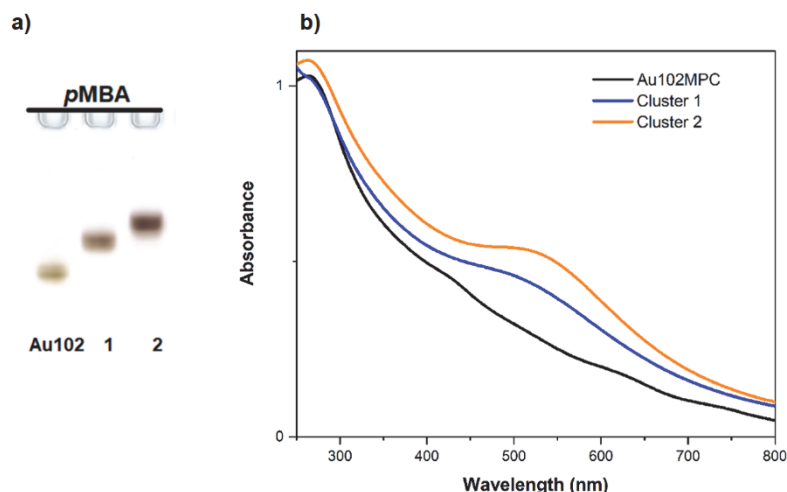
FIGURE 9 (**a**) PAGE bands of Au_{102}, *cluster 1* and *cluster 2*; Au_{102}–cluster has higher mobility comparing to *cluster 1* (**1**) and *cluster 2* (**2**). *Cluster 2* moves the slowest in the gel indicating the largest size of the cluster (**b**) UV-vis spectra of Au_{102}, *cluster 1* and *cluster 2* solvated in D_2O.[127]

4.1.3   Atomic structure and composition

The atomic structure and molecular composition of synthesized clusters were estimated based on experimentally measured powder XRD, HR-TEM, TGA to evaluate the properties of selected, structurally known water-soluble thiolate-gold clusters such as $Au_{102}(p\text{-MBA})_{44}$, $Au_{146}(p\text{-MBA})_{57}$. Due to the lack of experimentally resolved structures of large water-soluble clusters, $Au_{246}(SC_6H_4CH_3)_{80}$, and $Au_{279}(TBBT)_{84}$-nanoclusters were selected as the largest representatives of thiolate protected clusters.

The atomic structure of synthesized clusters was investigated by comparing experimental XRD patterns to the calculated XRD patterns of structurally known thiolate clusters (Figure 10). $Au_{146}(p\text{-MBA})_{57}$-cluster displays an fcc-based twinned core, and so far it is the largest structurally known soluble-in-water cluster. The calculated XRD pattern of Au_{146} cluster resembled the experimental data of the synthesized clusters. The strongest diffraction peaks at 38.8, 66.2, and 75.7° 2θ in both experimental patterns are located at the same diffraction angles as those of the $Au_{146}(p\text{-MBA})_{57}$ cluster. To compare, $Au_{246}(SC_6H_4CH_3)_{80}$ and $Au_{279}(TBBT)_{84}$-nanoclusters display respectively dodecahedral and fcc cores. The diffraction patterns show additional minor peaks at ~45 and ~50° 2θ which are not present in the experimental data sets of synthesized clusters. Besides, the most prominent peaks (38.8, 66.2, and 75.7 °2θ) are shifted to lower 2θ angles. Based on these observations, we speculate that the metal cores of new clusters most likely adopt a twinned fcc symmetry.
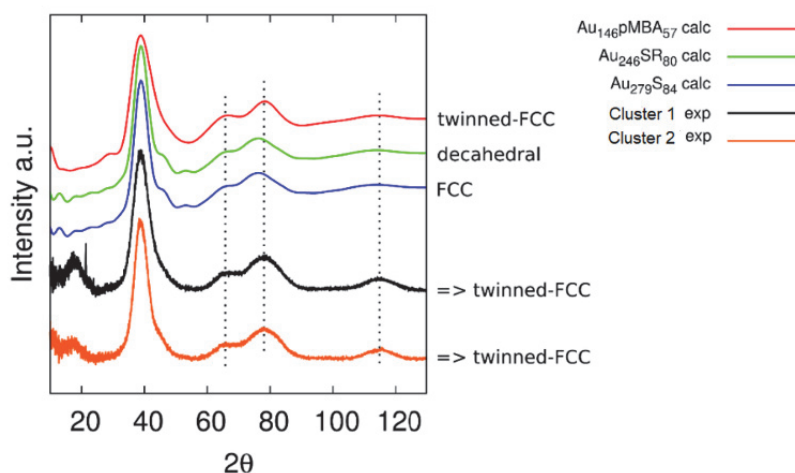
FIGURE 10 Diffraction patterns of the nanoclusters; comparison of experimental patterns of *cluster 1* and *cluster 2* with calculated patterns of Au_{146}, Au_{246} and Au_{279} clusters.[127]

Based on *cluster 1* and *cluster 2* experimental diameters and the prediction of twinned fcc octahedral arrangement, computationally aided models suggested metal core candidates, Au_{201-} core for the *cluster 1* and Au_{405}-core for *cluster 2* (Figure 11a). The diameter of calculated models agreed with the experimental diameter estimations, 1.7±0.1 nm and 2.2±0.1 nm respectively. The simulated HR-TEM images of Au_{201} metal core remarkably support the imaging experiment of *cluster 1* (Figure 11b). The experiments and simulation clearly showed the lattice fringes and characteristic stacking fault defects are only reproducible with fcc symmetry, shown in Figure 11(b) [(b),(d)].
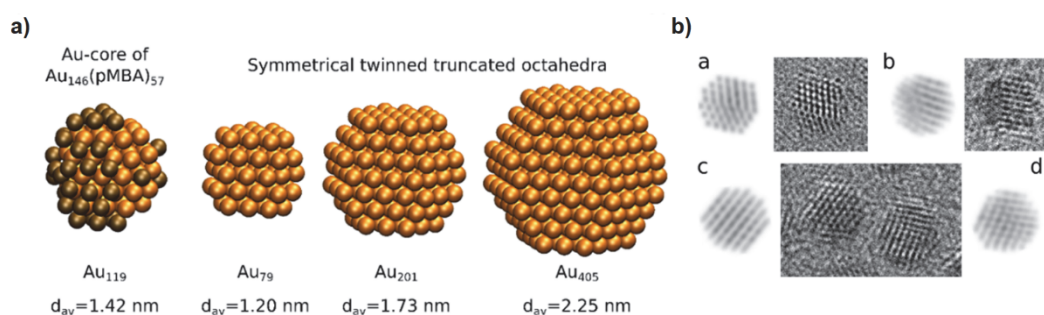

FIGURE 11 (**a**) Range for possible basis for a metal core structure in twinned octahedral arrangements; orange represents gold atoms and brown represents additional layer of gold atoms on top of symmetrical Au_{79}, representing together the gold core of $Au_{146}(p\text{-MBA})_{57}$ cluster; (**b**) Simulated HR-TEM images of Au_{201} metal core (white) in comparison to experimental images of *cluster 1*.[127] The experimental images show the lattice fringes and characteristic stacking fault defects.

The prediction of the molecular composition of the synthesized nanoclusters rely on the correlations to the selected structurally known clusters.

To estimate the number of gold atoms, the correlation between total number of gold atoms (metal-core and Au-S interface) as a function of diameter was made in the selected known clusters (Figure 12). To estimate the number of ligands, the correlation of the number of ligands to the spherical surface area in the known structures was made. If the synthesized *cluster 1* fits the trend and behavior of thiolate protected gold clusters, it consists of 210 gold atoms and 71 ligands in the protecting layer. The upper size limit of the gold atoms at 230 results in 2.1 nm diameter and 75 ligands.
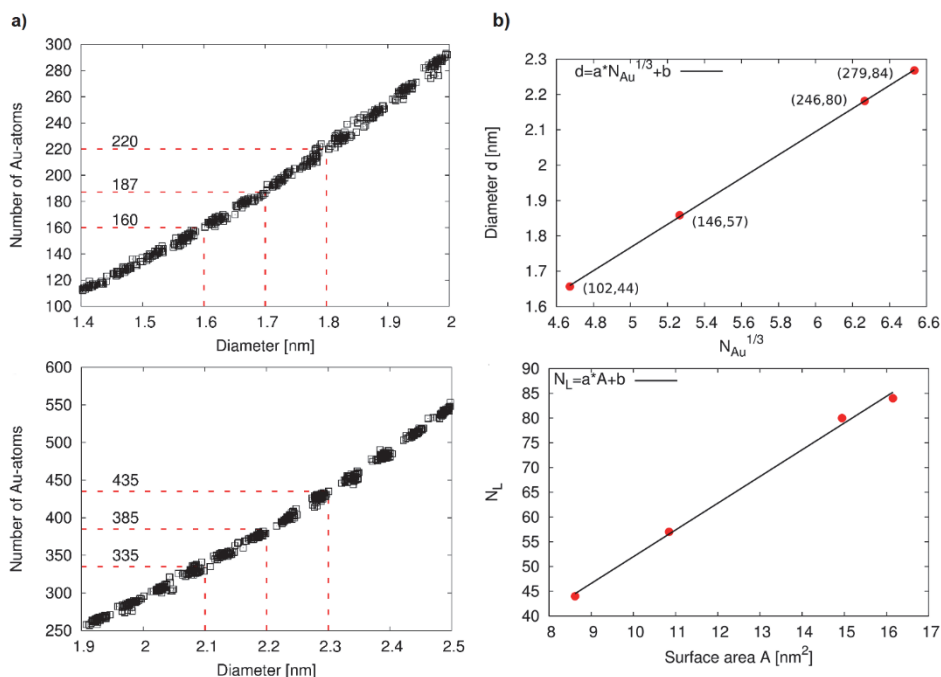

FIGURE 12 (**a**) Number of Au atoms of the spherical bare twinned fcc Au-clusters in the size range relevant to *cluster 1* and *cluster 2*. The plausible sizes 187 and 385 of the metal core for the measured diameters are labeled in the figure. (**b**) upper: linear fit correlates the number of Au atoms (metal core and Au-S interfaces) in the cluster to the diameter of the cluster; lower: correlation of spherical surface area to the number of ligands.[127]

The predictions for the larger synthesized *cluster 2* are not as accurate due to the lack of a reference structure of a large thiolate-protected cluster. The experimentally measured diameter of metal-core is 2.2 nm, which corresponds to 405 gold atoms based on the model. The addition of metal-ligand interface (0.4 nm) results in a 2.6 nm particle. Based on previously described gold atoms-to-diameter and spherical surface area-to-number of ligands correlations, the composition of the larger cluster is 429 gold atoms in total and 113 ligands.

The computationally aided predictions for both clusters are in good agreement with the experimentally determined number of ligands from thermogravimetric analyses (TGA). Based on experimental TG, *cluster 1* is composed of 73−80 ligands, whereas for *cluster 2* 111−116 surface ligands were determined.

As a summary, the best predictions of molecular composition for both clusters are $Au_{210-230}(p\text{-MBA})_{70-80}$ and $Au_{426-442}(p\text{-MBA})_{112-115}$ for *cluster 1* and *cluster 2* respectively. From now on, *cluster 1* and *cluster 2* are labeled as Au_{230} and Au_{450}-nanoclusters.

4.2 Formation of gold superstructures

This chapter describes the experimental effort to synthesize atomically precise structures by forming covalently bound molecular bridges between clusters. The formation of nanocluster-based superstructures with atomic precision opens new possibilities to learn the properties of this newly developed family of superclusters, and then to utilize the knowledge to control them by chemical and optical means by changing the size of nanocluster or linker molecules forming the nanocluster superstructures. The experimental results and analyses in combination with computational methods helped to gain insight into the nature of the bonding between the clusters.

4.2.1 Synthesis design

A straightforward approach to produce covalently bound multimers of gold MPCs was developed. Gold superstructures were synthesized by performing a ligand-exchange reaction using two different sizes of gold nanoclusters as building blocks, namely $Au_{102}(p\text{-MBA})_{44}$ and $Au_{210-230}(p\text{-MBA})_{70-80}$ (Au_{102} and Au_{230}). The multimers were bound together with several different dithiol molecules presented in Figure 13: biphenyl-4,4′-dithiol (BPDT) **1**, 5,5′-bis(mercaptomethyl)-2,2′-bipyridine (BMM-BPy) **2**, 4,4″-thiobisbenzenethiol (TBBT) **3**, benzene-1,4- dithiol (BDT) **4**, 1,4-benzenedimethanethiol (BDMT) **5** and dimercaptostilbene (DMS) **6**.

FIGURE 13 Molecular structure of the bifunctional thiols used to link gold NCs.[128] Biphenyl-4,4′-dithiol (BPDT) **1**, 5,5′-bis(mercaptomethyl)-2,2′-bipyridine BMM- BPy) **2**, 4,4″-thiobisbenzenethiol (TBBT) **3**, benzene-1,4- dithiol (BDT) **4**, 1,4-benzenedimethanethiol (BDMT) **5** and dimercaptostilbene (DMS) **6**.
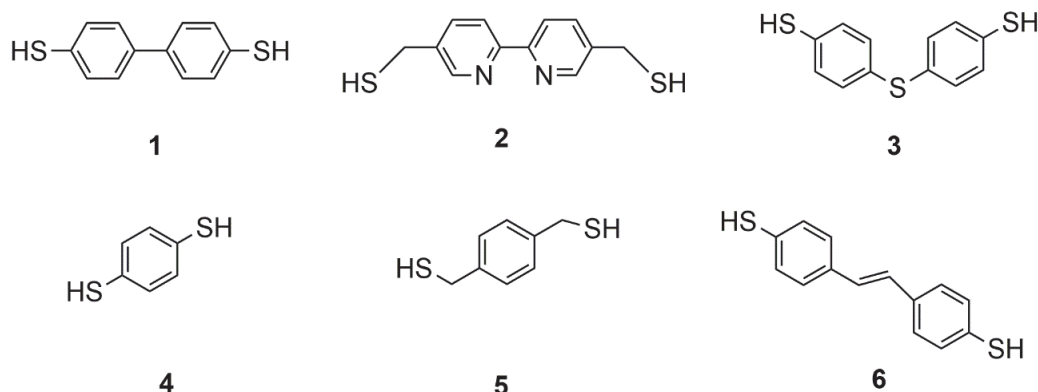
A ligand-exchange reaction leading to superstructures formation was carried out as follows: the stock solution of BPDT **1** in THF was added to the water-solution of nanocluster (2:1 ratio of incoming thiol/gold clusters), and the solution was stirred for 3.5 hours (Scheme 2). Next, the solution was quenched with isopropanol and ammonium acetate and centrifuged at 3500 rpm for 10 minutes. The supernatant was removed and the pellet was resuspended and washed in a 1:1 solution of H_2O/THF. The solution was precipitated again and washed to remove any remaining free thiol molecules.
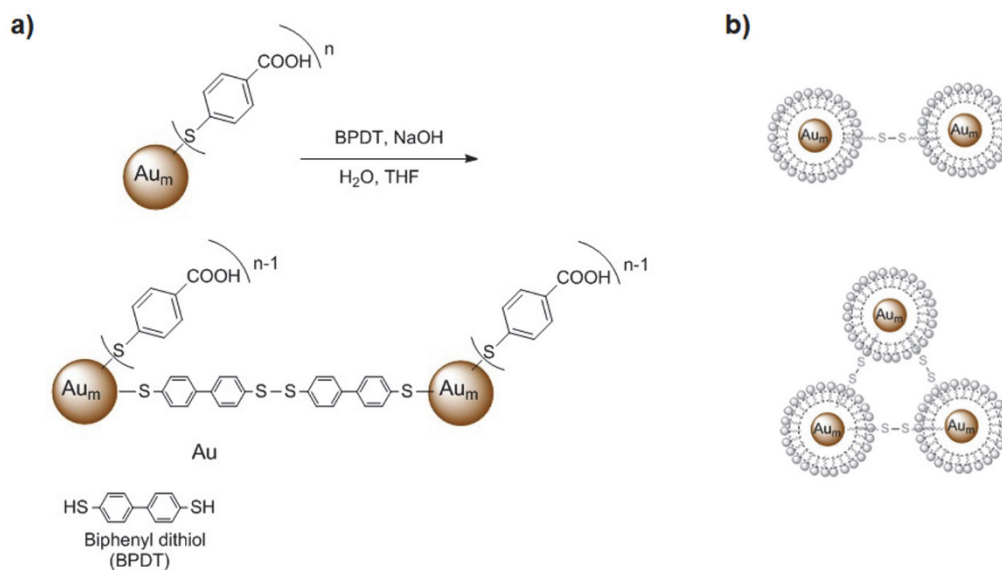
SCHEME 2 (**a**) Schematic representation of ligand exchange and linking reaction via two BPDT **1** molecules; (**b**) Example of dimeric and trimeric linking reaction products.[125]

4.2.2 Separation

The dithiol ligand-exchange procedure produces a large number of different sizes of superclusters (dimers, trimers, etc.). The crude synthesis products can be separated by gel electrophoresis based on mass and charge of the particle to a very high degree. Figure 14(a) shows the gel separation of monodisperse Au_{230}-clusters after bond formation with six different dithiol molecules. The indexes below each column specify the type of used dithiol, presented in Figure 13. The four lowest bands were labeled as M, D, T and Q bands. The most mobile M band consists of a monomeric form of clusters as indicated from transmission electron microscopy (TEM) images taken from the band after separation, shown in Figure 14(b). The bands appearing above the M bands show dominantly dimers for D bands, trimers for T bands and tetramers for Q bands, which were also confirmed by TEM.
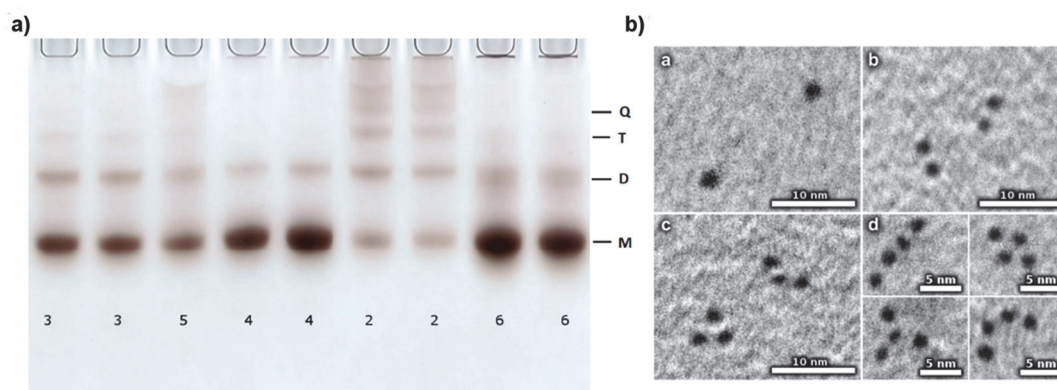
FIGURE 14 (**a**) PAGE gel showing bands of Au_{230}-nanoclusters linked with different dithiol molecules. Different dithiols are specified with the indexes below each column, the ratio of used dithiol-to-MPC was 2:1 (**b**) TEM micrographs showing (a) monomer from M band; (b) dimer from D band; (c) trimer from T band and (d) tetramer from Q band.[128]

The results indicate that the preparation of gold superstructures is completely general. Although all dithiols produce similar PAGE patterns, the yields of different oligomer fractions seem to be strongly related to the type of dithiol used.

Next, the reaction yields with different dithiol-to-MPC ratios of the most efficient BMM-BPy **2** linker were analyzed by the technique inspired by the densitometric analysis of Western blot.[126] A wet PAGE gel was scanned and the mean pixel intensity of each separated fraction was calculated. The obtained values were converted to absorbance values by using the conversion curve obtained from calibration.

The oligomer yields are strongly related to the dithiol:MPC ratio. The lowest 1:5 ratio showed that the reaction favors monomeric form of a cluster. The formation of higher-order structures increases exponentially with respect to the number of nanoclusters in oligomer when the dithiol-to-MPC ratio is increased from 1:5 to 1:2, 1:1 and 2:1. At higher dithiol-to-MPC ratios the reaction saturates, increasing the amount of large aggregates. The reaction yields did not have any significant dependence on time at equimolar ratio, indicating that reaction most likely reached an equilibrium after 15 minutes. The average experimental value of each fraction of gold MPCs for 3.5 hours in 2:1 dithiol-to-MPC ratio were for monomer 44%, dimer 27%, trimer 12%, tetramer 6% and for structures > 4 gold clusters 5%.

4.2.3 Linking mechanism

The ability to create and separate covalently linked dimers opens up interesting possibilities to study the mechanism and properties of these systems. In this study, the reaction mechanism of bond formation between atomically precise clusters and how many linkers are needed to bridge the clusters was investigated. The outcome of this study is built on experimental results supported by simulations. The distance analysis on pairs of covalently bound BPDT **1**

$Au_{102}(p\text{-MBA})_{44}$-nanoclusters was done by transmission electron microscopy, shown in Figure 15(b) (red). The center-to-center distances in linked Au_{102} dimers yielded a distribution spanning from 1.8 nm to 3.4 nm, suggesting that two nanoclusters could be linked by one, two or three BPDT **1** molecules.

The molecular dynamics (MD) simulations of the dimeric system was performed with Gromacs (Groningen Machine for Chemical Simulation) for fully protonated and deprotonated nanocluster systems, as shown in Figure 15(a). Although simulation yielded a stable, dimeric system linked through two BPDT **1** molecules, the possibility of having one, three or more BPDT **1** molecules was not excluded. The MD distance distribution for fully protonated system started from 2.2 nm and extended to 3.6 nm for fully deprotonated [Figure 15(b), grey&pink]. The extended distribution for fully deprotonated system could explain the experimental tail distribution, taking into account that in the solution clusters are mainly in deprotonated form during the measurements. In case of more than one linker molecule connecting the clusters, dithiols are most likely bridged by disulfide bonds connecting the clusters on both sides.
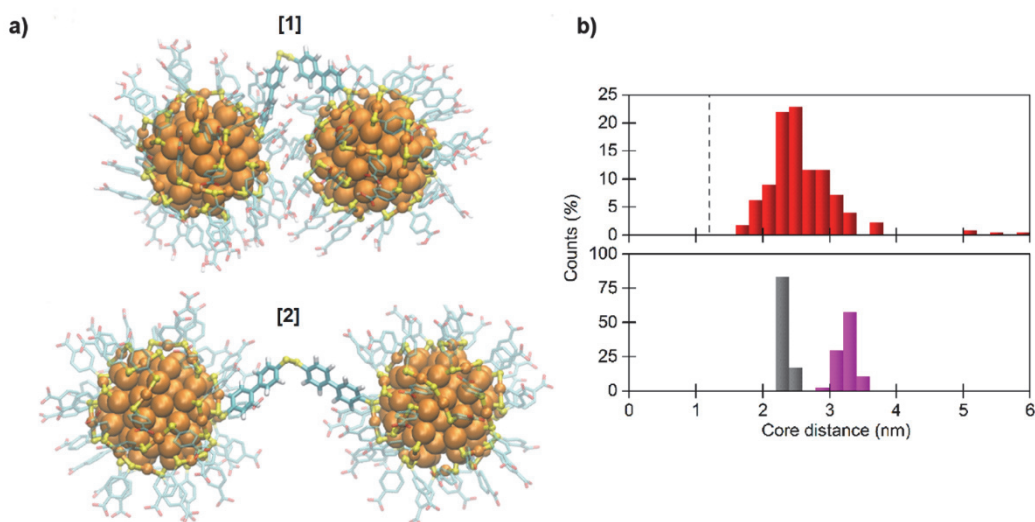

FIGURE 15 (**a**) Snapshot of MD simulation of [1] fully protonated and [2] fully deprotonated $Au_{102}MPC$–$(BPDT)_2$–$Au_{102}MPC$ in H_2O; (**b**) The distribution of center-to-center distances of the linked $Au_{102}MPC$ dimers from the TEM images (red) and from the simulation from fully protonated (grey) and fully deprotonated (pink) system in water.[125]

The bonding between dimeric structures of Au_{230}–nanoclusters linked with similarly sized BMM-BPy **2** molecules was studied by analyzing the reaction yields at different reaction conditions. The analysis was performed by a set of syntheses with different dithiol-to-gold clusters ratio followed by the PAGE run and scanning the gel with a desktop scanner. A detailed analysis of reaction yields showed that the formation of higher-order structures increases exponentially with respect to the number of nanoclusters in oligomer up to a certain point when only large aggregates are formed. The same trend was also

observed in TEM statistics, where fractions of dimer, trimer and higher oligomers were significantly higher comparing to a 1:5 dithiol-to-MPC ratio.

We speculate that similar behavior is observed in the polymerization reaction where the polymerization probability changes rapidly at low dithiol-to-MPC ratios and becomes saturated at higher ratios. Typically, polymerization processes are controlled by controlling time. We found no significant differences in the reaction yields after 0.25, 0.5, 3.5 and 7 hours, meaning that the reaction either reached the end or is in dynamic equilibrium. In our system, reaction equilibrium depends on ligand exchange rate, disulfide formation rate, ligand-exchange equilibrium between outgoing thiol and incoming dithiol, and disulfide equilibrium.

To simplify the problem, various hypotheses and assumptions were made to investigate the mechanism of covalently linked oligomers. Ligand-exchange and disulfide formation are the two primary competing processes in our system. Given the experimental data, ligand exchange is a fast and random process leading to the formation of a metastable state where gold nanoclusters have one, two or more ligands exchanged to dithiols. The simulation of this metastable state at equimolar ratio yielded 37% of NCs with no dithiol, 37% with one dithiol, 18% with two dithiols, 6%-three, and the remaining 2% have four or more dithiols. After ligand exchange process, two bridging possibilities were taken into account, formation of a single dithiol bridge (*direct linking*) or by two dithiol molecules with a disulfide bond between them (*indirect linking*). The two bridging possibilities were simulated taking into account the linking activity (fraction of dithiols that act as molecular bridges), ligand exchange as one irreversible process and ligand-exchange as continuous, two-way process that reaches a dynamic equilibrium.

Although simulation did not exclude direct linking, the best experimental match was found in case of *indirect linking*. Therefore, our system is most likely in a dynamic equilibrium where molecular bridges between oligomers are formed, by disulfide-bridged dithiols. Moreover, ligand-exchange is an ongoing and dynamic process leading to re-equilibration, where linked superstructures continuously form and break via ligand-exchange process. The simulated distribution of oligomer fractions reproduces the experiments very well when a chain length varies from single dithiol (35% linking activity) up to 2.85 dithiols. The results are in a good agreement with our previous findings on similarly sized BPDT **1** molecule, where chains of two, three or more dithiols formed dimers.

4.3 Optical properties of gold MPC superstructures

This chapter presents some of the optical studies of covalently linked gold MPC-based structures. The monomer, dimer and trimer fractions of BPDT **1** linked Au_{102}-clusters and Au_{230}-clusters were purified and analyzed by UV-vis spectroscopy. The study focused on changes in the UV-vis spectra upon linking and their characterization. Of interest was the coupling in covalently linked gold multimers. All the presented spectra were measured in D_2O at constant pH (8.3).

4.3.1 Analysis of $Au_{102}(p\text{-MBA})_{44}$ multimers

The UV-vis spectrum of covalently linked Au_{102}-nanoclusters resembles the spectra of the original clusters in the visible region, indicating that the cluster´s core remains intact after the linking reaction, shown in Figure 16 (red). In the UV region, an additional shoulder was observed in the linked clusters.

In the difference spectrum, the new feature at 308 nm closely resembles the transition of molecular BPDT linker (grey), being slightly red-shifted. We speculate that a new feature most likely originates from dithiol molecules being bound to gold core.
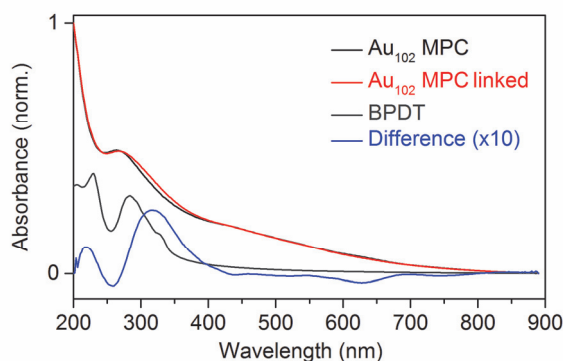

FIGURE 16 Normalized UV-vis spectra of Au_{102} reference cluster (black) and Au_{102} linked with BPDT molecule in D_2O (red), the arbitrarily scaled spectrum of molecular BPDT in THF (grey), and the difference spectrum of spectra before and after linking (linked Au_{102} MPC – unlinked Au_{102} MPC, blue, scaled by factor 10).[125]

4.3.2 Plasmon coupling in $Au_{210–230}(p\text{-MBA})_{70–80}$ multimers

To study the optical coupling of linked Au_{230}-nanoclusters the monomer (M), dimer (D) and trimer (T) fractions were purified. The UV-vis spectrum of each fraction is shown in Figure 17(a). To compare, the difference spectra between dimer-monomer (D-M) and trimer-monomer (T-M), are presented in Figure 16(b). The M, D and T spectra show the new features for the linked sample in the visible region. The difference spectra reveal slightly red-shifted two broad peaks at 630 nm and 810 nm, becoming more prominent in the T-M difference spectrum.
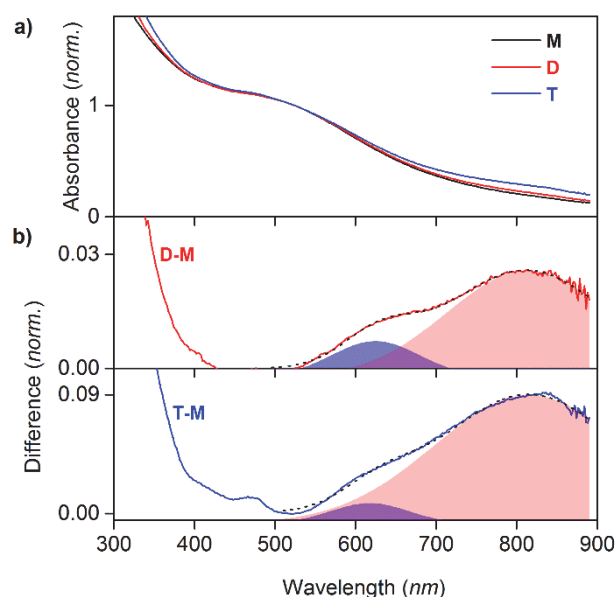
FIGURE 17 (**a**) Normalized UV-vis spectra of purified samples from M, D, and T bands. (**b**) Difference spectra between samples from D and M bands (top) as well as from T and M bands (bottom). The shaded areas indicate Gaussian components found in the data and the dashed curves indicate the totals.[125]

We argue that the observed transition at 630 nm originate from the fact that two clusters are in close proximity to each other, leading to optical coupling similar to dipolar plasmon bonding mode observed in big plasmonic nanoparticles. This behavior was also observed in case of a simple aggregation in low pH that led to hybridization of LSPR modes of nearby nanoparticles.

The peak at 810 nm, however, was not observed in the unlinked form of clusters and was sensitive to the number of gold cores forming the oligomer. We speculate, that this feature is related to the electronic structure of the molecular bridge, and could be assigned to a tunneling charge-transfer plasmon (tCTP), because its properties match with the tCTP mode. This feature has also been observed experimentally in much smaller linked systems.[103] Clearly, in our system the optical absorption changes upon linking and the peak at 810 nm is strongly related to linking.

From the DFT simulations we learned that the tCTP mode is possible to form when molecular states on the linker are close to the Fermi level of the system. Simulation of slightly larger plasmonic disulfide-bridged BPDT **1** $Au_{314}(SH)_{96}$ nanoclusters model have revealed that there exist several molecular states localized on the linker molecule that are energetically close to the combined nanocluster system [Figure 18(c)-(e)] Therefore, we assumed that these molecular states could act as a tunneling channel for the tCTP mode.
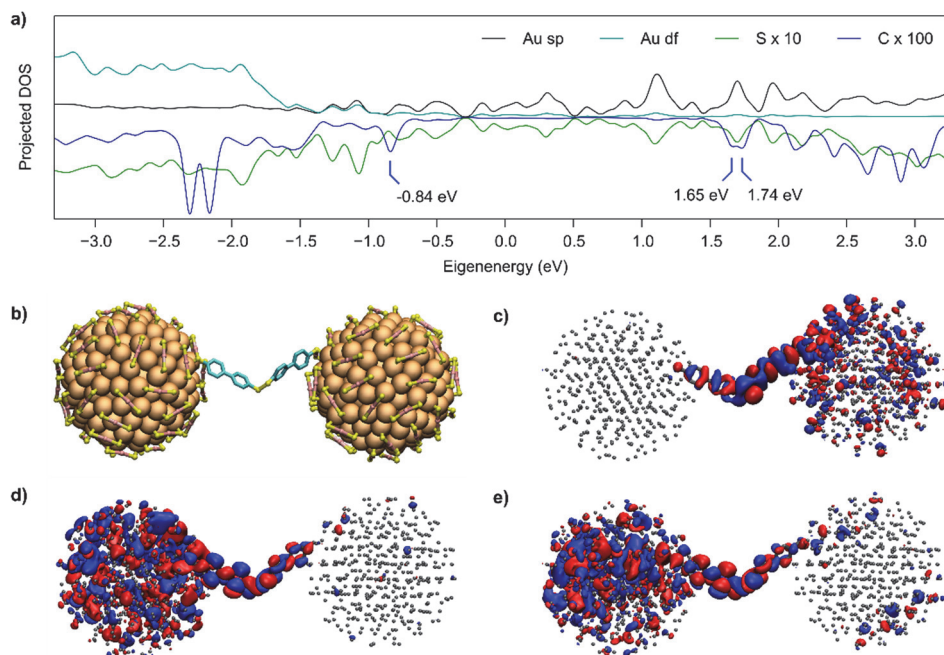
FIGURE 18 (**a**) Projected density of states for $Au_{314}(SH)_{95}$–BPDT–BPDT–$Au_{314}(SH)_{95}$ calculated using DFT. Projection to sulfur (green) is scaled by 10 and projection to carbon (blue) is scaled by 100 with respect to projection to s/p (black) and d/f (cyan) orbitals of gold. (**b**) Geometry of the $Au_{314}(SH)_{95}$–BPDT–BPDT–$Au_{314}(SH)_{95}$ dimer used in the calculation. Hydrogens are omitted for clarity. Isosurfaces for orbitals corresponding eigenenergies of (**c**) −0.84 eV, (**d**) 1.65 eV, and (**e**) 1.74 eV with respect to the Fermi level.[125]

4.4 Disulfide bridges: XPS and STEM-EELS atomic-scale structure analysis

The soon-to-be-published results presented in the last section of this thesis are an important extension to our previous studies. In this study, the atomic composition of the bridge between the Au_{230}-clusters was verified by X-ray photoelectron spectroscopy (XPS). A detailed analysis of sulfur core-level peaks confirms the presence of the disulfide bonds (R-S-S-R). The spatial analysis of scanning transmission electron microscope (STEM) images in combination with electron energy-loss spectroscopy (EELS) gives a structural confirmation of the molecular linkage between gold nanoclusters. These results validate our hypothesis of the proposed reaction mechanism and verify the chemical nature of the covalent bridge between covalently linked gold nanoclusters. This study will be published in the appropriate journal; hence, the results of this section are not shown here, but they are referred to the attached *manuscript submitted* in appendix (**IV**).

XPS measurements were utilized to confirm the presence of the disulfide bonds forming the covalently linked BMM-BPy **2** gold nanoclusters (Figure 1,

appendix **IV**). The photoemission data were collected at sulfur 2*p* and 2*s* core-levels and Au 4*f*, C 1*s*, and O 1*s* core-levels. In Figure 2(a) (appendix **IV**) the photoemission S 2*p* core-level spectrum shows two distinct components with two spin-orbit doublets with energies at ~162.5 eV and 164.6 eV. The first component with the energy at ~162.5 eV has been observed in the literature before, and was attributed to the sulfur atoms bonded to the gold atoms of the cluster (S-Au).

The second component however, at the 164.6 eV bonding energy is weak but still observable and it was previously attributed to the disulfide group that bridges dithiol molecules together (R-S-S-R). The weak signal is reasonable because the relative number of disulfide bridges is lower than that of the S-Au bonds in the sample. The 2*s* core-level spectrum shown in Figure 2(b) (appendix **IV**) was measured to confirm the presence of these two components. Typically, the components that are found in one transition should also be present in other transitions. In fact, similar components with the same binding energy were found in the sulfur 2*s* transition at ~228.5 eV and ~226.7 eV. In summary, we report that the components at 162.5 eV and 164.6 eV in the S 2*p* band, and 226.7 eV and 228.5 eV in the S 2*s* band, correspond respectively to S-Au and S-S bonds.

Covalently linked Au_{230}-trimers were further analyzed by aberration-corrected STEM coupled with EELS measurements. The EELS measurements were performed on a couple of regions of the sample. The EELS intensities were recorded at the core-loss regions, showing characteristic features for sulfur (165 eV), carbon (284 eV), nitrogen (401 eV) and oxygen (532 eV) [shown in Figure (3)b and S4, appendix **IV**]. The sulfur ionization edges were used to record energy-filtered images from the various sample areas to trace the presence of sulfur atoms, providing a spatial overview of the sulfur signals shown in Figure S5(a)—(d), (appendix **IV**). The acquired data set identified the spatial distribution of dominant features, i.e. high content of sulfur atoms in the cluster core; however, the analysis and observation of individual sulfur atoms is difficult. The signals corresponding to the sulfur atoms in the molecular bridge are weak, since these atoms are very few in numbers. Due to the resolution limits, it is perhaps not possible to differentiate two singlet sulfur signals coming from the disulfide bridge. To reveal the presence of sulfur signals between individually linked dimers or trimers, a detailed image analysis of sulfur elemental maps and cross-sectional profiles was performed.

The cross-section profiles of the sulfur intensities taken across the line indicated in the inset images are presented in Figure 4(a)—(d) and Figure S6 (appendix **IV**). In all presented cases, the most prominent features appear at the exact location of the core of the nanocluster, corresponding to the sulfur atoms at the ligand-gold core interface. Further analysis revealed the presence of signals with low counts located between the clusters. These signals correspond to sulfur signal and are highlighted with green rectangles in Figure 4(a)—(d) (appendix **IV**). This could indicate the presence of one disulfide-bridge linking two dithiol molecules. In some cases, the sulfur signal was not detected at all between the nanoclusters [Figure 4(c) and S7, appendix **IV**], meaning that the gold clusters are either connected by a direct link with a single dithiol molecule or the electron

beam has affected the structure of Au oligomers. Interestingly, in Figure 4(d) the vertical cyan line that passes through three nanoclusters shows two additional, weak sulfur peaks between the clusters. The nanoclusters are ~1.5 nm apart and the sulfur signals are spaced ~0.5 nm apart. This clearly indicated the presence of two disulfide molecular bridges linking three dithiol molecules between two gold nanoclusters.

These findings agree well with our previous study on the similarly sized but more rigid BPDT **1** dithiol molecule, where the disulfide bridge between BPDT **1** molecules linking the dimers was suggested, as discussed in paper **I**. Moreover, the presented results also agree with the hypothesis on reaction mechanism discussed in paper **II** between BMM-BPy **2** and Au_{230} nanoclusters, where the distance between two nanoclusters was on average found to be 1-2.85 dithiols long.

5 CONCLUSION

The work presented in this thesis yields a straightforward, up-scalable, robust synthesis to covalently bound water-soluble *para*-mercaptobenzoic acid (*p*-MBA) protected gold nanoclusters with known atomic precision. The covalent linking was achieved with two sizes of gold nanoclusters and different types of aryl dithiol molecules, producing in high yield large numbers of geometrical structures of linked gold clusters (dimer, trimers, etc.). The generality of this approach is critical for future studies of rational design of nanoscale devices with the precision of a single atom. Subsequently, a purification technique of individual covalently linked structures (dimer, trimer, etc.) was developed, resulting in efficient separation of a large number of different oligomer fractions to a very high degree. Controllable chemistry to synthesize well-defined gold superstructures and an efficient purification technique are the first steps towards understanding fundamental phenomena of electronic and optical properties of gold MPCs.

Our understanding of the reaction mechanism of superstructure formation is based on nearly constant distances observed in transmission electron microscopy (TEM) between singular Au clusters and the analysis of oligomer reaction yields. The data are in good agreement with simulations, suggesting that superstructures are dominantly linked by the formation of singular molecular bridges. The molecular bridges are most likely formed by the formation of S-S bonds between the terminal sulfurs of two (or more) dithiols connecting the clusters. The previously made hypothesis and the presence of the disulfide bonds was confirmed by using spectroscopic tools in combination with microscopic STEM imaging.

The system created in this work showed some inherently interesting optical properties. Formation of a covalent linkage between $Au_{210-230}(p\text{-MBA})_{70-80}$-clusters led to optical changes in the NIR spectral window (650-1350 nm), which for example, allow excitation by light in biological tissues. The first mode at 630 nm was associated with a mode similar to dipolar bonding modes, commonly observed in big nanoparticles. We speculate that the second mode at 810 nm might relate to the tCTP mode that was later observed by Bürgi group with much

smaller systems.[103] Nevertheless, the observed broad transition at 810 nm is related to the fact that the two clusters are connected together through a molecular linker.

The results presented in this work contribute to the understanding of plasmonic coupling through molecular bridges. The knowledge on how gold nanocluster oligomers are formed and understanding optical coupling through molecular bridges are essential in the development of nanoplasmonic sensors and devices. The ability to create superstructures opens new possibilities for fundamental studies of the internal motion of the clusters and the connecting ligands. Deeper understanding at the quantum level provides important information and generalizations, which will deepen our understanding of systems of large nanoparticles.

REFERENCES

1. David R.Lide, *Handbook of Chemistry and Physics*, CRC Press, **2005**.
2. Woldemar A Weyl, *Coloured Glasses*, The Society of Glass Technology, **1951**.
3. C. Louis and O. Pluchery, *Gold Nanoparticles for Physics, Chemistry and Biology*, Imperial Collage Press, **2012**.
4. T.Tsukuda and H.Häkkinen, *Protected Metal Clusters - From Fundamentals to Applications*, volume 9 of *Frontiers of Nanoscience*, Elsvier, **2015**.
5. R. Jin, C. Zeng, M. Zhou, and Y. Chen, Atomically Precise Colloidal Metal Nanoclusters and Nanoparticles: Fundamentals and Opportunities, *Chem. Rev.*, **2016**, 116, 10346–10413.
6. I. Chakraborty and T. Pradeep, Atomically Precise Clusters of Noble Metals: Emerging Link between Atoms and Nanoparticles, *Chem. Rev.*, **2017**, 117, 8208–8271.
7. H. Qian, M. Zhu, Z. Wu, and R. Jin, Quantum Sized Gold Nanoclusters with Atomic Precision, *Acc. Chem. Res.*, **2012**, 45, 1470–1479.
8. S. Malola, L. Lehtovaara, J. Enkovaara, and H. Häkkinen, Birth of the Localized Surface Plasmon Resonance in Monolayer-Protected Gold Nanoclusters, *Am. Chem. Soc.*, **2013**, 7, 10263–10270.
9. N. A. Sakthivel, S. Theivendran, V. Ganeshraj, A. G. Oliver, and A. Dass, Crystal Structure of Faradaurate-279: $Au_{279}(SPh\text{-}tBu)_{84}$ Plasmonic Nanocrystal Molecules, *J. Am. Chem. Soc.*, **2017**, 139, 15450–15459.
10. Y. Negishi, T. Nakazaki, S. Malola, S. Takano, Y. Niihori, W. Kurashige, S. Yamazoe, T. Tsukuda, and H. Häkkinen, A Critical Size for Emergence of Nonbulk Electronic and Geometric Structures in Dodecanethiolate-Protected Au Clusters, *J. Am. Chem. Soc.*, **2015**, 137, 1206–1212.
11. R. Philip, P. Chantharasupawong, H. Qian, R. Jin, and J. Thomas, Evolution of Nonlinear Optical Properties: From Gold Atomic Clusters to Plasmonic Nanocrystals, *Nano Lett.*, **2012**, 12, 4661–4667.
12. A. Mathew and T. Pradeep, Noble Metal Clusters: Applications in Energy, Environment, and Biology, *Noble Met. Clust. Appl. Energy, Environ. Biol.*, **2014**, 31, 1017–1053.
13. L. Y. Chen, C. W. Wang, Z. Yuan, and H. T. Chang, Fluorescent Gold Nanoclusters: Recent Advances in Sensing and Imaging, *Anal. Chem.*, **2015**, 87, 216–229.
14. T. Tsukuda, Toward an Atomic-Level Understanding of Size-Specific Properties of Protected and Stabilized Gold Clusters, *Bull. Chem. Soc. Jpn.*, **2012**, 85, 151–168.
15. Y. Negishi, K. Nobusada, and T. Tsukuda, Glutathione-Protected Gold Clusters Revisited: Bridging the Gap between Gold(I)-Thiolate Complexes and Thiolate-Protected Gold Nanocrystals, *J. Am. Chem. Soc.*, **2005**, 127, 5261–5270.
16. L. C. McKenzie, T. O. Zaikova, and J. E. Hutchison, Structurally Similar Triphenylphosphine-Stabilized Undecagolds, $Au_{11}(PPh_3)_7Cl_3$ and $[Au_{11}(PPh_3)_8Cl_2]Cl$, Exhibit Distinct Ligand Exchange Pathways with

Glutathione, *J. Am. Chem. Soc.*, **2014**, 136, 13426–13435.

17. J. Zhong, X. Tang, J. Tang, J. Su, and Y. Pei, Density Functional Theory Studies on Structure, Ligand Exchange, and Optical Properties of Ligand-Protected Gold Nanoclusters: Thiolate versus Selenolate, *J. Phys.Chem.C*, **2015**, 119, 9205–9214.

18. A. C. Templeton, W. P. Wuelfing, and R. W. Murray, Monolayer-Protected Cluster Molecules, *Acc. Chem. Res.*, **2000**, 33, 27–36.

19. H. Häkkinen, The Gold-Sulfur Interface at the Nanoscale, *Nat. Chem.*, **2012**, 4, 443–455.

20. D. E. Jiang, M. L. Tiago, W. Luo, and S. Dai, The 'Staple' Motif: A Key to Stability of Thiolate-Protected Gold Nanoclusters, *J. Am. Chem. Soc.*, **2008**, 130, 2777–2779.

21. M. Brust, M. Walker, D. Bethell, D. J. Schiffrin, and R. Whyman, Synthesis of Thiol-Derivatised Gold Nanoparticles in Two-Phase Liquid-Liquid System, *J.Chem. Soc., Chem. Commun.*, **1994**, 801–802.

22. R. L. Whetten, J. T. Khoury, M. M. Alvarez, S. Murthy, I. Vezmar, Z. L. Wang, P. W. Stephens, C. L. Cleveland, W. D. Luedtke, and U. Landman, Nanocrystal Gold Molecules, *Adv. Mater.*, **1996**, 8, 428–433.

23. P. D. Jadzinsky, G. Calero, C. J. Ackerson, D. A. Bushnell, and R. D. Kornberg, Structure of a Thiol Monolayer–Protected Gold Nanoparticle at 1.1 Å Resolution, *Science*, **2007**, 318, 430–433.

24. M. Walter, J. Akola, O. Lopez-Acevedo, P. D. Jadzinsky, G. Calero, C. J. Ackerson, R. L. Whetten, H. Grönbeck, and H. Häkkinen, A Unified View of Ligand-Protected Gold Clusters as Superatom Complexes, *PNAS*, **2008**, 105, 9157–9162.

25. Y. Gao, N. Shao, and X. C. Zeng, Ab Initio Study of Thiolate-Protected Au_{102} Nanocluster, *ACS Nano*, **2008**, 2, 1497–1503.

26. L. Cheng, C. Ren, X. Zhang, and J. Yang, New Insight into the Electronic Shell of $Au_{38}(SR)_{24}$: A Superatomic Molecule, *Nanoscale*, **2013**, 5, 1475–1478.

27. Y. Li, G. Galli, and F. Gygi, Electronic Structure of Thiolate-Covered Gold Nanoparticles: $Au_{102}(MBA)_{44}$, *ACS Nano*, **2008**, 2, 1896-1902.

28. Y. Levi-Kalisman, P. D. Jadzinsky, N. Kalisman, H. Tsunoyama, T. Tsukuda, D. A. Bushnell, and R. D. Kornberg, Synthesis and Characterization of $Au_{102}(p\text{-}MBA)_{44}$ nanoparticles, *J. Am. Chem. Soc.*, **2011**, 133, 2976–2982.

29. R. Jin, H. Qian, Z. Wu, Y. Zhu, M. Zhu, A. Mohanty, and N. Garg, Size Focusing: A Methodology for Synthesizing Atomically Precise Gold Nanoclusters, *J. Phys. Chem. Lett.*, **2010**, 1, 2903–2910.

30. Y. Negishi, C. Sakamoto, T. Ohyama, and T. Tsukuda, Synthesis and the Origin of the Stability of Thiolate-Protected Au_{130} and Au_{187} Clusters, *J.Phys.Chem.Soc*, **2012**, 3, 1624–1628.

31. H. Qian and R. Jin, Controlling Nanoparticles with Atomic Precision: The Case of $Au_{144}(SCH_2CH_2Ph)_{60}$, *Nano Lett.*, **2009**, 9, 4083–4087.

32. S. Vergara, D. A. Lukes, M. W. Martynowycz, U. Santiago, G. Plascencia-Villa, S. C. Weiss, M. J. De La Cruz, D. M. Black, M. M. Alvarez, X. López-

Lozano, C. O. Barnes, G. Lin, H. C. Weissker, R. L. Whetten, T. Gonen, M. J. Yacamán, and G. Calero, MicroED Structure of $Au_{146}(p\text{-MBA})_{57}$ at Subatomic Resolution Reveals a Twinned FCC Cluster, *J. Phys. Chem. Lett.*, **2017**, 8, 5523–5530.

33. H. Qian, Y. Zhu, and R. Jin, Atomically Precise Gold Nanocrystal Molecules with Surface Plasmon Resonance, *PNAS*, **2012**, 9, 696–700.

34. R. Jin, Atomically Precise Metal Nanoclusters: Stable Sizes and Optical Properties, *Nanoscale*, **2015**, 7, 1549–1565.

35. X. D. Zhang, D. Wu, X. Shen, P. X. Liu, F. Y. Fan, and S. J. Fan, In Vivo Renal Clearance, Biodistribution, Toxicity of Gold Nanoclusters, *Biomaterials*, **2012**, 33, 4628–4638.

36. C. Zhou, M. Long, Y. Qin, X. Sun, and J. Zheng, Luminescent Gold Nanoparticles with Efficient Renal Clearance, *Angew. Chemie - Int. Ed.*, **2011**, 50, 3168–3172.

37. R. Baronia, M. Singh, R. B. Gupta, S. Karuppiah, R. Kumar, J. Belz, R. Shanker, S. Sridhar, and S. P. Singh, Synthesis and Characterization of Multifunctional Gold Nanoclusters for Application in Radiation Therapy, *Int. J. Nanomedicine*, **2018**, 13, 113–115.

38. V. Marjomäki, T. Lahtinen, M. Martikainen, J. Koivisto, S. Malola, K. Salorinne, M. Pettersson, and H. Häkkinen, Site-Specific Targeting of Enterovirus Capsid by Functionalized Monodisperse Gold Nanoclusters, *Proc. Natl. Acad. Sci.*, **2014**, 111, 1277–1281.

39. M. Martikainen, K. Salorinne, T. Lahtinen, S. Malola, P. Permi, H. Häkkinen, and V. Marjomäki, Hydrophobic Pocket Targeting Probes for Enteroviruses, *Nanoscale*, **2015**, 7, 17457–17467.

40. Z. Wu and R. Jin, On the Ligand's Role in the Fluorescence of Gold Nanoclusters, *Nano Lett.*, **2010**, 10, 2568–2573.

41. W. Kurashige, M. Yamaguchi, K. Nobusada, and Y. Negishi, Ligand-Induced Stability of Gold Nanoclusters: Thiolate versus Selenolate, *J.Phys.Chem.Lett.*, **2012**, 3, 2649–2652.

42. E. Hutter and J. H. Fendler, Exploitation of Localized Surface Plasmon Resonance, *Adv. Mater.*, **2004**, 16, 1685–1706.

43. P. K. Jain, X. Huang, I. H. El-Sayed, and M. A. El-Sayed, Noble Metals on the Nanoscale: Optical and Photothermal Properties and Some Applications in Imaging, Sensing, Biology and Medicine, *Acc. Chem. Res.*, **2008**, 41, 1578–1586.

44. R. Jin, Atomically Precise Metal Nanoclusters: Stable Sizes and Optical Properties, **2015**, 15, 1549–1565.

45. E. Hukko, O. Loped-Acevedo, J. Koivisto, Y. Levi-Kalisman, R. D. Kornberg, M. Pettersson, and H. Häkkinen, Electronic and Vibrational Signatures of the $Au_{102}(p\text{-MBA})_{44}$ Cluster, *J. Am. Chem. Soc.*, **2011**, 133, 3752–3755.

46. T.-R. Tero, S. Malola, B. Koncz, E. Pohjolainen, S. Lautala, S. Mustalahti, P. Permi, G. Groenhof, M. Pettersson, and H. Häkkinen, Dynamic Stabilization of the Ligand-Metal Interface in Atomically Precise Gold

Nanoclusters Au_{68} and Au_{144} Protected by Meta-Mercaptobenzoic Acid, *ACS Nano*, **2017**, 11, 11872-11879.

47. M. Azubel, J. Koivisto, S. Malola, D. Bushnell, G. L. Hura, A. L. Koh, H. Tsunoyama, T. Tsukuda, M. Pettersson, H. Häkkinen, and R. D. Kornberg, Electron Microscopy of Gold Nanoparticles at Atomic Resolution, *Science*, **2014**, 345, 909–912.

48. M. Azubel, A. L. Koh, K. Koyasu, T. Tsukuda, and R. D. Kornberg, Structure Determination of a Water-Soluble 144-Gold Atom Particle at Atomic Resolution by Aberration-Corrected Electron Microscopy, *ACS Nano*, **2017**, 11, 11866–11871.

49. G. Salassa and T. Bürgi, NMR Spectroscopy: A Potent Tool for Studying Monolayer-Protected Metal Nanoclusters, *Nanoscale Horizons*, **2018**, 3, 457–463.

50. D.M. Chevrier, R. Yang, A. Chatt, and P. Zhang, Bonding Properties of Thiolate-Protected Gold Nanoclusters and Structural Analogs from X-ray Absorption Spectroscopy, *Nanotechnol. Rev.*, **2015**, 4, 193-206.

51. H. Häkkinen, M. Walter, and H. Grönbeck, Divide and Protect: Capping Gold Nanoclusters with Molecular Gold-Thiolate Rings, *J. Phys. Chem. B*, **2006**, 110, 9927–9931.

52. K. Salorinne, T. Lahtinen, S. Malola, J. Koivisto, and H. Häkkinen, Solvation Chemistry of Water-Soluble Thiol-Protected Gold Nanocluster Au_{102} from DOSY NMR Spectroscopy and DFT Calculations, *Nanoscale*, **2014**, 6, 7823–7826.

53. M. Azubel and R. D. Kornberg, Synthesis of Water-Soluble, Thiolate-Protected Gold Nanoparticles Uniform in Size, *Nano Lett.*, **2016**, 16, 3348–3351.

54. M. Zhu, H. Qian, and R. Jin, Thiolate-Protected Au_{20} Clusters with a Large Energy Gap of 2.1 eV, *J. Am. Chem. Soc.*, **2009**, 131, 7220–7221.

55. S. Mustalahti, P. Myllyperkiö, T. Lahtinen, S. Malola, K. Salorinne, T. R. Tero, J. Koivisto, H. Häkkinen, and M. Pettersson, Photodynamics of a Molecular Water-Soluble Nanocluster Identified as $Au_{130}(p\text{-MBA})_{50}$, *J. Phys. Chem. C*, **2015**, 119, 20224–20229.

56. S. Mustalahti, P. Myllyperkiö, T. Lahtinen, K. Salorinne, S. Malola, J. Koivisto, H. Häkkinen, and M. Pettersson, Ultrafast Electronic Relaxation and Vibrational Cooling Dynamics of $Au_{144}(SC_2H_4Ph)_{60}$ Nanocluster Probed by Transient Mid-IR Spectroscopy, *J. Phys. Chem. C*, **2014**, 118, 18233–18239.

57. C. Yi, M. a Tofanelli, C. J. Ackerson, and K. L. Knappenberger, Optical Properties and Electronic Energy Relaxation of Metallic $Au_{144}(SR)_{60}$ Nanoclusters, *J. Am. Chem. Soc.*, **2013**, 135, 18222–18228.

58. M. Zhu, C. M. Aikens, F. J. Hollander, G. C. Schatz, and R. Jin, Correlating the Crystal Structure of A Thiol-Protected Au_{25} Cluster and Optical Properties, *J. Am. Chem. Soc.*, **2008**, 130, 5883–5885.

59. S. Mustalahti, P. Myllyperkiö, S. Malola, T. Lahtinen, K. Salorinne, J. Koivisto, H. Häkkinen, and M. Pettersson, Molecule-Like Photodynamics

of Au$_{102}$(p-MBA)$_{44}$ Nanocluster, *ACS Nano*, **2015**, 9, 2328–2335.

60. J. Koivisto, X. Chen, S. Donnini, T. Lahtinen, H. Häkkinen, G. Groenhof, and M. Pettersson, Acid-Base Properties and Surface Charge Distribution of the Water-Soluble Au$_{102}$(p-MBA)$_{44}$ Nanocluster, *J. Phys. Chem. C*, **2016**, 120, 10041–10050.

61. C. L. Heinecke, T. W. Ni, S. Malola, V. Mäkinen, O. A. Wong, H. Häkkinen, and C. J. Ackerson, Structural and Theoretical Basis for Ligand Exchange on Thiolate Monolayer Protected Gold Nanoclusters, *J. Am. Chem. Soc.*, **2012**, 134, 13316–13322.

62. H. Qian and R. Jin, Ambient Synthesis of Au$_{144}$(SR)$_{60}$ Nanoclusters in Methanol, *Chem. Mater.*, **2011**, 23, 2209–2217.

63. Q. Yao, T. Chen, X. Yuan, and J. Xie, Toward Total Synthesis of Thiolate-Protected Metal Nanoclusters, *Acc. Chem. Res.*, **2018**, 51, 1338–1348.

64. Y. Chen, C. Zeng, D. R. Kau, and R. Jin, Tuning the Magic Size of Atomically Precise Gold Nanoclusters via Isomeric Methylbenzenethiols, *Am. Chem. Soc.*, **2015**, 15, 3603–3609.

65. O. A. Wong, W. S. Compel, and C. J. Ackerson, Combinatorial Discovery of Cosolvent Systems for Production of Narrow Dispersion Thiolate-Protected Gold Nanoparticles, *ACS Comb.Sci.*, **2015**, 17, 11–18.

66. Z. Wu, J. Suhan, and R. Jin, One-Pot Synthesis of Atomically Monodisperse , Thiol-Functionalized Au$_{25}$ Nanoclusters, *J. Mater. Chem.*, **2009**, 19, 622–626.

67. Q. Yao, Y. Yu, X. Yuan, Y. Yu, J. Xie, and J. Y. Lee, Two-Phase Synthesis of Small Thiolate-Protected Au$_{15}$ and Au$_{18}$ Nanoclusters, *Small*, **2013**, 9, 2696–2701.

68. X. Yuan, B. Zhang, Z. Luo, Q. Yao, D. T. Leong, N. Yan, and J. Xie, Balancing the Rate of Cluster Growth and Etching for Gram-Scale Synthesis of Thiolate-Protected Au$_{25}$ Nanoclusters with Atomic Precision, *Angew. Chemie - Int. Ed.*, **2014**, 53, 4623–4627.

69. C. Ackerson, P. D. Jadzinsky, D. A. Sexton, Jonathan Z. J.Bushnell, and R. D. Kornberg, Synthesis and Bioconjugation of 2 and 3 nm-Diameter Gold Nanoparticles, *Bioconjug. Chem.*, **2010**, 21, 214–218.

70. A. A. Sousa, J. T. Morgan, P. H. Brown, A. Adams, M. P. S. Jayasekara, G. Zhang, C. J. Ackerson, M. J. Kruhlak, and R. D. Leapman, Synthesis, Characterization, and Direct Intracellular Imaging of Ultrasmall and Uniform Glutathione-Coated Gold Nanoparticles, *Small*, **2012**, 8, 2277–2286.

71. C. J. Ackerson, P. D. Jadzinsky, and R. D. Kornberg, Thiolate Ligands for Synthesis of Water-Soluble Gold Clusters, *J. Am. Chem. Soc.*, **2005**, 127, 6550–6551.

72. L. M. Tvedte and C. J. Ackerson, Size-Focusing Synthesis of Gold Nanoclusters with p-Mercaptobenzoic Acid, *J. Phys. Chem. A*, **2014**, 118, 8124–8128.

73. Y. Negishi, K. Nobusada, and T. Tsukuda, Glutathione-Protected Gold Clusters Revisited : Bridging the Gap between Gold (I)-Thiolate Complexes and Thiolate-Protected Gold Nanocrystals, *J.Am.Chem.Soc.*, **2005**, 127, 5261–5270.

74. R. Tsunoyama, H. Tsunoyama, P. Pannopard, J. Limtrakul, and T. Tsukuda, MALDI Mass Analysis of 11 kDa Gold Clusters Protected by Octadecanethiolate Ligands, *J. Phys. Chem. C*, **2010**, 114, 16004–16009.

75. H. Qian, Y. Zhu, and R. Jin, Size-Focusing Synthesis, Optical and Electrochemical Properties of Monodisperse $Au_{38}(SC_2H_4Ph)_{24}$ Nanoclusters, *ACS Nano*, **2009**, 3, 3795–3803.

76. M. Zhu, E. Lanni, N. Garg, M. E. Bier, and R. Jin, Kinetically Controlled, High-Yield Synthesis of Au_{25} Clusters, *J. Am. Chem. Soc.*, **2008**, 130, 1138–1139.

77. T. Gregory Schaaff, G. Knight, M. N. Shafigullin, R. F. Borkman, and R. L. Whetten, Isolation and Selected Properties of a 10.4 kda Gold:Glutathione Cluster Compound, *J. Phys. Chem. B*, **1998**, 102, 10645–10646.

78. K. Kimura, N. Sugimoto, S. Sato, H. Yao, Y. Negishi, and T. Tsukuda, Size Determination of Gold Clusters by Polyacrylamide Gel Electrophoresis in a Large Cluster Region, *J.Phys.Chem.Soc*, **2009**, 113, 14076–14082.

79. N. Kothalawala, J. Lee-West IV, and A. Dass, Size-Dependent Molecule-Like to Plasmonic Transition in Water-Soluble Glutathione Stabilized Gold Nanomolecules, *Nanoscale*, **2014**, 6, 683–687.

80. A. M. Al-Somali, K. M. Krueger, J. C. Falkner, and V. L. Colvin, Recycling Size Exclusion Chromatography for the Analysis and Separation of Nanocrystalline Gold, *Anal. Chem.*, **2004**, 76, 5903–5910.

81. Y. Niihori, C. Uchida, W. Kurashige, and Y. Negishi, High-Resolution Separation of Thiolate-Protected Gold Clusters by Reversed-Phase High-Performance Liquid Chromatography, *Phys.Chem.Chem.Phys.*, **2016**, 18, 4251–4265.

82. Y. Niihori, M. Matsuzaki, T. Pradeep, and Y. Negishi, Separation of Precise Compositions of Noble Metal Clusters, *J. Am. Chem. Soc.*, **2013**, 135, 4946–4949.

83. H. Qian, Y. Zhu, and R. Jin, Isolation of Ubiquitous $Au_{40}(SR)_{24}$ Clusters from the 8 kDa Gold Clusters, *J. Am. Chem. Soc.*, **2010**, 132, 4583–4585.

84. A. Ghosh, O. F. Mohammed, and O. M. Bakr, Atomic-Level Doping of Metal Clusters, *Acc. Chem. Res.*, **2018**, 51, 3094–3103.

85. N. Goswami, K. Zheng, and J. Xie, Bio-NCs – The Marriage of Ultrasmall Metal Nanoclusters with Biomolecules, *Nanoscale*, **2014**, 6, 13328–13347.

86. J. Yan, B. K. Teo, and N. Zheng, Surface Chemistry of Atomically Precise Coinage−Metal Nanoclusters: From Structural Control to Surface Reactivity and Catalysis, *Acc. Chem. Res.*, **2018**, 51, 3084–3093.

87. Y. Negishi, K. Igarashi, K. Munakata, W. Ohgake, and K. Nobusada, Palladium Doping of Magic Gold Cluster $Au_{38}(SC_2H_4Ph)_{24}$: Formation of $Pd_2Au_{36}(SC_2H_4Ph)_{24}$ with Higher Stability than $A_{u38}(SC_2H_4Ph)_{24}$, *Chem. Commun.*, **2012**, 48, 660–662.

88. N. Kothalawala, C. Kumara, R. Ferrando, and A. Dass, $Au_{144-x}Pd_x(SR)_{60}$ Nanomolecules, *Chem. Commun.*, **2013**, 49, 10850–10852.

89. N. Barrabés, B. Zhang, and T. Bürgi, Racemization of Chiral $Pd_2Au_{36}(SC_2H_4Ph)_{24}$: Doping Increases the Flexibility of the Cluster Surface,

J. Am. Chem. Soc., **2014**, 136, 14361–14364.

90. Y. Niihori, W. Kurashige, M. Matsuzaki, and Y. Negishi, Remarkable Enhancement in Ligand-Exchange Reactivity of Thiolate-Protected Au_{25} Nanoclusters by Single Pd Atom Doping, *Nanoscale*, **2013**, 5, 508–512.

91. G. H. Woehrle, M. G. Warner, and J. E. Hutchison, Ligand Exchange Reactions Yield Subnanometer, Thiol-Stabilized Gold Particles with Defined Optical Transitions, *J. Phys. Chem. B*, **2002**, 106, 9979–9981.

92. M. J. Hostetler, A. C. Templeton, R. W. Murray, Dynamics of Place-Exchange Reactions on Monolayer-Protected Gold Cluster Molecules, *Langmuir*, **1999**, 15, 3782–3789.

93. G. Salassa, A. Sels, F. Mancin, and T. Bürgi, Dynamic Nature of Thiolate Monolayer in $Au_{25}(SR)_{18}$ Nanoclusters, *ACS Nano*, **2017**, 11, 12609–12614.

94. G. H. Woehrle, L. O. Brown, and J. E. Hutchison, Thiol-Functionalized, 1.5-nm Gold Nanoparticles Through Ligand Exchange Reactions: Scope and Mechanism of Ligand Exchange, *J. Am. Chem. Soc.*, **2005**, 127, 2172–2183.

95. Y. Shichibu, Y. Negishi, T. Tsukuda, and T. Teranishi, Large-Scale Synthesis of Thiolated Au_{25} Clusters via Ligand Exchange Reactions of Phosphine-Stabilized Au_{11} Clusters, *J. Am. Chem. Soc.*, **2005**, 127, 13464–13465.

96. C. Zeng, C. Liu, Y. Pei, and R. Jin, Thiol Ligand-Induced Transformation of $Au_{38}(SC_2H_4Ph)_{24}$ to $Au_{36}(SPh-t-Bu)_{24}$, *ACS Nano*, **2013**, 7, 6138–6145.

97. H. Qian, W. T. Eckenhoff, Y. Zhu, T. Pintauer, and R. Jin, Total Structure Determination of Thiolate-Protected Au_{38} Nanoparticles, *J. Am. Chem. Soc.*, **2010**, 132, 8280–8281.

98. S. Link, A. Beeby, S. FitzGerald, M. A. El-Sayed, T. G. Schaaff, and R. L. Whetten, Visible to Infrared Luminescence from a 28-atom Gold Cluster, *J. Phys. Chem. B*, **2002**, 106, 3410–3415.

99. E. S. Shibu, M. A. H. Muhammed, T. Tsukuda, and T. Pradeep, Ligand Exchange of $Au_{25}(SG)_{18}$ Leading to Functionalized Gold Clusters: Spectroscopy, Kinetics, and Luminescence, *J. Phys. Chem. C*, **2008**, 112, 12168–12176.

100. S. Knoppe, A. C. Dharmaratne, E. Schreiner, A. Dass, and T. Bürgi, Ligand Exchange Reactions on Au_{38} and Au_{40} Clusters: A Combined Circular Dichroism and Mass Spectrometry Study, *J. Am. Chem. Soc.*, **2010**, 132, 16783–16789.

101. S. Knoppe and T. Bürgi, The Fate of $Au_{25}(SR)_{18}$ Clusters Upon Ligand Exchange with Binaphthyl-Dithiol: Interstaple Binding vs. Decomposition, *Phys. Chem. Chem. Phys.*, **2013**, 15, 15816–15820.

102. L. Bega, D. Deschamps, S. Perrio, A. Gaumont, S. Knoppe, and T. Bürgi, Ligand Exchange Reaction on $Au_{38}(SR)_{24}$, Separation of $Au_{38}(SR)_{23}(SR')_1$ Regioisomers, and Migration of Thiolates, *J. Phys. Chem. C*, **2013**, 38, 21619–21625.

103. A. Sels, G. Salassa, F. Cousin, L.-T. Lee, and T. Bürgi, Covalently Bonded Multimers of $Au_{25}(SBut)_{18}$ as a Conjugated System, *Nanoscale*, **2018**, 10,

12754–12762.

104. M. C. Stark, M. A. Baikoghli, T. Lahtinen, S. Malola, L. Xing, M. Nguyen, N. Marina, A. Sikaroudi, V. Marjomäki, H. Häkkinen, and R. H. Cheng, Structural Characterization of Site-Modified Nanocapsid with Monodispersed Gold Clusters, *Sci. Rep.*, **2017**, 1–11.

105. A. K. Shaw and S. K. Pal, Quantum Clusters of Gold Exhibiting FRET, *J. Phys. Chem. C*, **2008**, 112, 14324–14330.

106. N. J. Halas, S. Lal, W. S. Chang, S. Link, and P. Nordlander, Plasmons in Strongly Coupled Metallic Nanostructures, *Chem. Rev.*, **2011**, 111, 3913–3961.

107. C. Sönnichsen, B. M. Reinhard, J. Liphardt, and A. P. Alivisatos, A Molecular Ruler Based on Plasmon Coupling of Single Gold and Silver Nanoparticles, *Nat. Biotechnol.*, **2005**, 23, 741–745.

108. S. Yampolsky, D. A. Fishman, S. Dey, E. Hulkko, M. Banik, E. O. Potma, and V. A. Apkarian, Seeing a Single Molecule Vibrate Through Time-Resolved Coherent Anti-Stokes Raman Scattering, *Nat. Photonics*, **2014**, 8, 650–656.

109. H. Cha, J. H. Yoon, and S. Yoon, Probing Quantum Plasmon Coupling Ysing Gold Nanoparticle Dimers with Tunable Interparticle Distances Down to the Subnanometer Range, *ACS Nano*, **2014**, 8, 8554–8563.

110. D. H. Tsai, T. J. Cho, F. W. Delrio, J. M. Gorham, J. Zheng, J. Tan, M. R. Zachariah, and V. A. Hackley, Controlled Formation and Characterization of Dithiothreitol-Conjugated Gold Nanoparticle Clusters, *Langmuir*, **2014**, 30, 3397–3405.

111. Z. Xie, I. Bâldea, C. E. Smith, Y. Wu, and C. D. Frisbie, Experimental and Theoretical Analysis of Nanotransport in Oligophenylene Dithiol Junctions as a Function of Molecular Length and Contact Work Function, *ACS Nano*, **2015**, 9, 8022–8036.

112. J. Akola, K. A. Kacprzak, O. Lopez-Acevedo, M. Walter, H. Grönbeck, and H. Häkkinen, Thiolate-Protected Au_{25} Superatoms as Building Blocks: Dimers and Crystals, *J. Phys. Chem. C*, **2010**, 114, 15986–15994.

113. V. R. Jupally, R. Kota, E. Van Dornshuld, D. L. Mattern, G. S. Tschumper, D. E. Jiang, and A. Dass, Interstaple Dithiol Cross-Linking in $Au_{25}(SR)_{18}$ Nanomolecules: A Combined Mass Spectrometric and Computational Study, *J. Am. Chem. Soc.*, **2011**, 133, 20258–20266.

114. Nonappa, T. Lahtinen, J. S. Haataja, T. R. Tero, H. Häkkinen, and O. Ikkala, Template-Free Supracolloidal Self-Assembly of Atomically Precise Gold Nanoclusters: From 2D Colloidal Crystals to Spherical Capsids, *Angew. Chem. Int. Ed.*, **2016**, 55, 16035–16038.

115. D. Bahena, N. Bhattarai, U. Santiago, A. Tlahuice, A. Ponce, S. B. H. Bach, B. Yoon, R. L. Whetten, U. Landman, and M. J.Yacamán, STEM Electron Diffraction and High-Resolution Images Used in the Determination of the Crystal Structure of the $Au_{144}(SR)_{60}$ Cluster, *J. Phys. Chem. Lett.*, **2013**, 4, 975–981.

116. M. W. Heaven, A. Dass, P. S. White, K. M. Holt, and R. W. Murray, Crystal Structure of the Gold Nanoparticle [N(C$_8$H$_{17}$)$_4$][Au$_{25}$(SCH$_2$CH$_2$Ph)$_{18}$], *J. Am. Chem. Soc.*, **2008**, 130, 3754–3755.

117. A. L. Koh, K. Bao, I. Khan, W. E. Smith, G. Kothleitner, P. Nordlander, S. A. Maier, and D. W. Mccomb, Electron Energy-Loss Spectroscopy (EELS) of Surface Plasmons in Single Silver Nanoparticles and Dimers: Influence of Beam Damage and Mapping of Dark Modes, *ACS Nano*, **2009**, 3, 3015–3022.

118. J. B. Tracy, M. C. Crowe, J. F. Parker, O. Hampe, C. A. Fields-Zinna, A. Dass, and R. W. Murray, Electrospray Ionization Mass Spectrometry of Uniform and Mixed Monolayer Nanoparticles: Au$_{25}$[S(CH$_2$)$_2$Ph]$_{18}$ and Au$_{25}$[S(CH$_2$)$_2$Ph]$_{18-x}$(SR)$_x$, *J. Am. Chem. Soc.*, **2007**, 129, 16209–16215.

119. A. Dass, A. Stevenson, G. R. Dubay, J. B. Tracy, and R. W. Murray, Nanoparticle MALDI-TOF Mass Spectrometry Without Fragmentation: Au$_{25}$(SCH$_2$CH$_2$Ph)$_{18}$ and Mixed Monolayer Au$_{25}$(SCH$_2$CH$_2$Ph)$_{18-x}$(L)$_x$, *J. Am. Chem. Soc.*, **2008**, 130, 5940–5946.

120. G. Plascencia-Villa, B. Demeler, R. L. Whetten, W. P. Griffith, M. Alvarez, D. M. Black, and M. José-Yacamán, Analytical Characterization of Size-Dependent Properties of Larger Aqueous Gold Nanoclusters, *J. Phys. Chem. C*, **2016**, 120, 8950–8958.

121. J. Koivisto, K. Salorinne, S. Mustalahti, T. Lahtinen, S. Malola, H. Häkkinen, and M. Pettersson, Vibrational Perturbations and Ligand-Layer Coupling in a Single Crystal of Au$_{144}$(SC$_2$H$_4$Ph)$_{60}$ Nanocluster, *J. Phys. Chem. Lett.*, **2014**, 5, 387–392.

122. J. Koivisto, S. Malola, C. Kumara, A. Dass, H. Häkkinen, and M. Pettersson, Experimental and Theoretical Determination of the Optical Gap of the Au$_{144}$(SC$_2$H$_4$Ph)$_{60}$ Cluster and the (Au/Ag)$_{144}$(SC$_2$H$_4$Ph)$_{60}$ Nanoalloys, *J. Phys. Chem. Lett.*, **2012**, 3, 3076–3080.

123. K. Salorinne, S. Malola, O. A. Wong, C. D. Rithner, X. Chen, C. J. Ackerson, and H. Häkkinen, Conformation and Dynamics of the Ligand Shell of a Water-Soluble Au$_{102}$ Nanoparticle, *Nat. Commun.*, **2016**, 7, 1-8.

124. K. Salorinne, T. Lahtinen, J. Koivisto, E. Kalenius, M. Nissinen, M. Pettersson, and H. Häkkinen, Nondestructive Size Determination of Thiol-Stabilized Gold Nanoclusters in Solution by Diffusion Ordered NMR Spectroscopy, *Anal. Chem.*, **2013**, 85, 3489–3492.

125. T. Lahtinen, E. Hulkko, K. Sokołowska, T. R. Tero, V. Saarnio, J. Lindgren, M. Pettersson, H. Häkkinen, and L. Lehtovaara, Covalently Linked Multimers of Gold Nanoclusters Au$_{102}$(*p*-MBA)$_{44}$ and Au$_{\sim250}$(*p*-MBA)$_n$, *Nanoscale*, **2016**, 8, 18665–18674.

126. A. Gürtler, N. Kunz, M. Gomolka, S. Hornhardt, A. A. Friedl, K. McDonald, J. E. Kohn, and A. Posch, Stain-Free Technology as a Normalization Tool in Western Blot Analysis, *Anal. Biochem.*, **2013**, 433, 105–111.

127. K. Sokołowska, S. Malola, M. Lahtinen, V. Saarnio, P. Permi, K. Koskinen, M. Jalasvuori, H. Häkkinen, L. Lehtovaara, and T. Lahtinen, Towards Controlled Synthesis of Water-Soluble Gold Nanoclusters: Synthesis and Analysis, *J. Phys. Chem. C*, **2019**, 123, 2602–2612.

128. K. Sokołowska, E. Hulkko, L. Lehtovaara, and T. Lahtinen, Dithiol-Induced Oligomerization of Thiol-Protected Gold Nanoclusters, *J. Phys. Chem. C*, **2018**, 122, 12524–12533.

ORIGINAL PAPERS

I

COVALENTLY LINKED MULTIMERS OF GOLD NANOCLUSTERS Au$_{102}$(p-MBA)$_{44}$ AND Au~$_{250}$(p-MBA)$_{n}$

by

Tanja Lahtinen, Eero Hulkko, Karolina Sokołowska, Tiia-Riikka Tero,
Ville Saarnio, Johan Lindgren, Mika Pettersson, Hannu Häkkinen
and Lauri Lehtovaara 2016

Author(s): Lahtinen, Tanja; Hulkko, Eero; Sokołowska, Karolina; Tero, Tiia-Riikka; Saarnio, Ville; Lindgren, Johan; Pettersson, Mika; Häkkinen, Hannu; Lehtovaara, Lauri

Title: Covalently linked multimers of gold nanoclusters Au102(p-MBA)44 and Au250(p-MBA)n

Year: 2016

Version:

Journal Name

ARTICLE

Covalently linked multimers of gold nanoclusters Au$_{102}$(*p*-MBA)$_{44}$ and Au$_{\sim250}$(*p*-MBA)$_n$

Tanja Lahtinen[a‡], Eero Hulkko[a‡], Karolina Sokołowska[a], Tiia-Riikka Tero[a], Ville Saarnio[a], Johan Lindgren[a], Mika Pettersson[a*], Hannu Häkkinen[a,b*], Lauri Lehtovaara[a*]

We present synthesis, separation, and characterization of covalently-bound multimers of *para*-mercaptobenzoicacid (*p*-MBA) protected gold nanoclusters. The multimers were synthesized by performing a ligand-exchange reaction of pre-characterized Au$_{102}$(*p*-MBA)$_{44}$ nanocluster with biphenyl-4,4'-dithiol (BPDT). The reaction products were separated using gel electrophoresis yielding several distinct bands. The bands were analyzed with transmission electron microscopy (TEM) revealing monomer, dimer, and trimer fractions of the nanocluster. TEM analysis of dimers in combination with molecular dynamics simulations suggest that the nanoclusters are covalently bound via a disulfide bridge between BPDT molecules. The linking chemistry is not specific to Au$_{102}$(*p*-MBA)$_{44}$. The same approach yields multimers also for a larger monodisperse *p*-MBA –protected cluster of approximately 250 gold atoms, Au$_{\sim250}$(*p*-MBA)$_n$. Whereas the Au$_{102}$(*p*-MBA)$_{44}$ is not plasmonic, Au$_{\sim250}$(*p*-MBA)$_n$ nanocluster supports localized surface plasmon resonance (LSPR) at 530 nm. Multimers of Au$_{\sim250}$(*p*-MBA)$_n$ exhibit additional transitions in their UV-vis spectrum at 630 nm and at 810 nm, indicating presence of hybridized LSPR modes. Well-defined structure and relatively small size make these systems excellent candidates for connecting *ab initio* theoretical studies and experimental quantum plasmonics. Moreover, our work opens new possibilities in controlled synthesis of advanced monodisperse nanocluster superstructures.

Introduction

Nanoparticles (NPs) and their superstructures have attracted a lot of interest in fundamental research as well as in nanotechnological applications. The main reason is that physicochemical properties of nanoparticles are often strikingly different from their bulk counterparts and depend on composition, size, shape, and internal structure of the nanoparticles.[1,2] The properties of superstructures are influenced by their immediate surroundings including other nanoparticles. For example, optical spectrum of metal nanoparticles is dominated by localized surface plasmon (LSPR) that hybridizes with LSPRs of other nearby NPs.[3] The hybridization leads to formation of "hotspots" in between of the NPs, where electromagnetic field intensity increases orders of magnitudes. This had led to many applications. For example, nanoparticle dimers can act as nanoscale distance

probes because of their sensitivity to interparticle spacing.[4,5] The field enhancement has been employed, for example, in surface enhanced Raman spectroscopy[6], where sensitivity has reached single molecule level[7].

There exist several different approaches to fabricate NP assemblies and superstructures. The most straightforward is to simply aggregate NPs.[8] More stable structures can be achieved with polymer or silica encasing[9,10] or templating polymer layers[11]. Lithography has been extensively used to fabricate plasmonic nanoparticle assemblies in a controlled way.[12] However, for several applications, it would be desirable to have a controlled, wet-chemistry synthesis of superstructures. Successful wet-chemistry approaches based on self-assembly has been demonstrated, for example, with DNA-templating[13] and with several different molecular linkers[14-18].

Colloidal nanoparticles, in general, have a serious drawback from the chemical point-of-view. Their structure is not well-defined at the atomic level, and typical nanoparticle synthesis produces a polydisperse sample of different sizes, shapes, and surface structures.[5] This seriously hinders synthesis of homogeneous NP superstructures, and experiments that require atomic-level control, for example, LSPR hybridization through molecular states, are extremely difficult to carry out reproducibly.

Monolayer protected clusters (MPC) are a special kind of NPs which have a well-defined atomic structure that can be accurately determined by mass spectrometry and by single-crystal X-ray diffraction similar to small molecules.[19] For

a. *Department of Chemistry, Nanoscience Center, University of Jyväskylä, P.O. Box 35, 40014 Jyväskylä, Finland*
b. *Department of Physics, Nanoscience Center, University of Jyväskylä, P.O. Box 35, 40014 Jyväskylä, Finland*
† These authors contributed equally.
* Emails: lauri.lehtovaara@jyu.fi, hannu.j.hakkinen@jyu.fi, mika.j.pettersson@jyu.fi

example, the crystal structure of *para*-mercaptobenzoicacid (*p*-MBA) protected $Au_{102}(p\text{-MBA})_{44}$ cluster, used in this work, shows a core of 79 gold atoms protected by 19 RS–Au–SR and two $Au_2(SR)_3$ units in a well-defined motif.[20,21]

The atomically precise structures of MPC have enabled accurate studies of their chemistry. $Au_{102}(p\text{-MBA})_{44}$ and other MPCs are known to have preferred sites for ligand exchange reactions, i.e., specific ligands are exchanged with higher probability than others.[22,23] A well-defined structure with unequal ligand-exchange activities provides a basis for controlled synthesis of homogeneous NP superstructures.

An additional benefit of using MPCs to study fundamental aspects of NP superstructures is that depending on the size and shape of the metallic core, the electronic structure of MPC can change from discrete molecular-like energy levels[19], to semiconducting[24,25], and finally to metallic continuum[26,27]. The changes in the electronic structure are reflected to their physicochemical properties, for example, UV-vis spectrum changes from discrete peaks[19], to continuum[25], and finally to a spectrum with clear LSPR[26,27].

The well-defined atomic structure, preferred sites for ligand exchange, and possibility to approach nanoparticle limit from below in a controlled manner make MPCs excellent candidates for accurate studies of emergent properties in NP superstructures. Moreover, MPC superstructures and their possible MPC specific properties are inherently interesting themselves having potential applications in chemical sensing and biomedical imaging[28]. In this paper, we demonstrate a synthesis of small covalently linked MPC superstructures via ligand-exchange reaction where a biphenyl-4-4'-dithiol (BPDT) replaces a *p*-MBA ligand and creates a covalent disulfide bridge with another BPDT forming a MPC multimer. Furthermore, we show that emergence of plasmonic coupling can be studied using these MPC multimers. Previously, MPC dimers have been demonstrated using dynamic diglyme bonding[29], however, in our approach, dithiol-bridged MPCs form a covalently bound system.

The rest of the paper is structured as follows. We begin by describing synthesis and purification of $Au_{102}(p\text{-MBA})_{44}$ and $Au_{\sim250}(p\text{-MBA})_n$ clusters and their BPDT linked multimers (see Fig. 1). Experimental analysis methods are described next, followed by computational methods. Results and discussion begins with characterization of $Au_{102}(p\text{-MBA})_{44}$ and analysis of $Au_{\sim250}(p\text{-MBA})_n$ followed by analysis of their multimers. TEM analyses and molecular dynamics (MD) simulations are combined to explain the nature of the linking. In the last part of the paper, we focus on UV-vis spectroscopy of $Au_{\sim250}(p\text{-MBA})_n$ multimers and interpretation of observed plasmonic features supported by density functional theory simulations.

Materials and methods

Materials

All reagents were commercial and used as received unless otherwise mentioned.

Synthesis of nanoclusters. Two different MPCs were synthesized to be used as starting material for the multimer synthesis. The smaller nanocluster, $Au_{102}(p\text{-MBA})_{44}$, has been extensively studied before.[20,21,22,24,25,30,31,32] We followed its previously reported synthesis given in Ref. 30. The larger nanocluster of approximately 250 gold atoms and unknown number of *p*-MBAs (labelled as $Au_{\sim250}(p\text{-MBA})_n$) required a treatment of the initial $Au_x(p\text{-MBA})_y$, polymerization step at pH of ~11 before reduction that nucleates the growth of the metal core.[33] The syntheses of both sizes produced mg-quantities of material. Detailed description of the syntheses and purification are given in ESI.

Synthesis of nanocluster multimers. The ligand exchange reaction leading to multimers of $Au_{102}(p\text{-MBA})_{44}$ was carried out as follows. Stock solution of BPDT in THF was added to water solution of $Au_{102}(p\text{-MBA})_{44}$ (2:1 ratio of thiol groups vs. gold clusters) together with a few drops of NaOH. The reaction was quenched after 3.5 hours with isopropanol and 5 M NH_4OAc, and the resulting black precipitate was centrifuged. The supernatant was removed and the pellet was washed to remove any remaining free thiol residue. The ligand-exchange reaction of $Au_{\sim250}(p\text{-MBA})_n$ was carried out the same way.

Separation of nanocluster multimers. Gel electrophoresis (PAGE) was used to separate reaction products of $Au_{102}(p\text{-MBA})_{44}$ and $Au_{\sim250}(p\text{-MBA})_n$ multimer syntheses. Preparative PAGE was performed with a 2 mm thick gel. Different PAGE bands were mechanically cut from the acrylamide gel and dissolved separately in small amount of water. Clusters were
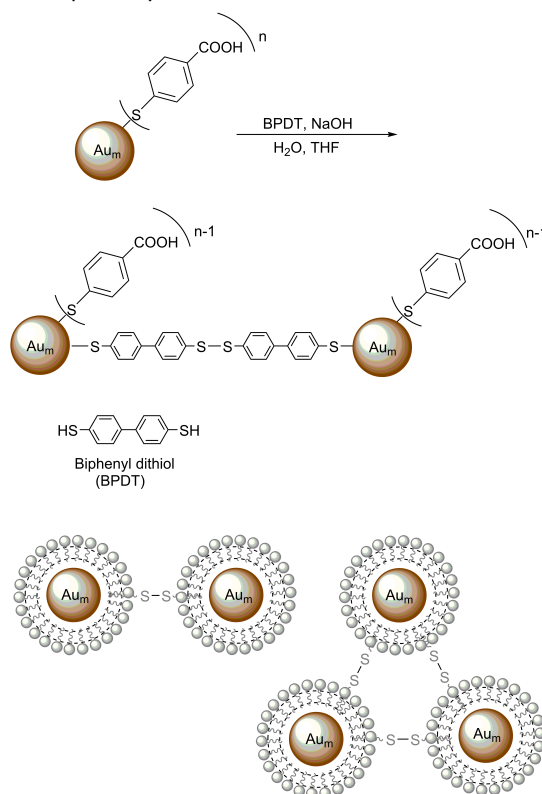

Fig. 1 Schematic representation of the ligand exchange and linking reaction. The scheme shows the molecular structure of biphenyl-4,4'-dithiol (BPDT), the covalent linking via two BPDTs as an example, and examples of dimeric and trimeric reaction products.

ARTICLE

allowed to dissolve from the gel until significant coloration of the solution was observed (typically overnight). Solution was filtered through a centrifugal filter tube with a pore size of 0.22 μm (time: 60 s, speed: rcf = 1.0) to remove excess gel residues. The separation procedure was repeated for the separated bands to obtain higher purity for TEM imaging and optical absorption spectroscopy.

Experimental techniques

Polyacrylamide gel electrophoresis (PAGE). PAGE was run on a 15 or 20 % polyacrylamide gel (29:1 acrylamide:bisacrylamide) using 2X TBE run buffer in a Bio-Rad Mini-Protean Tetra System gel electrophoresis apparatus at 130 V.

Mass spectrometry (MS). Electrospray ionization mass spectrum of for $Au_{102}(p\text{-MBA})_{44}$ sample was measured at the University of Tokyo using a homemade TOF mass spectrometer with a similar procedure and parameters as previously reported in Ref. 31. The sample was dissolved in 50% (v/v) methanol/water containing 0.07% triethylamine.

Nuclear magnetic resonance (NMR) spectroscopy. ^{1}H NMR spectra were recorded on a Bruker Avance DRX 300 MHz (for $Au_{102}(p\text{-MBA})_{44}$) and 400 MHz (for $Au_{\sim250}(p\text{-MBA})_n$) spectrometers.

UV-vis spectroscopy. Optical absorption measurements were done with Perkin Elmer Lambda 850 UV/Vis -spectrometer with 2 nm resolution.

Transmission electron microscopy (TEM) and image analysis. TEM samples were prepared by drop-casting 40 mL of dilute deionized water solution of linked nanoclusters on a glow discharged 400 mesh holey carbon copper grid (Ted-Pella ultrathin c). Solution was allowed to deposit for 15 min, after which excess sample was removed and grid was allowed to dry under vacuum overnight. Samples were imaged with 0.26 nm point resolution using JEOL JEM-1400HC TEM operated at 80 kV or 120 kV, equipped with bottom mounted 11 Megapixel CCD camera (Olympus SIS Quemesa).

TEM images were analyzed by semi-automatic procedure using in-house developed code. First, a blob detector filter was applied to TEM images, where the filter is difference of two Gaussians of widths σ and 2σ, and the value of σ depends on TEM magnification. After the automatic blob detection, the found particles were verified by a human, and any false positives were removed from further analysis. A 2D Gaussian function was fitted to a slightly smoothed TEM intensity around each detected and verified particle. Parameters of the fitted 2D Gaussians are stored for further analysis.

Exposure time for determining particle size was chosen not to saturate TEM images at the centers of particles. Size of the particle is reported as the average of the long and short axis full widths at half maximum (FWHM). For example, the crystal structure of $Au_{102}(p\text{-MBA})_{44}$ yields FWHM of 1.1 nm when each atom in the crystal structure is represented as a Gaussian charge distribution with intensity proportional to atomic number and width equal to 0.2 nm.

Computational methods

Molecular dynamics. The molecular dynamics (MD) simulations were performed with Gromacs 4.6.7[34] using periodic boundary conditions; leap-frog integrator with 2 fs time step; PME electrostatics with 1.0 nm cut-off and 0.12 nm grid spacing; and Lennard-Jones interaction with 1.0 nm cut-off and dispersion correction for energy and pressure. Simulated structures were placed in the center of cubic box and then solvated using TIP3P water model. Counterions (Na^+) were added, when needed, to neutralize the system. All simulations model NPT ensemble using velocity-rescale thermostat (reference temperature 298.15 K) and Berendsen barostat (reference pressure 1 bar). Total simulation time was 100 ns and sampling was started after 50 ns.

The force field parameters and charges for the gold-sulphur units, and deprotonated and protonated p-MBA ligands were obtained from Ref. 35. Existing force field parameters in AMBER12[36] were used for the BPDT molecule. The partial charges for BPDT were calculated using structures consisting of one, two, or three BPDT(s) capped by gold atoms at the ends. The ground state geometries of the structures were obtained using Gaussian09 software[37], B3LYP functional, def2-TZVP basis set, and W06 density fitting. The MD partial charges were calculated using Ambertools12[36] and RESP charge fitting procedure[38] in two stages with the charge of gold atoms set to zero. Radius of gold atoms was set to 0.17 nm. The partial charges can be found in ESI, Table S1. The force field parameters for BPDT linker molecules and for the atom types are listed in ESI, Table S2.

Dimeric $Au_{102}(p\text{-MBA})_{43} - (BPDT)_n - Au_{102}(p\text{-MBA})_{43}$ systems for molecular dynamics were constructed by replacing the p-MBA ligand labeled as "pMBA2" in Ref. 22 by a BPDT molecule. If structure contained more than one BPDT molecule, a disulfide bridge (RS–SR) was formed between BPDT molecules.

Density functional theory. The density functional theory (DFT) calculations were performed using GPAW 0.10.0[39], GPAW setups 0.9.11271 and PBE exchange-correlation functional. The initial structure for DFT simulations was taken from a MD simulation of deprotonated $Au_{102}(p\text{-MBA})_{43} - (BPDT)_n - Au_{102}(p\text{-MBA})_{43}$ where core-to-core distance was 3.4 nm. Both $Au_{102}(p\text{-MBA})_{43}BPDT$ fragments were replaced by $Au_{314}(SH)_{96}$ from Malola et al.[40] in a such way that gold atoms in Au–SH–Au–SH–Au units of $Au_{314}(SH)_{96}$ were aligned with the respective gold atoms of Au–BPDT–Au–p-MBA–Au units of $Au_{102}(p\text{-MBA})_{43}BPDT$. The geometry of BPDT–BPDT linker was relaxed in a system where only Au–BPDT–Au–SH–Au units were included in the DFT calculation and all gold atoms were fixed.

Results and Discussion

Characterization of $Au_{102}(p\text{-MBA})_{44}$. The purified product of $Au_{102}(p\text{-MBA})_{44}$ synthesis was analyzed using PAGE, NMR, MS, TEM, and UV-vis. The synthesis product showed up as a single distinct band in PAGE (see Fig. 2, and ESI, Fig. S1) indicating a monodisperse MPC. MPC was identified as $Au_{102}(p\text{-MBA})_{44}$

based on its NMR and mass spectra. Electrospray ionization mass spectrum (see ESI, Fig. S2) shows peaks that correspond to different mass to charge ratios of partially deprotonated $Au_{102}(p\text{-}MBA)_{44}$, and the NMR spectrum (see ESI, Fig. S3) reproduces the characteristic NMR fingerprint of $Au_{102}(p\text{-}MBA)_{44}$.[32] UV-vis spectrum (see Fig. 3) and TEM diameter of 1.2 ± 0.3 nm (see ESI, Fig. S4) are also in agreement with previous studies.[20,25,31]

Analysis of $Au_{\sim250}(p\text{-}MBA)_n$. Previous studies have shown that MPCs in this size range have preferred sizes,[26,27,41] and the sizes appear as individual bands in PAGE.[41,42] Product of $Au_{\sim250}(p\text{-}MBA)_n$ synthesis forms a single distinct band in PAGE (see Fig. 2) indicating a monodisperse MPC. The band had lower mobility than $Au_{102}(p\text{-}MBA)_{44}$ in the PAGE run indicating larger size (see ESI, Fig. S1A). This is consistent with TEM analysis, that yields 1.6 ± 0.3 nm core diameter (see ESI, Fig. S4). A rough estimate for the number of gold atoms can be obtained by assuming relatively similar shape and density for the two MPCs ($N_{102}/V_{102} = N_x/V_x$), and then scaling the number of gold atoms in $Au_{102}(p\text{-}MBA)_{44}$ by their relative volume calculated from the estimated core diameters: $N_x = 102 \times (1.6$ nm $/ 1.2$ nm$)^3 \approx 240$.

UV-vis spectrum (see Fig. 3) shows a weak LSPR band at 530 ± 15 nm. Recent studies have shown that LSPR begins to appear when MPC has approximately 200 gold atoms and becomes
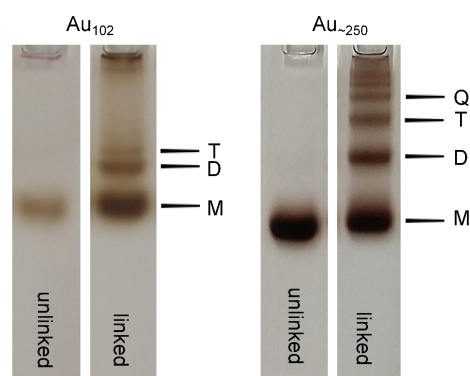
stronger as the cluster size increases. Our spectrum is comparable to the reported spectra of 51 kDa[26], 45 kDa and 53 kDa clusters[27], with estimated number of gold atoms 250, 226, and 253, respectively. We label our larger MPC as $Au_{\sim250}(p\text{-}MBA)_n$ based on these TEM and UV-vis estimates.

Analysis of $Au_{102}(p\text{-}MBA)_{44}$ multimers. Crude product from the $Au_{102}(p\text{-}MBA)_{44}$ ligand-exchange synthesis was analyzed with UV-vis spectroscopy after purification (see Fig. 4). The spectrum essentially reproduces the spectrum of $Au_{102}(p\text{-}MBA)_{44}$ in the visible region,[25] indicating that the cluster core remains intact in the reaction. New electronic transitions appear in the UV-region seen as spectral broadening of the ligand transitions, and the difference spectrum (see Fig. 4) reveals a new maximum in the linked clusters at 308 nm. The features closely resemble transitions of molecular BPDT measured in H_2O, but they are red-shifted. Although, optical coupling between the cores of $Au_{102}(p\text{-}MBA)_{44}$ cannot be ruled out based on these observations, it is more likely that the observed feature originates from BPDT molecules bound to gold. Similar changes in the UV-vis spectrum has been reported before for diacetylene linked 1.1 nm AuNPs.[17]

The crude synthesis product was further analyzed by PAGE, where the sample separated to several distinct bands (see Fig. 1, and ESI, Fig. S1A). We label the three lowest bands as M, D, and T bands. The most intense and most mobile M band was aligned with the $Au_{102}(p\text{-}MBA)_{44}$ reference band indicating that M band is unreacted $Au_{102}(p\text{-}MBA)_{44}$ or monomeric $Au_{102}(p\text{-}MBA)_{44-n}$ $(BPDT)_n$. This was confirmed by TEM showing dominantly monomeric MPCs for the M band (see Fig. 5a, ESI Fig. S5). The D and T bands are clearly less mobile than the M band having shorter running distance than the $Au_{102}(p\text{-}MBA)_{44}$ reference. TEM imaging of these bands shows dominantly dimers for the D band and a large fraction of trimers in T band (see Figs. 5b-c, ESI Figs. S5B-C).

TEM analysis of center-to-center distances in the D band yielded a distribution spanning from 1.8 nm up to 3.4 nm (see Fig. 5d). To gain insight into the nature of the bonding between multimers, we performed MD simulations of Au_{102}MPCs linked with one or more BPDT molecules. Atomistic models were constructed based on the known $Au_{102}(p\text{-}MBA)_{44}$

Fig. 2 PAGE bands of the $Au_{102}(p\text{-}MBA)_{44}$ and $Au_{\sim250}(p\text{-}MBA)_n$ clusters and their linked multimers. $Au_{102}(p\text{-}MBA)_{44}$ gels are from a different run than $Au_{\sim250}(p\text{-}MBA)_n$ gels, thus the run distances are not comparable. See ESI, Fig. S1A for samples in a same PAGE run.
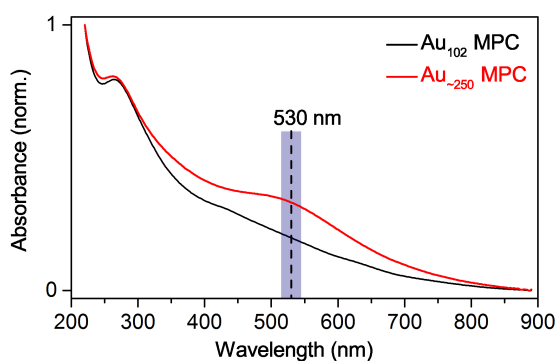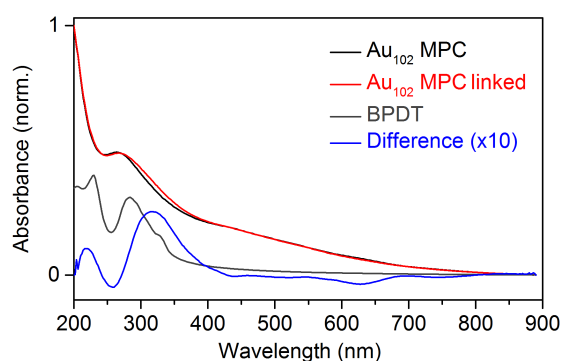

Fig. 3 Normalized UV-vis spectra of $Au_{102}(p\text{-}MBA)_{44}$ (black) and $Au_{\sim250}(p\text{-}MBA)_n$ (red) clusters in H_2O. LSPR absorption maximum of $Au_{\sim250}(p\text{-}MBA)_n$ at 530 ± 15 nm is indicated with a dashed line.

Fig. 4 Normalized UV-vis spectra of $Au_{102}(p\text{-}MBA)_{44}$ before (black) and after (red) linking with BPDT in H_2O, arbitrarily scaled spectrum of molecular BPDT in H_2O (grey), and difference spectrum of spectra before and after linking (linked Au_{102} MPC - unlinked Au_{102} MPC, blue, scaled by factor 10).
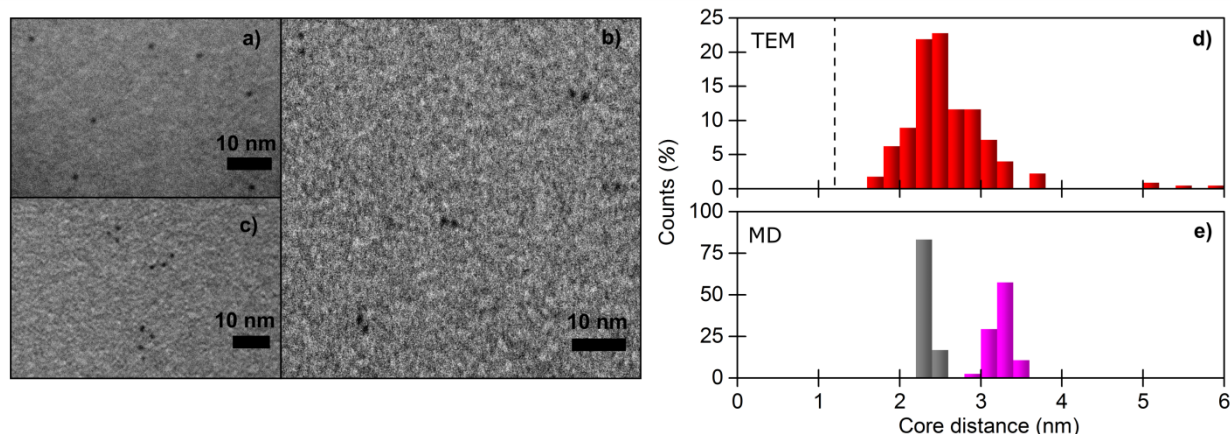
ARTICLE

Fig. 5 TEM images of a) monomeric, b) dimeric, and c) trimeric Au$_{102}$MPCs in M, D, and T bands, respectively. Distribution of center-to-center distances of the linked Au$_{102}$MPC dimers d) from TEM images (number of particles, n = 220), and e) from simulation of fully-protonated (grey) and fully-deprotonated (purple) Au$_{102}$MPC − (BPDT)$_2$ − Au$_{102}$MPC in H$_2$O. The estimated core size of 1.2 nm is marked with a dashed vertical line.

X-ray structure[20] as described in Materials and Methods. The simulations were done in water both for the fully protonated and deprotonated forms of p-MBA ligand surface.

Simulations of the Au$_{102}$(p-MBA)$_{43}$-BPDT-Au$_{102}$(p-MBA)$_{43}$ dimer indicated that the linkage by a single BPDT is rather rigid and both sterically and electrostatically demanding. The deprotonated system was not stable unless electrostatic repulsion was screened by adding a significant amount of salt. The simulation in saline solution produced a very narrow center-to-center distance distribution between 2.5 − 2.7 nm (see Fig. S6A) that is unable to reproduce the full range of experimentally observed distances.

Simulations of Au$_{102}$(p-MBA)$_{43}$−(BPDT)$_2$−Au$_{102}$(p-MBA)$_{43}$ dimer with a disulfide bridge between the BPDT molecules indicated a stable and flexible system (see Fig. 6). The center-to-center distances started from 2.2 nm for the fully protonated system

Fig. 6 Snapshot from MD simulation of a) fully protonated and b) fully deprotonated Au$_{102}$MPC − (BPDT)$_2$ − Au$_{102}$MPC in H$_2$O. Orange: Au; yellow: S; cyan, C; red: O. The disulfide bridge is highlighted by a yellow bond at the center.

and extended up to 3.6 nm for the fully deprotonated systems, agreeing with the tails of the experimental distribution (see Fig. 5c). The simulated distributions of fully protonated and deprotonated clusters are relatively narrow and peak at the ends of the experimental spectrum. This suggests that Au$_{102}$MPCs are neither fully protonated nor fully deprotonated forming a distribution of distances based on the protonation level. Distances below 2.2 nm in the experimental distribution can be addressed to the roughness of the TEM support film leading to tilted dimers with respect to the imaging plane.

Simulations of dimers, where three BPDT molecules connect fully deprotonated MPCs, yield a distribution which spans from 3.5 nm to 4.5 nm being above experimentally observed values (see ESI, Fig. S6E). Although, this does not exclude possibility of triple linker, it suggests that triple linking is rare. Dimers linked with multiple BPDT bridges are very unlikely due to low BPDT concentration used in the experiment (only two BPDT per 44 p-MBA). Therefore, the most straightforward explanation is that Au$_{102}$MPC dimers are linked primarily by two BPDT molecules with a single disulfide bridge between them.

Analysis of Au$_{\sim250}$(p-MBA)$_n$ multimers. We did a similar PAGE analysis and separation for the crude product of Au$_{\sim250}$(p-MBA)$_n$ ligand exchange reaction as for Au$_{102}$(p-MBA)$_{44}$. PAGE showed several distinct bands, however, the bands were less mobile than linked Au$_{102}$MPCs by a factor comparable to the mobility difference between unlinked MPCs (see Fig. 2, ESI Fig. S1). TEM imaging of the three lowest bands, M, D, and T, revealed dominantly monomeric, dimeric, and trimeric structures of Au$_{\sim250}$(p-MBA)$_n$, respectively (see Fig. 7a-d and ESI, Figs. S7-9). The distributions of multimer core counts in M, D, and T bands in Fig. 7d were obtained from a concentrated sample prepared for UV-vis spectroscopy. The purity of the samples can be further increased by using less concentrated material in PAGE (see ESI, Figure S10).

Note that the D and T bands are very narrow, as in the case of Au$_{102}$(p-MBA)$_{44}$. This provides additional evidence that the Au$_{\sim250}$(p-MBA)$_n$ is a monodisperse MPC.

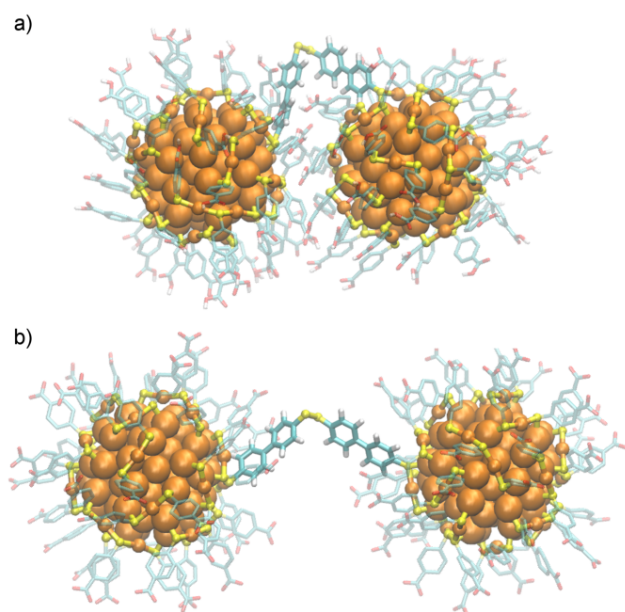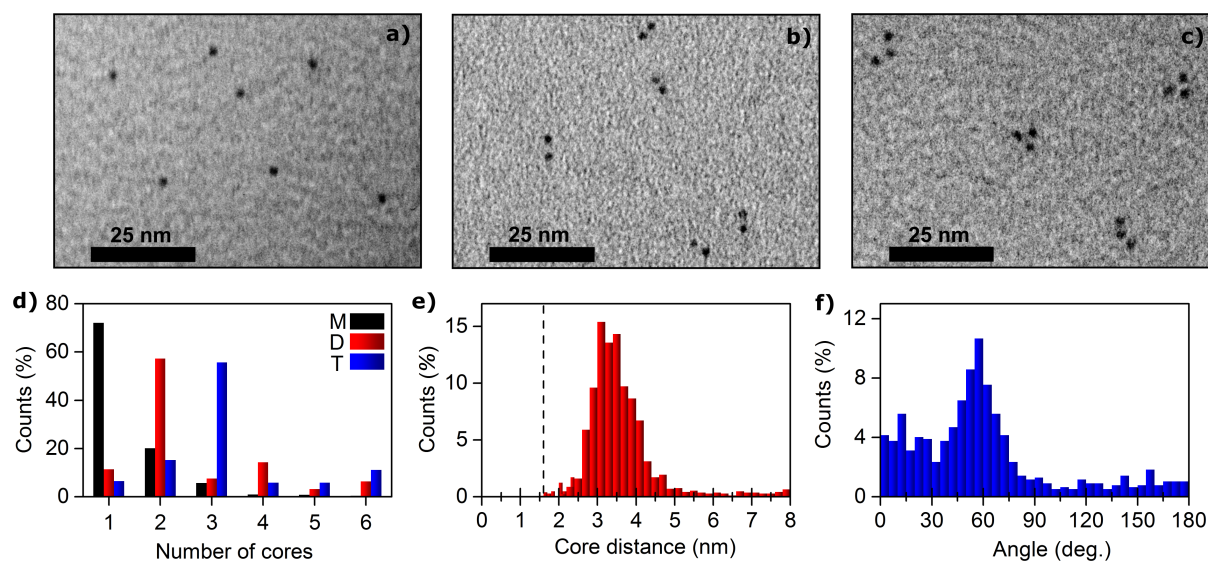**Fig. 7** TEM images of a) monomeric, b) dimeric, and c) trimeric Au$_{\sim250}$MPCs. e) Statistics of multimers from M (number of particles, n = 1119), D (n = 227), and T (n = 624) bands of linked Au$_{\sim250}$MPCs. Distribution of e) center-to-center distances for dimers (n = 1863), and f) angles for trimers (n = 770) analyzed from TEM images of linked Au$_{\sim250}$MPCs. The estimated core size of 1.6 nm is marked with a dashed vertical line.

TEM analysis of center-to-center distances in the D band of Au$_{\sim250}$MPCs was rather broad spanning from 2.6 nm up to 4.4 nm (see Fig 7e). The larger diameter of Au$_{\sim250}$(*p*-MBA)$_n$ adds a constant shift of 0.4 nm to the Au$_{102}$(*p*-MBA)$_{44}$ distribution. The tail of the distribution extending up to 4.4 nm can be explained by contribution from dimers bound by three (or more) BPDT molecules. The larger electrostatic repulsion between Au$_{\sim250}$MPCs compared to Au$_{102}$MPCs might favor longer linkers. Remarkably, the distribution of the angles in the TEM analysis of trimers showed a dominant peak at 60° indicating equilateral triangular multimers (see Fig. 7f), which is also clearly visible in the micrographs in addition to bent or linear geometries (see Fig. 7c, and ESI Fig. S9). The preference for equilateral triangles could be explained by a covalent bridge between each pair of MPCs in a trimer (see Fig. 1, and ESI, Fig S11).

Plasmon coupling in Au$_{\sim250}$(*p*-MBA)$_n$ multimers. To study optical properties of the plasmonic Au$_{\sim250}$(*p*-MBA)$_n$, we ran PAGE multiple times to prepare concentrated samples from M, D, and T bands. UV-vis absorption spectrum from the concentrated M band was equal to unlinked Au$_{\sim250}$(*p*-MBA)$_n$ in the visible region, but it showed changes in the UV region as in the case of Au$_{102}$MPCs. Comparison of spectra from M, D, and T bands, normalized to the main LSPR peak at 530 nm, (see Fig. 8a, and ESI, Figure S12) shows interesting new features for the linked Au$_{\sim250}$MPCs in the visible region. The difference between normalized spectra of D and M bands (Fig. 8b) has two broad and significantly red-shifted peaks. These features become stronger in the difference spectrum between T and M bands. If we fit two Gaussian functions with an exponential background to the difference spectra, the fit reproduces these features extremely well in both cases. The obtained peak positions, 630 nm and 810 nm, are the same for the D and T bands. The features are weak compared to the main LSPR

band, but they are locally significant altering absorption intensity up to ~10%. More importantly, they are reproducible (see ESI, Figure S13).

It is difficult to ascertain the origin of these modes experimentally. We observed, however, significant red-shift of the main LSPR peak when *unlinked* Au$_{\sim250}$MPCs were agglomerated by reducing pH down to 3.5 (see ESI, Fig S14). This is typical plasmonic nanoparticle behavior which originates from the coupling of LSPR modes between nearby NPs.[3] The observed feature peaks at 635 nm in the difference
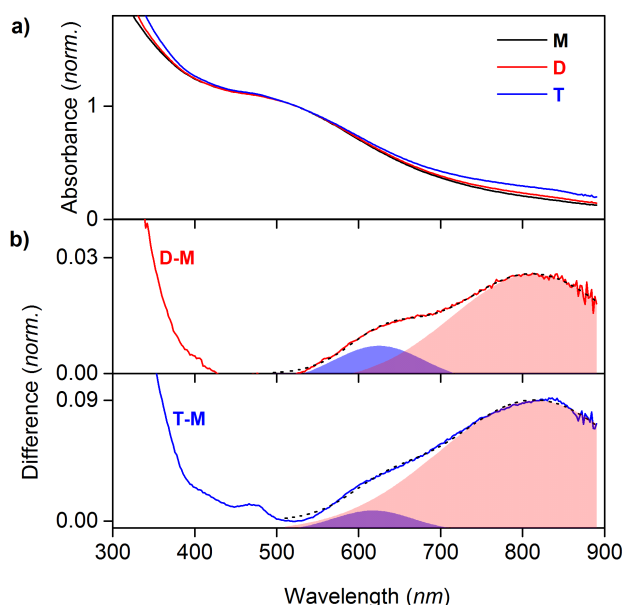

Fig. 8 a) Normalized UV-vis spectra of purified samples from M, D, and T bands. b) Difference spectra between samples from D and M bands (top) as well as from T and M bands (bottom). The shaded areas indicate Gaussian components found in the data and the dashed curves indicate the totals.

spectrum between low and high pH (see ESI, Fig S14). This strongly suggests that the peak at 630 nm in the spectra of Au$_{\sim250}$MPC dimers and trimers originates from a coupled plasmon mode, called bonding dipolar plasmon (BDP) mode, where LSPRs of two nearby particles oscillate in-phase.[3] Therefore, this feature would not be directly related to the linker molecule, but only to the fact that two plasmonic particles are close to each other.

Using parameters relevant to our system (particle diameter 1.6 nm and edge-to-edge distance 1.4 nm), the well-known "plasmon ruler equation"[43] predicts a minor plasmon shift (< 10 nm) as compared to the observed shift of 100 nm from 530 nm to 630 nm. The failure of the plasmon ruler equation here could be due to its incompatibility to sub-2 nm MPCs for which atomistic details play an important role. The thickness of the ligand layer is comparable to the diameter of the metal core, and therefore, hybridization of the metallic core with the pi-electrons of the ligand layer might have significantly larger influence than in larger NPs.

We did not observe the peak at 810 nm in unlinked Au$_{\sim250}$MPC agglomerates, and it is sensitive to the number of cores in the multimer. Therefore, we assign this mode to quantum-mechanical effects depending on the electronic structure of the molecular bridge. Previous studies of linked NPs have shown that a tunneling charge transfer plasmon (tCTP) can

form between NPs when they are connected with a molecular linker or similar structure.[44-48] This mode typically exists together with the BDP mode, it is red-shifted with respect to the BDP mode, and it depends sensitively on the tunneling properties of the NP − molecule − NP junction. Moreover, tunneling through molecular states allows coupling over much longer distances than the normal charge transfer plasmon (CTP), that happens only over very short (< 1 nm) insulating gaps and causes blue-shift instead of red-shift[44,49,50]

Simulations of a simple two-level system between plasmonic NPs have showed that tCTP mode forms when a molecular state localized on the linker is near the Fermi level of the combined system.[47] To examine whether such localized states could exists in Au$_{\sim250}$MPC multimers, we performed DFT simulations on a model system. While we do not have currently information of the atomic structure of Au$_{\sim250}$MPC, we have previously done density functional theory (DFT) calculations on a slightly larger plasmonic Au$_{314}$(SH)$_{96}$ model MPC.[40] We now built a model system (see Fig. 9) by linking two such clusters via a disulfide-bridged BPDT pair and solved for its electronic structure using DFT. Several molecular states that are localized on BPDT were found starting 0.8 eV below (occupied states) and 1.7 eV above (unoccupied states) the Fermi level (see Fig. 9). These states are close enough to the Fermi level, that when coupled to LSPRs of MPCs in an optical
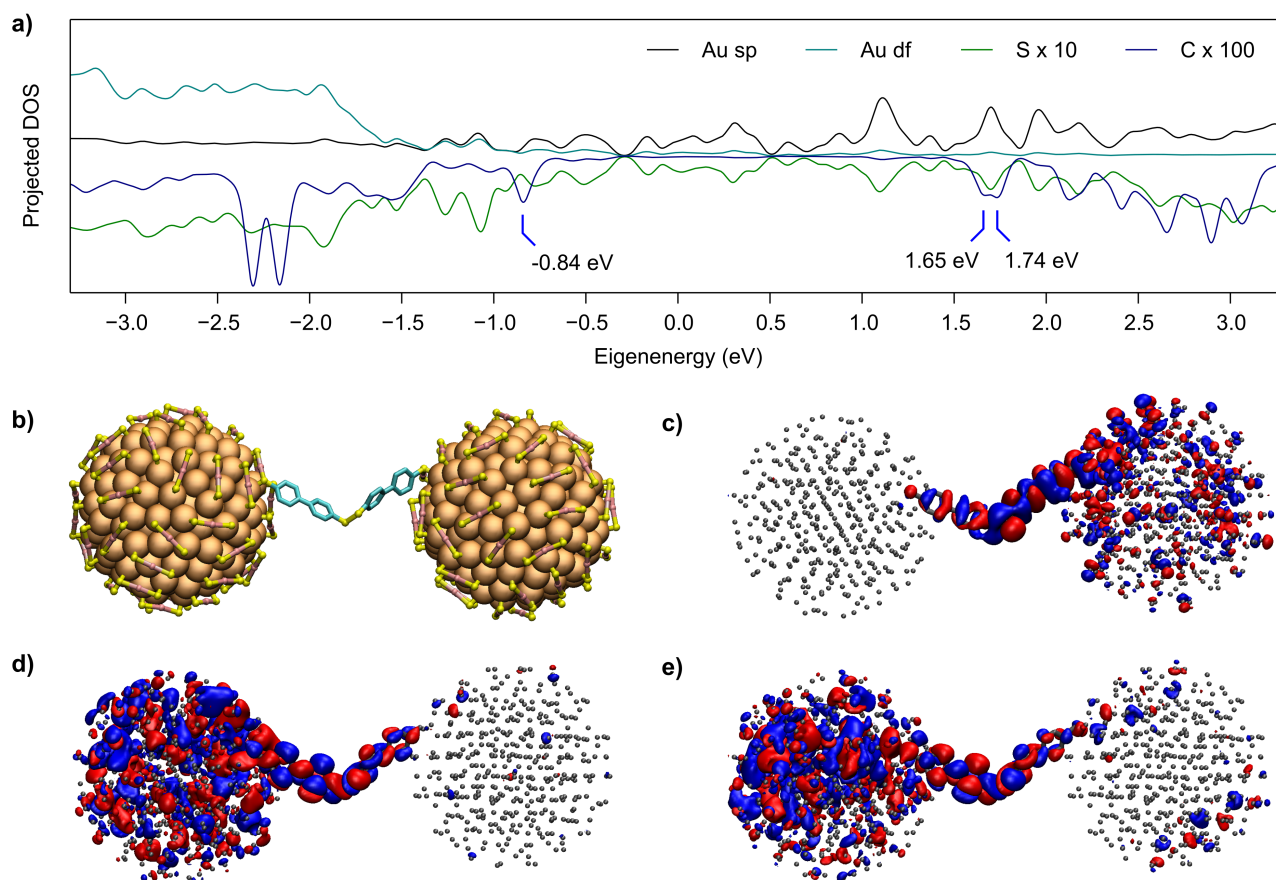
Fig. 9 a) Projected density of states for Au$_{314}$(SH)$_{95}$−BPDT−BPDT−Au$_{314}$(SH)$_{95}$ calculated using DFT. Projection to sulfur (green) is scaled by 10 and projection to carbon (blue) is scaled by 100 with respect to projection to s/p (black) and d/f (cyan) orbitals of gold. b) Geometry of Au$_{314}$(SH)$_{95}$−BPDT−BPDT−Au$_{314}$(SH)$_{95}$ dimer used in the calculation. Hydrogens are omitted for clarity. Isosurfaces for orbitals corresponding eigenenergies of c) -0.84 eV, d) 1.65 eV, and e) 1.74 eV with respect to the Fermi level.

excitation, they could act as tunneling channels for the tCTP mode, and therefore, account for the observed absorption in 700 - 900 nm range and possibly longer wavelengths.

Another possible explanation for the observed 810 nm peak is that the incoming BPDT ligand would alter the electronic structure of $Au_{\sim 250}(p\text{-MBA})_n$ and thus introduce new transitions near 800 nm. This is highly unlikely as the 810nm mode does not appear in the spectrum of $Au_{\sim 250}MPC$ monomer or linked $Au_{102}MPCs$. Another BDP mode as the origin of 810 nm peak is also not plausible, because larger spectral red-shift would require shorter interparticle distance, which is not possible based on our MD simulations. All observations are in agreement with our proposed interpretation that the 810 nm peak originates from a tCTP or similar mode, nevertheless, further theoretical and experimental studies are needed to uncover the details of the plasmonic coupling in the linked $Au_{\sim 250}MPC$ multimers.

Conclusions

We have achieved covalent linking between two gold nanoparticles which have a precisely known atomic structure, $Au_{102}(p\text{-MBA})_{44}$. In our approach, a BPDT molecule replaces a p-MBA ligand molecule in a ligand exchange reaction and becomes a part of the protecting ligand layer. The covalent disulfide bridge between two BPDT ligands joins the ligand layers and metal cores of two clusters forming a single unit with a well-defined atomic structure comparable to a molecule. This is an important step towards synthesis of atomically-precise MPC superstructures. Our approach differs from the previous studies, where linking has been noncovalent or atomic-level structure of the particle was unknown.

Moreover, we synthesized a larger, plasmonic monodisperse MPC, $Au_{\sim 250}(p\text{-MBA})_n$, and its multimers. Changes in the UV-vis spectra of $Au_{\sim 250}MPC$ multimer indicated two hybridized LSPR modes with much larger red-shifts than expected from experiments of colloidal NPs. We assigned the first mode as the typical BDP mode in plasmonic NP aggregates. The second mode, however, is likely to originate from a tCTP, where tunneling happens through molecular states of disulfide bridged BPDT molecules. $Au_{\sim 250}MPC$ multimers are the smallest systems reported which are essentially monodisperse, and show plasmonic coupling over a single covalently bound molecular bridge. Therefore, these systems are ideal candidates for connecting experimental observations to ab-initio level theory in the field of nanoplasmonics.

Acknowledgements

Notes and references

1   U. Kreibig and M. Vollmer, Optical Properties of Metal Clusters, Springer-Verlag, Berlin Heidelberg, 1995.
2   C. Bréchignac, P. Houdy and M. Lahmani, Nanomaterials and Nanochemistry, Springer-Verlag Berlin Heidelberg, 2010.
3   N.J. Halas, S. Lal, W.S. Chang, S. Link and P. Nordlander, Chem. Rev., 2011, 111, 3913-3961.
4   C. Sönnichsen, B.M. Reinhard, J. Liphardt and A. P. Alivisatos, Nature Biotechnology, 2005, 23, 741-745.
5   B. M. Reinhard, M. Siu, H. Agarwal, A. P. Alivisatos and J. Liphardt, NanoLetters, 2005, 5, 2246-2252.
6   E. C. Le Ru and P. G. Etchegoin, Annu. Rev. Phys. Chem., 2012, 63, 65–87.
7   S. Yampolsky, D. A. Fishman, S Dey, E. Hulkko, M. Banik, E. O. Potma and V. A. Apkarian, Nature Photonics, 2014, 8, 650-656.
8   M. Quinten, U. Kreibig, D. Schönauer and L. Genzel, Surf. Sci., 1985, 156, 741-750.
9   X. Wang, G. Li, T. Chen, M. Yang, Z. Zhang, T. Wu and H. Chen, Nano Lett., 2008, 8, 2643-2647.
10 S.L. Kleinman, B. Sharma, M.G. Blaber, A.-I. Henry, N. Valley, R.G. Freeman, M.J. Natan, G.C. Schatz and R.P. Van Duyne, J. Am. Chem. Soc., 2013, 135, 301-308.
11 A. Cunningham, S. Mühlig, C. Rockstuhl and T. Bürgi, J. Phys. Chem. C, 2011, 115, 8955–8960.
12 C.L. Haynes and R.P. Van Duyne, J. Phys. Chem. B,, 2001, 105, 5599–5611.
13 S.J. Tan, M.J. Campolongo, D. Luo and W. Cheng, Nature Nanotechnol., 2011, 6, 268-76.
14 G.A. DeVries, M. Brunnbauer, Y. Hu, A.M. Jackson, B. Long, B.T. Neltner, O. Uzun, B.H. Wunsch and F. Stellacci, Science, 2007, 315, 358-361.
15 R. Sardar, T. Heap and J. S. Shumaker-Parry, J. Am. Chem. Soc., 2007, 129, 5356-5357.
16 H. Cha, J.H. Yoon and S. Yoon, ACS Nano, 2014, 8, 8554-8563.
17 T. Peterle, P. Ringler and M. Mayor, Adv. Funct. Mater., 2009, 19, 3497-3506.
18 D-H. Tsai, T. J. Cho, F. W. DelRio, J. M. Gorham, J. Zheng, J. Tan, M. R. Zachariah and V. A. Hackley, Langmuir, 2014, 30, 3397-3405.
19 T. Tsukuda, Häkkinen Häkkine and Protected H., Metal Clusters: From Fundamentals to Appliations, Elsevier, Amsterdam, 2015..
20 P.D. Jadzinsky, G. Calero, C.J. Ackerson, D.A. Bushnell and R.D. Kornberg, Science, 2007, 318, 430-433.
21 M. Walter, J. Akola, O. Lopez-Acevedo, P. D. Jadzinsky, G. Calero, C. J. Ackerson, R. L. Whetten, H. Grönbeck and H. Häkkinen, Proc. Natl. Acad. Sci., 2008, 105, 9157-9162.
22 C. L. Heinecke, T. W. Ni, S. Malola, V. Mäkinen, O. A. Wong, H. Häkkinen and C. J. Ackerson, J. Am. Chem. Soc., 2012, 134, 13316-13322.
23 S. Knoppe, A.C. Dharmaratne, E. Schreiner, A. Dass and T. Bürgi, J. Am. Chem. Soc., 2010, 132, 16783–16789.
24 S. Mustalahti, P. Myllyperkiö, S. Malola, T. Lahtinen, K. Salorinne, J. Koivisto, H. Häkkinen and M. Pettersson, ACSNano, 2015, 9, 2328–2335.
25 E. Hulkko, O. Lopez-Acevedo, J. Koivisto, Y. Levi-Kalisman, R.D. Kornberg, M. Pettersson and H. Häkkinen, J. Am. Chem. Soc., 2011, 133, 3752-3755.
26 C. Yi, H. Zheng, L. M. Tvedte, C. J. Ackerson and K. L. J. Knappenberger Jr., Phys. Chem. C, 2015, 119, 6307-6313.

27 Y. Negishi, T. Nakazaki, S. Malola, S. Takano, Y. Niihori, W. Kurashige, S. Yamazoe, T. Tsukuda and H. Häkkinen, J. Am. Chem. Soc., 2015, 137, 1206-1212.

28 V. Marjomäki, T. Lahtinen, M. Martikainen, J. Koivisto, S. Malola, K. Salorinne, M. Pettersson and H. H. Häkkinen, Proc. Nat. Acad. Sci., 2014, 111, 1277-1281.

29 W.S. Compel, O.A. Wong, X. Chen, C. Yi, R. Geiss, H. Häkkinen, K.L. Knappenberger Jr. and C.J. Ackerson, ACS Nano, 2015, 9, 11690-11698.

30 K. Salorinne, T. Lahtinen, S. Malola, J. Koivisto and H. Häkkinen, Nanoscale, 2014, 6, 7823-7826.

31 Y. Levi-Kalisman, P.D. Jadzinsky, N. Kalisman, H. Tsunoyama, T. Tsukuda, D.A. Bushnell and R.D. Kornberg, J. Am. Chem. Soc., 2011, 133, 2976-2982.

32 K. Salorinne, S. Malola, O.A. Wong, C.D. Rithner, X. Chen, C.J. Ackerson and H. Häkkinen, Nature Communications, 2016, 7, 10401.

33 M. Azubel, J. Koivisto, S. Malola, D. Bushnell, G. L. Hura, A. H. Koh, H. Tsunoyama, T. Tsukuda, M. Pettersson, H. Häkkinen and R. D. Kornberg, Science, 2014, 345, 909-912.

34 B. Hess, C. Kutzner, D. van der Spoel and E. Lindahl, J. Chem. Theory Comput., 2008, 4, 435-447.

35 E. Pohjolainen, X. Chen, S. Malola, G. Groenhof and H. Häkkinen, J. Chem. Theory Comp., 2016, 12, 1342–1350.

36 M. D. Case, T. A. Darden, T. E., III Cheatham, C. L. Simmerling, J. Wang, R. E. Duke, R. Luo, R. C. Walker, W. Zhang, K. M. Merz, B. Roberts, S. Hayik, A. Roitberg, G. Seabra, J. Swails, A. W. Götz, I. Kolossváry, K. F. Wong, F. Paesani, J. Vanicek, R. M. Wolf, J. Liu, X. Wu, S. R. Brozell, T. Steinbrecher, H. Gohlke, Q. Cai, X. Ye, J. Wang, M. -J. Hsieh, G. Cui, D. R. Roe, D. H. Mathews, M. G. Seetin, R. Salomon-Ferrer, C. Sagui, V. Babin, T. Luchko, S. Gusarov, A. Kovalenko and P. A. Kollman, AMBER 12, University of California: San Fransisco, 2012..

37 M. Frisch, G. W. Trucks, H. B. Schlegel, G. E. Scuseria, M. A. Robb, J. R. Cheeseman, G. Scalmani, V. Barone, B. Mennucci, G. A. Petersson, H. Nakatsuji, M. Caricato, X. Li, H. P. Hratchian, A. F. Izmaylov, J. Bloino, G. Zheng, J. L. Sonnenberg, M. Hada, M. Ehara, K. Toyota, R. Fukuda, J. Hasegawa, M. Ishida, T. Nakajima, Y. Honda, O. Kitao, H. Nakai, T. Vreven, J. A., Jr. Montgomery, J. E. Peralta, F. Ogliaro, M. Bearpark, J. J. Heyd, E. Brothers, K. N. Kudin, V. N. Staroverov, R. Kobayashi, J. Normand, K. Raghavachari, A. Rendell, J. C. Burant, S. S. Iyengar, J. Tomasi, M. Cossi, N. Rega, J. M. Millam, M. Klene, J. E. Knox, J. B. Cross, V. Bakken, C. Adamo, J. Jaramillo, R. Gomperts, R. E. Stratmann, O. Yazyev, A. J. Austin, R. Cammi, C. Pomelli, J. W. Ochterski, R. L. Martin, K. Morokuma, V. G. Zakrzewski, G. A. Voth, P. Salvador, J. J. Dannenberg, S. Dapprich, A. D. Daniels, Ö. Farkas, J. B. Foresman, J. V. Ortiz, J. Cioslowski and D. J. Fox, Gaussian 09, Revision D.01, Gaussian Inc.: Wallingford CT, 2009..

38 C. I. Bayly, P. Cieplak, W. Cornell and P. A. Kollman, J. Phys. Chem., 1993, 97, 10269-10280.

39 J. Enkovaara, R. Rostgaard, J. J. Mortensen, J. Chen, M. Dulak, L. Ferrighi, J. Gavnholt, C. Glinsvad, V. Haikola, H. A. Hansen, H. H. Kristoffersen, M. Kuisma, A. H. Larsen, L. Lehtovaara, M. Ljungberg, O. Lopez-Acevedo, P. G. Moses, J. Ojanen, T. Olsen, V. Petzold, N. A. Romero, J. Stausholm, M. Strange, G. A. Tritsaris, M. Vanin, M. Walter, B. Hammer, H. Häkkinen, G. K. H. Madsen, R. M. Nieminen, J. K. Nørskov, M. Puska, T. T. Rantala, J. Schiøtz, K. S. Thygesen and K. W. Jacobsen, J. Phys.: Condens. Matter, 2010, 22, 253202.

40 S. Malola, L. Lehtovaara, J. Enkovaara and H. Häkkinen, ACS Nano, 2013, 7, 10263-10270.

41 G. Plascencia-Villa, B. Demeler, R. L. Whetten, W. P. Griffith, M. Alvarez, D. M. Black and M. Jose-Yacaman, J. Phys. Chem. C, 2016, 120, 8950-8958.

42 L.M. Tvedte and C.J. Ackerson, J. Phys. Chem. A, 2014, 118, 8124-8128.

43 P.K. Jain, W. Huang and M.A. El-Sayed, Nano Letters, 2007, 7, 2080-2088.

44 W. Zhu, R. Esteban, A. G. Borisov, J. J. Baumberg, P. Nordlander, H. J. Lezec, J. Aizpurua and K. B. Crozier, Nat. Comm., 2016, 7, 11495.

45 S.F. Tan, L. Wu, J.K.W. Yang, P. Bai, M. Bosman and C.A. Nijhuis, Science, 2014, 343, 1496-1499.

46 N. Zabala, O. Pérez-González, P. Nordlander and J. Aizpurua, Proc. SPIE, 2011, 8096, 80961L.

47 V. Kulkarni and A. Manjavacas, ACS Photonics, 2015, 2, 987–992.

48 T.P. Rossi, A. Zugarramurdi, M. J. Puska and R. M. Nieminen, Phys. Rev. Lett., 2015, 115, 236804.

49 K.I. Savage, M.M. Hawkeye, R. Esteban, A.G. Borisov, J. Aizpurua and J.J. Baumberg, Nature, 2012, 491, 574-577.

50 H. Jung, H. Cha, D. Lee and S. Yoon, ACS Nano, 2015, 9, 12292-12300.

Table of Contents
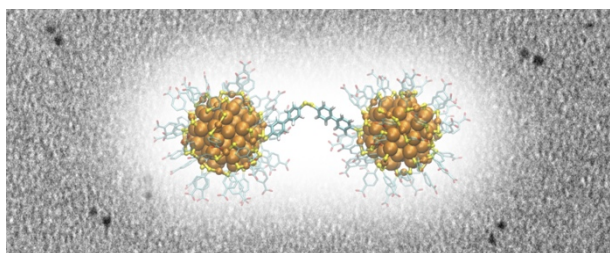
Covalently-linked multimers of monodisperse gold nanoclusters $Au_{102}(p\text{-MBA})_{44}$ and $Au_{\sim250}(p\text{-MBA})_n$ were synthesized and plasmonic coupling was observed in $Au_{\sim250}(p\text{-MBA})_n$ multimers..

II

DITHIOL-INDUCED OLIGOMERIZATION
OF THIOL-PROTECTED GOLD NANOCLUSTERS

by

Karolina Sokołowska, Eero Hulkko, Lauri Lehtovaara
and Tanja Lahtinen 2018

Journal of Physical Chemistry C, 2018, 122, 12524–12533

# Dithiol-Induced Oligomerization of Thiol-Protected Gold Nanoclusters

Karolina Sokolowska, Eero Hulkko, Lauri Lehtovaara,* and Tanja Lahtinen*

Nanoscience Center, Department of Chemistry, University of Jyväskylä, P.O. Box 35, 40014 Jyväskylä, Finland

S Supporting Information

ABSTRACT: Controlled synthesis of nanostructure oligomers requires detailed understanding of their wet chemistry and the forces driving the polymerization process. In this paper, we report the main factors affecting the reaction yields of a dithiol-induced synthesis of covalently bound nanocluster dimers and oligomers and present a detailed analysis of possible reaction mechanisms. We synthesize the nanocluster oligomers using monodisperse *para*-mercaptobenzoic acid (*p*-MBA)-protected gold nanoclusters with a nominal composition of $Au_{\sim250}(p\text{-}MBA)_n$ to minimize ensemble effects on size, shape, and surface structure. Ligand exchange was performed on the nanoclusters with five different dithiol linkers: 5,5′-bis(mercaptomethyl)-2,2′-bipyridine, 4,4″-thiobisbenzenethiol, benzene-1,4-dithiol, 1,4-benzenedimethanethiol, and dimercaptostilbene. Oligomer yields depend strongly on the used dithiol and on the dithiol-to-nanocluster ratio. Detailed analysis of the reaction yields in combination with simulations suggests that the system reaches a dynamic equilibrium, where ligand exchange happens continuously forming and breaking nanocluster oligomers that are bound together by short chains of disulfide-bridged dithiols. Despite the dynamic nature of the system, dithiol-induced polymerization of nanoclusters is a general and straightforward approach to produce dimers and larger oligomers of thiol-protected nanoclusters. Our work provides physical insight into, offers tools for, and reveals challenges in the controlled synthesis of covalently bound nanoparticle assemblies.
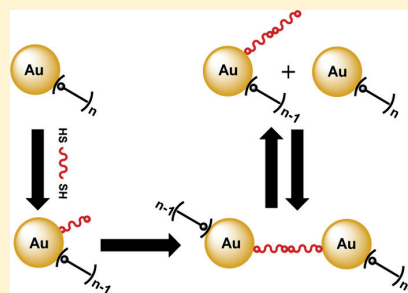
1. INTRODUCTION

Controlled assembly of metal nanoparticles to predetermined superstructures has been under extensive study during the past decades.[1] Nanoparticle assemblies can have striking optical,[2] chiro-optical,[3] and electronic effects,[4] that can be used, for example, in sensing,[5,6] photocatalysis,[7,8] and nanoelectronics.[9,10] Several approaches have been used to fabricate metal nanoparticle dimers and larger superstructures, such as, simple aggregation,[11] polymer or silica encasing,[12,13] templating polymer layers,[14] lithography,[15] and wet-chemistry linking approaches.[16−21] The wet-chemistry linking approaches to synthesize gold nanostructures have the advantage of being scalable to milligram quantities and enable better control of superstructure formation via molecular interactions. For example, DNA-linking and templating has been successfully applied to design well-defined superstructures.[9,16] Covalent cross-linking of gold nanoparticles with dithiols and multithiols is a well-known approach to form dimers and larger oligomers.[17−20] However, achieving completely homogeneous samples and control of the interparticle molecular bridges at the level of molecular precision are extremely difficult, and detailed molecular-level understanding of the linking mechanisms has not been fully achieved yet.[22] This is mainly because colloidal nanoparticles are not homogeneous but form a distribution of sizes, shapes, and surface structures.[23]

Small monolayer-protected gold nanoclusters (AuMPCs)[24,25] are monodisperse, and they have an atomically well-defined structure, which can be determined by single-crystal X-ray diffraction[26−28] or electron tomography.[29] In contrast to colloidal nanoparticles that form a continuous distribution of sizes, MPCs are known to form a discrete and relatively sparse distribution of preferred cluster sizes.[30,31] A special class of AuMPCs are thiol-protected AuMPCs, $Au_m(SR)_n$, where strong binding and covalent nature of Au–S bond make them more stable and easier to handle under ambient conditions than commonly used larger nanoparticles. Recently, several thiol-protected AuMPCs with a diameter over 2 nm have been synthesized.[30−32] Their properties are approaching the properties of colloidal nanoparticles being metallic and plasmonic while still remaining well-defined and monodisperse. Thanks to their monodispersity and well-defined atomic structure combined with stability and structure-dependent properties, large MPCs and their super-structures are excellent candidates for fundamental studies of nanoscience, for example, for studying emergence of plasmonic effects and hot-electron generation in nanoparticle dimers with unpreceded accuracy.

Several alternatives exist for forming molecular bridges between metal nanoclusters. Cross-linking of small gold clusters with organic molecules has been demonstrated using

dithiothreitol, diacetylene, chiral dithiol, diglyme, and biphenyldithiol.[20,33−36] In our previous work, where we used biphenyl-4,4′-dithiol (BPDT) to cross-link two different MPCs, namely $Au_{102}(p\text{-}MBA)_{44}$ and $Au_{\sim250}(p\text{-}MBA)_n$, we showed that dimers and trimers of monodisperse MPCs can be produced with a straightforward single-step reaction. Here, we extend this work in two ways. We show that the dithiol linking is general in the sense that it works with several different dithiols (in addition to different MPCs, as we demonstrated before[36]), and we propose a possible reaction mechanism.

In Experimental Methods section, we briefly review the synthesis that yields dithiol-linked MPC oligomers, and in addition to the commonly used standard analysis methods, we introduce a rapid method to analyze reaction yields of different oligomer fractions quantitatively. In Results and Discussion, we demonstrate that the synthesis is able to produce MPC oligomers with a variety of dithiols. Figure 1 shows the
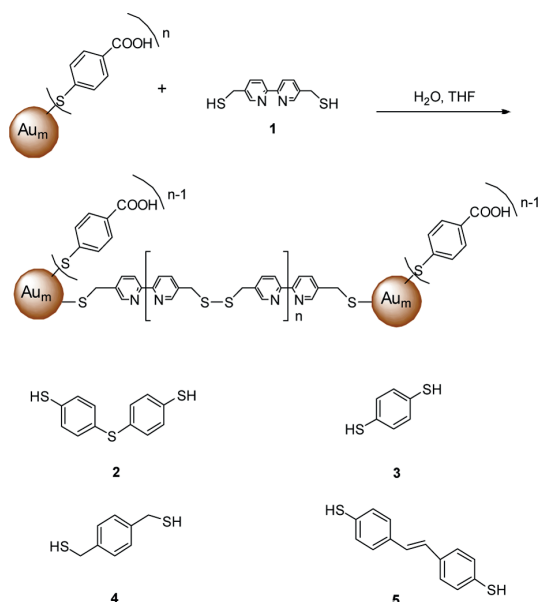

Figure 1. Suggested ligand exchange and the linking reaction of AuMPCs. The scheme also shows the molecular structure of the dithiols used to cross-link $Au_{\sim250}(p\text{-}MBA_n)$. BMM-BPy **1**, TBBT **2**, BDT **3**, BDMT **4**, and DMS **5**.

structures of the used dithiol linkers and the proposed linking mechanism of AuMPCs. We focus on 5,5′-bis-(mercaptomethyl)-2,2′-bipyridine (BMM-BPy) **1** and analyze the effects of dithiol-to-MPC ratio and reaction time to oligomer reaction yields. Finally, we discuss the possible reaction mechanisms and narrow down the options with a combination of simulations and experimental data.

2. EXPERIMENTAL METHODS

Synthesis of $Au_{\sim250}(p\text{-}MBA)_n$ nanoclusters was carried out, as described in detail in our previous publication.[36]

2.1. Synthesis of Dithiol-Linked $Au_{\sim250}(p\text{-}MBA)_n$ Nanocluster Oligomers. Dithiol cross-linked oligomers were prepared by a similar ligand-exchange synthesis previously reported for 4,4′-biphenyldithiol.[36] Briefly, stock solutions of BMM-BPy **1**, 4,4″-thiobisbenzenethiol (TBBT) **2**, benzene-1,4-dithiol (BDT) **3**, 1,4-benzenedimethanethiol (BDMT) **4**, and

dimercaptostilbene (DMS) **5** were initially prepared in tetrahydrofuran. Different dithiol solutions (**1**−**5**) were added to a $Au_{\sim250}(p\text{-}MBA)_n$ water solution with a resulting 2:1 molar ratio (dithiol/MPC). The concentration of $Au_{\sim250}(p\text{-}MBA)_n$ was calculated from the estimated molecular weight of 65 kDa (~250 gold atoms and ~100 thiolates). The ligand-exchange reaction was quenched after 3.5 h by adding isopropanol and 5 M NH_4OAc to the reaction mixture. The resulting black precipitate was centrifuged, and the supernatant containing any remaining free thiol residue was removed. The pellet containing the reaction products was dissolved to H_2O. The linking reaction was carried out for BMM-BPy **1** also with dithiol-to-MPC ratios of 1:5, 1:2, 1:1, 2:1, and 10:1. Notable difference to our previously reported synthesis is the omission of adding concentrated NaOH in the dithiol/MPC reaction mixture. We have discovered that the linking occurs efficiently also without addition of a base.

2.2. Polyacrylamide Gel Electrophoresis. Polyacrylamide gel electrophoresis (PAGE) was used to separate reaction products of $Au_{\sim250}(p\text{-}MBA)_n$ oligomer syntheses with different dithiols. Electrophoretic separation was performed using a Bio-Rad Mini-Protean Tetra System apparatus operated at 130 V. Polyacrylamide gels (15 w/v %, 29:1 acrylamide/bisacrylamide) with 1.0 mm thickness were used in the separation. Run buffer in the experiments was 2× Tris/borate/EDTA.

2.3. UV−Vis Spectroscopy. Optical absorption measurements were carried out with PerkinElmer Lambda 850 UV−vis spectrometer with 2 nm resolution. To measure UV−vis absorption directly from the PAGE gels, each electrophoretically separated column was mechanically cut from the gel and compressed between two quartz microscopy slides. Light beam was accurately positioned on individual gel bands by locally maximizing the absorption using an XYZ-micrometer stage positioned inside the spectrometer.

2.4. Transmission Electron Microscopy. Transmission electron microscopy (TEM) samples were prepared by dropcasting 8 μL of dilute deionized water solution of linked nanoclusters on a glow discharged 400 mesh holey carbon copper grid (Ted-Pella ultrathin c). Solution was allowed to deposit for 15 min, after which excess sample was removed, and the grid was allowed to dry under vacuum overnight. Samples were imaged with JEOL JEM-1400HC TEM operated at 80 kV, equipped with bottom mounted 11 Megapixel CCD camera (Olympus SIS Quemesa).

2.5. Analysis of Reaction Yields with a Desktop Scanner. We developed a method where a standard desktop scanner is used to evaluate rapidly reaction yields of nanocluster oligomers. First, a desktop scanner (Canon imageRUNNER) was calibrated against a set of neutral density filters, in the following way. Each of the neutral density filters was measured with a UV−vis spectrometer to obtain its absorbance. Then, the same set of filters was scanned with a white A4 paper as a background. The grayscale values obtained from the scanned image were plotted against absorbance of each filter at 500 nm (see Figure S1). The data were fitted to obtain a conversion curve from grayscale values to the corresponding absorbance values.

The calibration was followed by the actual analysis. First, a normal PAGE run was performed. Then, the wet PAGE gel—still between the glass plates—was immediately scanned. The same white A4 paper that was used in the calibration was used again as the background. The scanned image was converted to a grayscale image. A narrow, rectangular area was selected around

the darkness maxima of each PAGE column, and the mean intensity of pixels in each row was calculated. The grayscale values were converted to the corresponding absorbance values using the conversion curve obtained from the calibration. The PAGE running distance was calculated by transforming the distance from pixels to millimeters by multiplying with the scanner's known resolution, dots-per-inch. This gives us integrated absorbance as a function of the PAGE running distance in millimeters. Because absorption in the visible range changes negligibly between different MPC oligomer fractions, the measured absorbance is directly proportional to the number of cluster cores in the corresponding gel position. The absorbance values can then be integrated over a band, and the integrated values can be directly converted to reaction yields, as the number of clusters per reaction product, that is, per oligomer in a PAGE band is known from TEM.

2.6. Simulations. Simulations of linking were initialized by taking 100 000 nanoclusters, represented as an array of two integers, $n_{cluster}$ and $n_{dithiol}$, where initially $n_{cluster} = 1$ and $n_{dithiol} = 0$. Then, dithiols were assigned one-by-one randomly and independently until the desired dithiol-to-MPC ratio was reached, $n_{dithiol}^{(avg)}$ = dithiol-to-MPC ratio. Next, a simple Monte-Carlo molecular kinetics was performed. At each time-step, a pair of nanoclusters, or later oligomers, was selected randomly, that is, two random array elements, $n^{(i)}$ and $n^{(j)}$, were selected. In the case of direct linking with a single dithiol, a molecular bridge was formed between nanoclusters, if at least one of the two nanoclusters had dithiol available for linking, $n_{avail}^{(i)} > 0$ or $n_{avail}^{(j)} > 0$. In the case of linking via disulfide bridge, a molecular bridge was formed between nanoclusters, if both nanoclusters had at least one dithiol available for linking, $n_{avail}^{(i)} > 0$ and $n_{avail}^{(j)} > 0$. Whether any dithiols were available for linking or not was determined by how many nanoclusters and dithiols were already in the nanocluster or oligomer. In the case of direct linking with a single dithiol, each molecular bridge reduced available dithiols for linking by one, $n_{avail} = n_{dithiol} - (n_{cluster} - 1)$. In the case of linking via disulfide bridge, each molecular bridge reduced available dithiols for linking by two, $n_{avail} = n_{dithiol} - 2(n_{cluster} - 1)$. If enough available dithiols were found, a new molecular bridge was created and the selected pair of nanoclusters/oligomers was merged as a new larger oligomer, $n^{(k)} = n^{(i)} + n^{(j)}$, and the old ones were removed, $n^{(i)} = n^{(j)} = 0$. This procedure was repeated until the distribution of oligomers converged.

Breaking of dithiol bridges, breaking via ligand exchange, formation of dithiol polymers, passivation of dithiols with p-MBA, unequal ligand-exchange probabilities, and so forth were not considered in the simulations to keep the model minimal. Addition of these effects would introduce adjustable parameters complicating the interpretation and discussion of simulation results without adding significant value.

3. RESULTS AND DISCUSSION

3.1. Qualitative Analysis of Au$_{\sim250}$(p-MBA)$_n$ Oligomers.
Crude products from the Au$_{\sim250}$(p-MBA)$_n$ ligand-exchange synthesis with different dithiols were analyzed initially by PAGE. Reaction products of all five tested dithiols (1–5) produced qualitatively similar patterns, as seen in Figure 2. In all cases, distinct bands formed above the unlinked cluster band, which means that reaction products in these bands have lower mobility than the reference unlinked cluster. Similar patterns were observed also in our previous study, where BPDT was used as the linker molecule.[36]
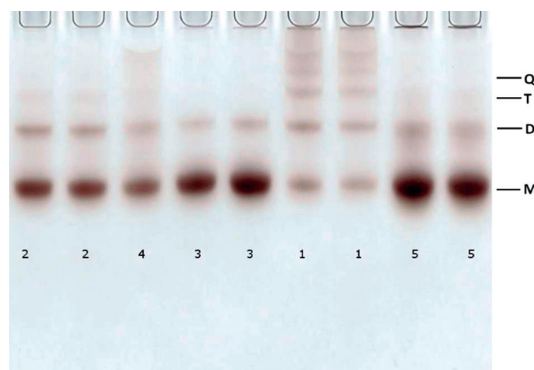

Figure 2. PAGE gel showing bands of Au$_{\sim250}$(p-MBA)$_n$ linked with different dithiols. The index of the dithiol used is specified below each column (see Figure 1). Ratio of dithiol-to-MPC was 2:1 in all cases.

We confirmed that the observed bands originate from different oligomers using TEM imaging, as shown in Figures 3
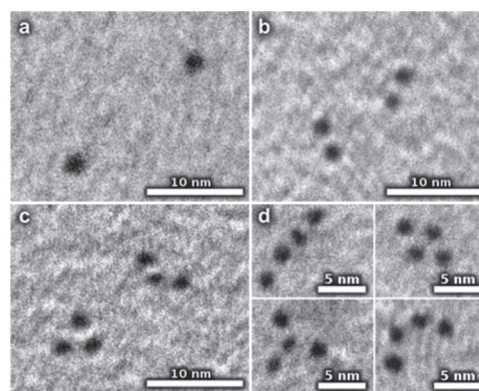

Figure 3. TEM micrographs showing (a) monomers of Au$_{\sim250}$(p-MBA)$_n$ from M band; (b) dimers linked with BMM-BPy **1** from D band; (c) trimers from T band; and (d) tetramers from Q band.

and S2–S5, for BMM-BPy **1**. The most mobile M band consists of monomers, whereas D-, T-, and Q bands contain a dominant fraction of dimeric, trimeric, and tetrameric forms, respectively. As all of the tested linking reactions with different dithiols produced PAGE patterns indicating significant presence of oligomers, the dithiol linking approach appears to be a general synthetic strategy to produce covalently bound nanocluster oligomers.

3.2. Quantitative Analysis of Au$_{\sim250}$(p-MBA)$_n$ Oligomers.
Although similar PAGE patterns are observed with all dithiols, the reaction yields of different oligomer fractions depend strongly on the particular dithiol used. To compare the relative yields between dithiols, we determined them quantitatively. We applied a rapid method inspired by the densiometric analysis of Western blot[37] and the use of PAGE to separate different MPCs.[30,38,39] The method uses a standard desktop scanner to analyze a complete PAGE gel at once. Each PAGE gel has multiple wells, each of which can be used to separate products of a different reaction. Single PAGE run followed by scanning can therefore analyze reaction yields of ten or more MPC linking reactions at once (see Experimental Methods section for the details of the method).

Normalized absorbance profiles obtained with the scanning method along each column of PAGE bands of Figure 2 are shown in Figure 4. To validate our scanning method, we
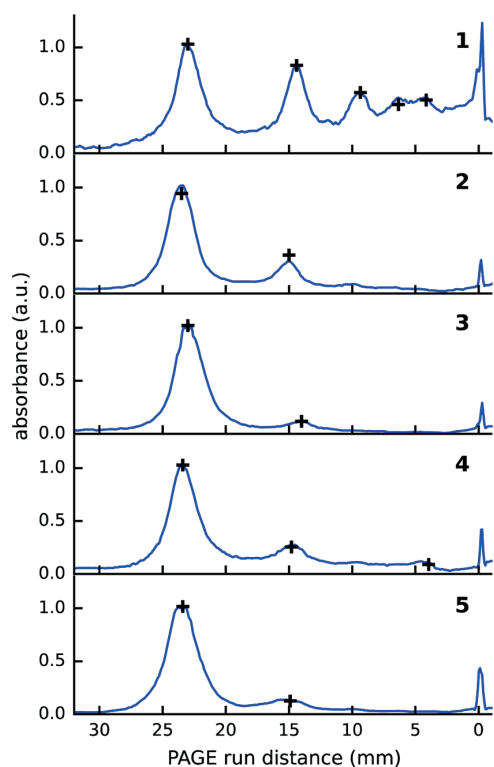

Figure 4. Absorbance of linked Au$_{\sim250}$(p-MBA)$_n$ as a function of the PAGE running distance for different dithiols. Indices of the dithiols are given in the top-right corner of each panel. The solid blue lines are the integrated absorbances obtained with the scanning method along each column of the PAGE gel. The black crosses are the integrated absorbances obtained from the UV−vis spectrum and scaled for an optimal fit to the scanning method.

performed a UV−vis spectroscopy measurement for each visible band in the same PAGE gel. The absorption spectrum (see Figure S6) was integrated from 400 to 600 nm to obtain an integrated absorbance. The integrated absorbance is directly proportional to the local concentration of nanoclusters because the UV−vis spectrum changes negligibly in this region between different oligomers. The integrated absorbance values obtained with this method are shown in Figure 4 as crosses.

The results of the scanning method for BMM-Bpy **1**, BDT **3**, BDMT **4**, and 4,4′-DMS **5** linked Au$_{\sim250}$(p-MBA)$_n$ oligomers are in near-perfect agreement with the results determined from the integrated UV−vis absorbance, as seen in Figure 4. The relative absorbance of TBBT **2** differs somewhat between the two methods, although the trend is similar. We speculate that this small discrepancy originates from experimental uncertainties in acquiring UV−vis spectra from the cut gel samples. The scanning approach is significantly faster and easier to measure than the UV−vis approach, and therefore it provides a fast and reliable way to obtain local nanocluster concentration profiles along each PAGE column for linked MPC systems.

3.2.1. Linking Efficiency. The profiles in Figure 4 show that BMM-BPy **1** is clearly the most effective in forming higher

order oligomers when the dithiol-to-MPC molar ratio was 2:1, whereas BDT **3** is the least effective. It is not surprising that BMM-BPy **1** is more efficient than BDT because BMM-BPy **1** is significantly longer than BDT **3**. Actually, BDT **3** is so short, sulfur-to-sulfur distance being 0.6 nm, that it would probably require at least three BDT **3** molecules to bridge metallic cores of two MPCs through their p-MBA ligand layers, if the thickness of the ligand layer is evaluated from the known structure of Au$_{102}$(p-MBA)$_{44}$.[28] However, the length of the dithiol linker cannot be the only factor affecting the efficiency of oligomer formation. 4,4′-DMS **5** has practically the same length (1.3 nm) as BMM-BPy **1** (1.2 nm), but its efficiency for producing dimers is an order of magnitude lower than BMM-BPy **1** and only just above the shortest linker BDT **3** (see Figure 4). This clearly indicates that also other factors than the length of the linker are important to oligomer formation. Possible candidates are, for example, steric effects and dithiol−p-MBA interactions. One would also expect that the chemical group attached to the terminal sulfurs would play an important role in the reaction. This is likely to be the case, but again, it cannot be the only determining factor. For example, BMM-BPy **1** and BDMT **4** have the same methylphenyl group attached to the sulfur but still have significantly different linking efficiencies. Therefore, the linking efficiency must be an interplay between the different factors mentioned above, and further studies are required to explain different contributions in detail. Our findings are in agreement with Salassa et al., who demonstrated that ligand distributions of Au$_{25}$(SR)$_{18-x}$(SR′)$_x$$^-$ depend on the thiol pair used for the synthesis and for the subsequent ligand exchange.[40]

3.2.2. Reaction Conditions. Next, we will focus on the most efficient linker molecule BMM-BPy **1** and analyze its reaction yields in different reaction conditions. We performed the ligand exchange of Au$_{\sim250}$(p-MBA)$_n$ with BMM-BPy **1** using different dithiol-to-MPC molar ratios of 1:5, 1:2, 1:1, 2:1, and 10:1. PAGE gel separation of the first four ratios are shown in Figure S7, and the corresponding absorption profiles are shown in Figure 5. A PAGE gel including ratio 10:1 is shown in Figure S8a. The absorption profiles show that the lowest dithiol concentration (1:5) strongly favors monomeric form yielding only a small fraction of dimers and negligible amounts of higher oligomers, as expected (see Figures S8b and S9). The trimer and larger oligomer yields increase rapidly when dithiol-to-nanocluster molar ratio is increased from 1:5 to 1:2, 1:1, and 2:1. As the concentration is increased further, the reaction begins to produce large amounts of nanocluster aggregates that remain immobile in the PAGE wells, as seen in Figure S8.

A similar trend can be observed in TEM statistics where relative abundances of different oligomers in the crude product were determined from TEM micrographs. The statistics of two different linker-to-MPC molar ratios are shown in Figure S9. The fractions of dimers, trimers, and larger oligomers are significantly higher in 2:1 molar ratio than in 1:5 ratio. PAGE and TEM distributions are not entirely comparable because some noncovalent agglomeration is prone to happen in TEM sample preparation, nevertheless, the trend is clear.

To gain more insights to the reaction mechanism, we performed quantitative analysis of reaction yields as a function of the dithiol-to-MPC ratio by processing the absorbance data produced by the scanning approach in a following way. The reaction yields were estimated from the absorbance data by integrating the area under each PAGE band. The integrated area is proportional to the number of MPCs in the band. As
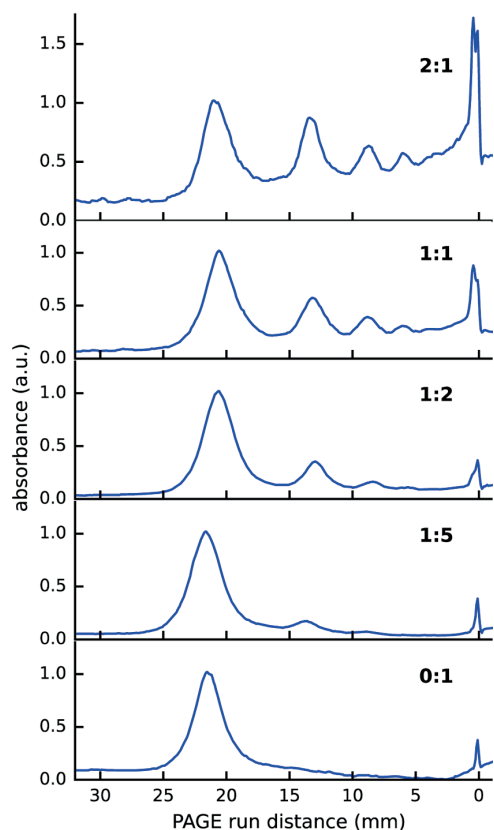
Figure 5. Absorbance of BMM-BPy **1**-linked $Au_{\sim250}(p\text{-MBA})_n$ as a function of the PAGE running distance. The molar ratios are given in the top-right corner of each panel. The lowest panel shows the unlinked $Au_{\sim250}(p\text{-MBA})_n$ reference band (ratio 0:1).

Figure 6. (a) Oligomer reaction yields normalized to the monomer yield as a function of the oligomer size for dithiol-to-MPC ratios of 1:5 (purple circles), 1:2 (cyan squares), 1:1 (blue diamonds), and 2:1 (green crosses). The reaction yields decrease approximately exponentially as the number of nanoclusters in the oligomer increases. Solid lines are linear least-squares fits to $\log_{10}(P_n/P_1)$. (b) Fit parameter p as a function of dithiol-to-MPC ratio (black crosses), fit to eq 4 with r_{AB} equal to dithiol-to-MPC ratio R, that is, one dithiol per MPC (dot-dashed green), fit to eq 4 with $r_{AB} = R/2$, that is, two dithiols per MPC (dashed blue).

each band has approximately a Gaussian profile, we fitted a set of Gaussian functions on top of a linear background (see Figure S10). The number of MPCs in a band can be converted to its relative concentration of oligomers (relative to other bands) by dividing the number of MPCs in the band by the number of MPC per oligomer known from TEM. The oligomer reaction yields as a function of dithiol-to-MPC ratio for $Au_{\sim250}(p\text{-MBA})_n$ linked with BMM-BPy **1** are shown in Figure 6a.

3.2.3. Saturation of Oligomer Yields. The reaction yields decrease approximately exponentially with respect to the number of nanoclusters in the oligomer, that is, monomer-to-dimer ratio is close to dimer-to-trimer ratio, and trimer-to-tetramer ratio. A similar behavior is observed in step-growth polymerization,[41] which has been demonstrated to happen also for nanoparticles.[42] In step-growth polymerization, bifunctional (or multifunctional) monomers form dimers with probability $(1 - p(t))p(t)$, and longer oligomers with

$$P_n = (1 - p)p^{n-1} \tag{1}$$

where P_n is probability of finding an oligomer with n monomeric units, and p is the probability for a single polymerization step. The exponential curves are shown as solid lines in Figure 6a, ratio-versus-yield-a correspond to P_n/P_1. The above equation (eq 1) holds only for ideal bifunctional monomers ($-A-$) or bifunctional polymerizing units (e.g., $-[A-B]-$) and only for the equimolar case. For a non-
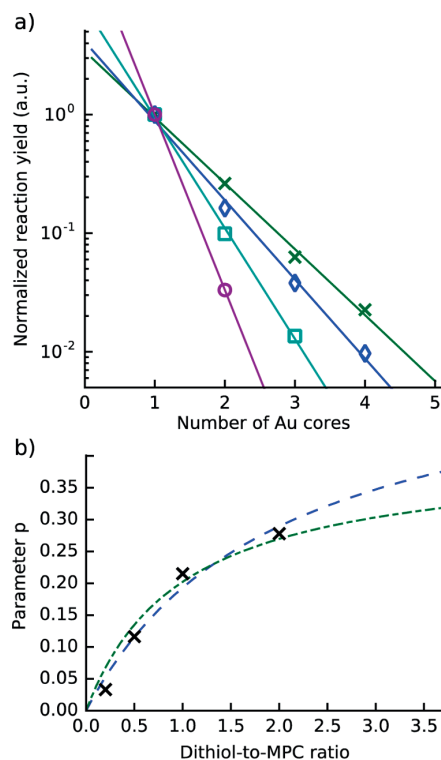
equimolar case, we can take into account the dependence on the dithiol-to-MPC ratio by replacing the degree of polymerization for the equimolar case

$$X = (1 - p_{eq})^{-1} \tag{2}$$

by the degree of polymerization for a nonequimolar case

$$X = \left(1 - p_{eq}\frac{2}{1 + r_{AB}^{-1}}\right)^{-1} \tag{3}$$

where r_{AB} is the ratio of A and B in the bifunctional unit.[41] From these equations, we see that the fit parameter p should depend on the ratio r_{AB} as

$$p(r_{AB}) = p_{eq}\frac{2}{1 + r_{AB}^{-1}} \tag{4}$$

In Figure 6b, the fit parameter p is shown as a function of the dithiol-to-MPC ratio R together with fits to eq 4 with $r_{AB} = R$ and $r_{AB} = R/2$. The first fit, $r_{AB} = R/2$, corresponds to a polymerization unit with one dithiol per MPC, that is, one dithiol directly connecting two MPCs ($-D-MPC-D-MPC-$). Whereas the second fit, $r_{AB} = R/2$, corresponds to two dithiols per MPC, that is, two dithiols connecting two

MPCs via a disulfide bridge (−D−MPC−D−D−MPC−D−). Experimental observations and both fits have the same trend, where the polymerization probability $p(R)$ changes rapidly at low dithiol-to-MPC ratios, but become saturated at higher ratios. In other words, increasing the dithiol-to-MPC ratio beyond certain point does not increase the yields of dimers, trimers, and tetramers significantly, but leads to increasing formation of large aggregates. The fits are used here only to demonstrate the trend. We will present a more rigorous analysis and an elaborate discussion below.

3.2.4. Reaction Time and Equilibrium. A typical way to control a polymerization reaction is to control its reaction time. We examined this aspect by performing syntheses using 0.25, 0.5, 3.5, and 7 h reaction times for the equimolar case (i.e., 1:1 ratio). The resulting oligomer yields are shown in Figure 7,
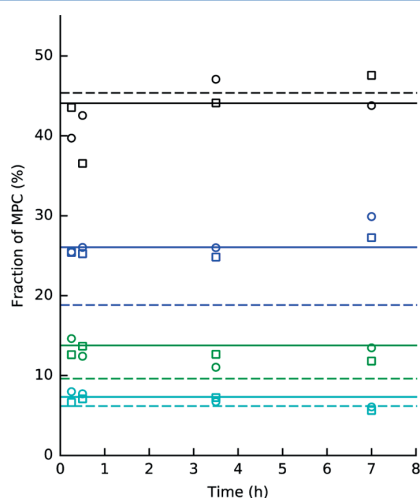

Figure 7. Oligomer yields for equimolar case (1:1) as a function of the reaction time (0.25, 0.5, 3.5, and 7 h) of two different syntheses. The shapes (circles and squares) denote different nanocluster synthesis batches. At each time, we have four values corresponding with (from top to bottom) monomer (black), dimer (blue), trimer (green), and tetramer (cyan). Simulated oligomer yields at equilibrium for ligand-exchange linking (solid) and for disulfide linking (dashed) with the optimal linking activities of 35 and 80%, correspondingly, are shown as vertical lines (for details, see discussion below). The reaction yields are given as a fraction of MPCs in the corresponding oligomeric form. The linking activity (%) is defined as the fraction of dithiols that act as molecular bridges, with respect to the total number of the dithiols.

where we observe that the reaction yields have no significant dependence on time. Therefore, the reaction must have reached its end or equilibrium, or at least, be in the slowly varying asymptotic region near the equilibrium. We will use this information in the following discussion of full kinetic model.

3.3. Kinetic Model. We have shown that our experimental results agree surprisingly well with step-growth polymerization, and it serves as a good starting point for the discussion, but it is an oversimplification of the process. In reality, the ligand-exchange process must be (at least up to a certain degree, for example, within preferred sites) a stochastic process, where ligand exchange can happen once, twice, or more times per MPC. This leads to MPCs with one, two, or more dithiol "arms", whereas some of the MPCs are left without any dithiol arms. The distribution of arms per MPC depends on the dithiol-to-MPC ratio. The ligand exchange can also happen in the

reverse direction, where an already exchanged dithiol is replaced by an exchanged *p*-MBA from the solution. In addition, we have another competing process: the disulfide bridge formation between dithiols.

Therefore, the key factors in the formation of the equilibrium (or a long-lived metastable state) in dithiol-MPC systems are (1) ligand-exchange rate, (2) disulfide formation rate, (3) ligand-exchange equilibrium between *p*-MBA and dithiol, and (4) disulfide equilibrium. Some of the rates and equilibriums might be different for free versus MPC-bound dithiols, and for monomers versus oligomers. To gain insights into this rather complex system, we will test different simplifying hypotheses and their validity. We have collected different hypotheses and their results in Figures 8 and S11.

3.3.1. Hypothesis: Fast Disulfide Formation (Figure S11x). Let us first assume that disulfide formation reaction strongly favors disulfides over thiols/thiolates. This assumption is supported by earlier research where dithiols were observed to polymerize in water-forming disulfide-bridged chains and rings.[43,44] In addition, our observation that when we add dithiol to water alone, we observe the formation of a white milky haze indicating the same polymerization process.

If we combine a hypothesis of irreversible disulfide formation with a hypothesis that this reaction is much faster than ligand exchange, we should observe long polymer chains of dithiols connecting two MPCs at the ends (see Figure S11). This would result in extremely low oligomer yields at equimolar dithiol-to-MPC ratio, however, as we observe significant amounts of oligomers, for example, in Figure 7, this combination of hypotheses is not valid.

3.3.2. Hypothesis: Fast Ligand-Exchange (Figure S11a). If we take an opposite hypothesis for the reaction speeds, that is, if ligand-exchange reaction is much faster than disulphide formation, a metastable state begins to form, where MPCs have one or more ligands exchanged to dithiols, but no molecular bridges have formed between MPCs yet (see Figures 8a and S11a). How many of the dithiols become exchanged depends on the dithiol, for example, some dithiols will have strong steric hindrance or have chemical groups that strongly repel neighboring *p*-MBAs leading to low-exchange probabilities, whereas others might be preferred over *p*-MBA for the opposite reasons. Nevertheless, in general, there exists a strong entropic force to drive dithiols from the solution to the ligand layer at equimolar dithiol-to-MPC ratio for the following reason. Initially, all dithiols are in the solution and all *p*-MBAs are in the ligand layer. Entropy drives dithiols to the ligand layer until the ligand layer and the solution have equal dithiol-to-*p*-MBA ratio (~1:100 in the equimolar case). Because the ligand layer has two orders of more thiols than in the solution, entropy drives dithiols to the ligand layer, until it has two orders of more dithiols than in the solution. In other words, unless dithiols are energetically disfavored, the metastable state has nearly all dithiols bound to MPCs.

3.3.2.1. Simplifying Assumption: Entropy Dominates. We assume, as given below, that the ligand exchange does not energetically favor or disfavor dithiol, and that the equilibrium is determined mainly by entropy. If dithiol is favored or disfavored slightly, this leads to readjustment of distribution without altering the qualitative behavior of the system.

3.3.2.2. Simplifying Assumption: Negligible Dithiol−Dithiol Interactions. As more than one dithiol per MPC must be exchanged to form trimers and larger oligomers, we must consider dithiol−dithiol interactions. We will assume that
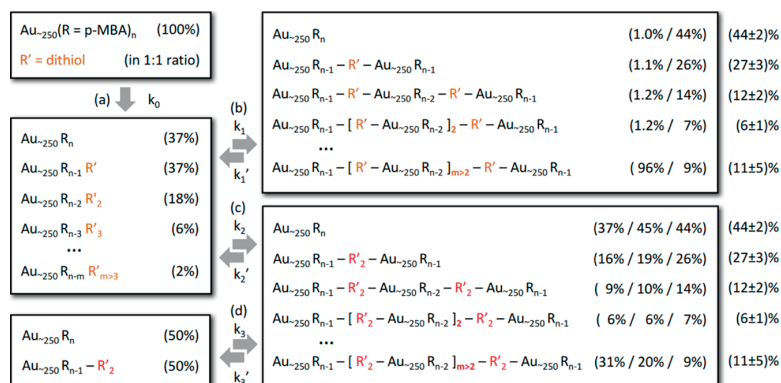
Figure 8. Schematic presentation of hypotheses and their outcomes (see also Figure S11): (a) formation of a metastable state if ligand exchange is faster than disulfide formation, (b) formation of oligomers bridged by single dithiol, (c) formation of oligomers bridged by two dithiols with a disulfide bond between them, (d) re-equilibration caused by ligand exchange after the initial formation of oligomers via disulfide bridging. Values in parenthesis are the fractions of MPCs in the specified form. Values in the top-right panel are for 100% (left) and for 35% (right) linking activity. Values in the bottom-right panel are for 100% (left) and for 80% (center) linking activity without re-equilibration, and for 70% linking activity after the re-equilibration via ligand exchange. Values in the parentheses outside of the boxes are the average of the experimental values for 3.5 h and 7 h reaction times, as shown in Figure 7. The error is calculated as the maximum absolute deviation from the average.

only a few dithiols exchange, and that the exchanged dithiols are on average far enough from each other to not interact significantly. If no significant dithiol-to-dithiol interaction exists when dithiols are bound to MPC, then the ligand-exchange process should be random and independent from how many dithiols have already been exchanged. As we are using low dithiol-to-MPC ratio, the assumption of negligible dithiol–dithiol interactions is justified.

3.2.3. Metastable State. Examples of simulated metastable states based on the above assumptions of fast, nearly one-way ligand-exchange reaction, where exchanges happen randomly and independently, are shown in Figure S12. When dithiol-to-MPC ratio is below 1:10, fraction of MPCs with one dithiol grows linearly as a function of ratio and practically no MPCs with two or more dithiols exist. Behavior diverges rapidly from linear as the ratio grows, and at equimolar ratio, only 37% of MPC have one dithiol and still 37% of MPC have no dithiol, 18% have two dithiols, 6% have three, and the remaining 2% have four or more dithiols. Above equimolar ratio, the fraction of MPCs with multiple dithiols increases rapidly, and at 4:1 ratio, it reaches 90%.

After the formation of the metastable state, molecular bridges begin to form between MPCs. This could happen in two ways. The first option is that a single dithiol forms a direct bridge from one MPC to another (see Figures 8b and S11b). The second option is that two or more dithiols form disulfide bridges that connect two MPCs (see Figures 8c and S11c). Simulations of these two cases are shown in Figure 9, where we have still assumed that both reactions are one way ($k'_1 = k'_2 = 0$).

3.3.3. Hypothesis: Direct Linking with Single Dithiol (Figure S11b). We observe that direct linking with a single dithiol would produce practically only large aggregates at equimolar ratio (see Figures 8b and S11b), which does not match with the experiment (see, e.g., Figure 7). Either direct dithiol linking does not happen or all dithiols are not active in linking. If we assume that only 35% of dithiols form dithiol bridges between MPCs, that is, the effective dithiol-to-MPC ratio is 0.35, we have an excellent match with the experimental reaction yields (see Figure 7). Here, we defined the linking activity (%) as the fraction of the dithiols that act as molecular
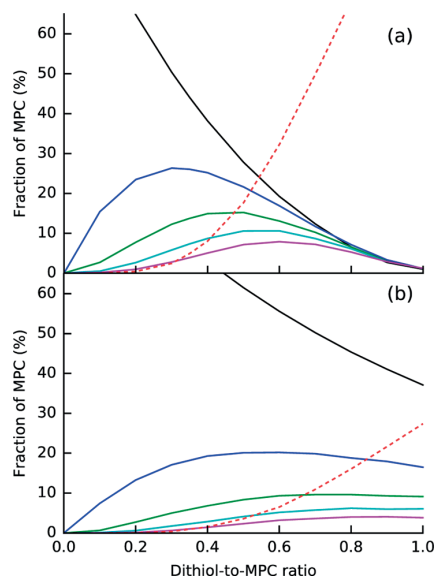
Figure 9. Simulated fractions of MPCs in the form of monomers (black), dimers (blue), trimers (green), tetramers (cyan), pentamers (magenta), and larger than pentamer (dashed red) for (a) linking where a molecular bridge between MPCs forms via ligand exchange, and for (b) linking where a bridge forms via disulfide bond formation. Panel (a) was simulated with one dithiol molecule in the bridge (minimum for a dithiol bridge), and panel (b) with one dithiol pair (minimum for a disulfide bridge).

bridges, with respect to the total number of the dithiols in the system that includes free dithiols and exchanged but non-bridging dithiols, in addition to the bridging ligands. Assuming reduced "linking activity" of 35% for dithiols is reasonable because it is possible that (1) not all dithiols become exchanged, that (2) not all exchanged dithiols form bridges, and/or that (3) exchanged p-MBAs passivate some of the dithiols.

3.3.4. Hypothesis: Indirect Linking via Disulfide Bridge (Figure S11c). Direct linking with a single dithiol and linking

activity of 35% offers a one-possible explanation, but other explanations are not yet ruled out. The second option for forming oligomers starting from the metastable state is that the exchanged dithiols form disulfide bridges between the MPCs (see Figures 8c and S11c). If we assume that this is an irreversible reaction and that ligand exchange does not happen anymore ($k_2 > 0$; k_1, k_1', k_3', k_3', $k_2' = 0$), our simulations at equimolar ratio yield a distribution of oligomers that is somewhat similar to the experimental data. The match is much better than direct linking with 100% linking activity, but it is clearly not as good as direct linking with 35% activity. Even if we take an optimal linking activity of 80% for the disulfide linking, the match is not nearly as good as the direct linking with the optimal activity of 35%, especially for dimer (see Figure 7).

The above assumption that ligand exchange does not happen after the metastable state has formed was made to simplify simulations and discussion, and it is clearly not valid in a general case. The only case when it would be valid is when dithiols are energetically strongly favored over *p*-MBAs in the ligand layer. Therefore, we consider next a more general case, where the ligand-exchange process is a continuous, two-way process that reaches a dynamic equilibrium.

3.3.5. Hypothesis: Ligand-Exchange Equilibrium Together with Slow Disulfide Formation (Figure S11d). If we make an assumption that the ligand-exchange process is happening to both directions continuously and that the already formed disulfide bridges do not break, we have the following process: random, two-way dithiol exchange (k_2, k_2', k_3, $k_3' > 0$) together with slow, one-way disulfide bridge formation ($k_1 > 0$; $k_1' = 0$; k_2, $k_3 \gg k_1$). Initially, the metastable state forms reaching dynamic equilibrium as before. Occasionally, disulfide forms bridging two MPCs together with a chain of two dithiols to form a dimer. As the ligand exchange is an ongoing process, the formed disulfide-bound dithiol chain can also be exchanged. This results in MPC without dithiols (more precisely, MPC that has lost one of its dithiol chains) and MPC with a chain of dithiols that is bound only from one end. MPC, with a chain bound only from one end, can bind to any other MPC without forming a new disulfide bridge. In other words, it behaves similar to MPC in the direct dithiol linking via ligand exchange, but instead of a single dithiol, it has a chain of dithiols attached to it. Slowly, every dithiol becomes part of a disulfide bridge, and in the end, the ligand-exchange process happens only with disulfide-bridged chains (see Figures 8d and S11d).

3.3.5.1. Chains of Two Dithiols. Let us ignore the formation of dithiol chains longer than two for a moment. The above process will end up to an equilibrium that is equal to the direct ligand-exchange linking with a single dithiol, except that a chain of two bridged disulphides connect MPCs instead of a single dithiol, that is, the chain acts as a single, long dithiol. The dithiol-to-MPC ratio of the direct linking case must be now replaced by chain-to-MPC ratio, but otherwise the two processes lead to exactly the same distribution.

Because a chain of two dithiols has twice as many dithiols as a single dithiol, the optimal dithiol linking activity is simply 70%, and the match with the experiment is as good as with a single dithiol and 35% linking activity.

3.3.5.2. Distribution of Chain Lengths. When chains longer than two dithiols form, the linking activity for the chain rises above 70%. The upper limit of 100% is reached, when the average chain length is approximately 2.85 dithiols, for example, with an exponential distribution, where a chain of two dithiols

has a probability of 54%, a chain of three 25%, a chain of four 11%, and so forth. This is relevant as we have previously demonstrated that BPDT, a dithiol of similar size as BMM-BPy **1**, forms dimers that have chains of three or more dithiols, in addition to chains of two.[36]

3.3.5.3. Dynamic Chains. Formation of chains longer than two dithiols is actually quite likely in the above scenario (see Figures 8d and S11d). Chains can grow or shrink via thiol-disulfide exchange,[45] as long as free thiol is present in the solution. Nevertheless, thiol-disulfide exchange reaction should have lower rate than ligand exchange, or otherwise, the distribution of oligomer yields would resemble more the dynamics of the disulfide linking without ligand exchange (see Figures 8c and S11c).

3.3.6. Summary of the Kinetic Model. After this discussion, we can summarize the requirements for reproducing the experimental data for BMM-BPy **1**: (1) equilibrium has been reached, (2) equilibrium has significant fraction of dithiols bound to MPCs, (3) equilibrium favors disulfide formation over breaking ($k_2 > k_2'$), and (4) ligand exchange happens more frequently than disulfide formation (k_1 or $k_3 \gg k_2$). Requirements 1 and 2 are supported directly by experimental observations. Requirement 3 is supported directly by experimental data for short chains of dithiols (and it is irrelevant for the unlikely case that linking happens only via single dithiols). Requirement 4 is supported by a combination of simulations and experiments. These requirements lead to a distribution of oligomers that originates (dominantly) from a process, where molecular bridges between MPCs form via ligand exchange. The simulated distribution reproduces the experimental data extremely well, when the average chain length for the molecular bridges is from a single dithiol up to 2.85 dithiols and the corresponding dithiol linking activity is from 35% up to 100%, respectively.

4. CONCLUSIONS

We have demonstrated that covalent linking between MPCs can be achieved with several different dithiols indicating generality of the ligand-exchange-based dithiol-linking approach. We observed that oligomer yields depend strongly on the dithiol used, but we found no simple trend based on the length of the dithiol or the functional groups in the dithiol. The yields depend strongly also on the dithiol-to-MPC ratio. Too low ratio leads to low oligomer yields, whereas too high ratio leads to excessive aggregation that reduces the yields. The optimal ratio is found in a relatively narrow range, for BMM-BPy **1**, between 1:1 and 2:1. Nevertheless, we showed that this range can be found in a straightforward way by a set of syntheses with different ratios followed by a PAGE run and scanning of the PAGE gel with a desktop scanner. The scanning approach is also suitable for extensive studies with different dithiols, MPCs, and reaction conditions to find trends and to gain deeper understanding of the dithiol-induced oligomerization of MPCs and nanoparticles.

We discussed several different options for a possible reaction mechanism based on the experimental observations obtained with our rapid scanning approach and simulations of reaction kinetics. We found that the best match with the experimental observations is achieved with simulations of a system at dynamic equilibrium, where MPCs are linked by short chains of disulfide-bridged dithiols that continuously form and break via a ligand-exchange process. The shortest possible chain length is one dithiol requiring that only ~35% of the dithiols are

contributing to the molecular bridges between MPCs, in the case of BMM-BPy **1**. However, based on our previous results on a similarly sized BPDT dithiol, the dithiol chains are more likely two or more dithiols long, the upper limit for the average chain length being ~2.85 dithiols, in the case of BMM-BPy **1**.

Our result that the system at dynamic equilibrium, where ligand exchange happens continuously, is in agreement with the recent studies of ligand exchange in MPCs.[40,46,47] This has implications for the stability of the system. As long as dithiol-to-MPC ratio remains unchanged and the distribution of oligomers is not altered in other ways, the system should be stable and self-repairing in solution. However, immediately, if the equilibrium distribution is disturbed, for example, by extracting one pure fraction of dimers, the system begins to re-equilibrate in solution converting dimers to monomers, trimers, tetramers, and so forth. We have observed slow redistribution of oligomers in our previous work, even in the absence of free thiol (see Supporting Information of ref 36). Therefore, a purified oligomer fraction must be stored as a dry solid, or some other approach, such as, encapsulation, must be applied to prevent further ligand exchange.

To conclude, our work on dithiol-induced oligomerization of MPCs provides tools and knowledge for developing controlled synthesis of covalently bound MPCs and nanoparticles for scientific and industrial applications.

■ ASSOCIATED CONTENT

Ⓢ Supporting Information

The Supporting Information is available free of charge on the ACS Publications website at DOI: 10.1021/acs.jpcc.8b02988.

> Calibration curve for converting scanned grayscale value to absorbance; TEM image of M band of BMM-BPy **1** linked AuMPCs; TEM image of D band of BMM-BPy **1** linked AuMPCs; TEM image of T band of BMM-BPy **1** linked AuMPCs; TEM image of Q-band of BMM-BPy **1** linked AuMPCs; UV−vis absorption spectrum of each visible band in the PAGE gel; PAGE gel showing bands of $Au_{\sim250}(p\text{-MBA})_n$ linked with BMM-BPy **1**; PAGE gel showing bands of $Au_{\sim250}(p\text{-MBA})_n$ linked with BMM-BPy **1**; absorbance of BMM-BPy **1** linked $Au_{\sim250}(p\text{-MBA})_n$ as a function of the PAGE running distance measured from the scanned grayscale image of the PAGE gel; statistics of multimers in the crude product as determined from TEM for two different linker-to-MPC molar ratios; absorbance of BMM-BPy **1** linked $Au_{\sim250}(p\text{-MBA})_n$ as a function of the PAGE running distance measured from the scanned grayscale image of the PAGE gel (blue), set of Gaussian functions with linear background fitted to data manually (orange), residual of the fit with respect to the experimental data (dark cyan), and molar ratios given in the top-right corner of each panel; schematic presentation of hypotheses and their outcomes; and fraction of MPCs after one-way, random, and independent ligand exchange that have no dithiols (black), one (blue), two (green), three (cyan), four (magenta), and more than four dithiols (dashed red) (PDF)

■ AUTHOR INFORMATION

Corresponding Authors

*E-mail: lauri.lehtovaara@jyu.fi (L.L.).

*E-mail: tanja.m.lahtinen@jyu.fi. Phone: +358 40805 3697 (T.L.).

ORCID Ⓘ

Eero Hulkko: 0000-0002-7536-5595

Tanja Lahtinen: 0000-0002-1747-6959

Notes

The authors declare no competing financial interest.

■ ACKNOWLEDGMENTS

■ REFERENCES

(1) Grzelczak, M.; Vermant, J.; Furst, E. M.; Liz-Marzán, L. M. Directed Self-Assembly of Nanoparticles. *ACS Nano* **2010**, *4*, 3591−3605.

(2) Halas, N. J.; Lal, S.; Chang, W.- S.; Link, S.; Nordlander, P. Plasmons in Strongly Coupled Metallic Nanostructures. *Chem. Rev.* **2011**, *111*, 3913−3961.

(3) Banik, M.; Rodriguez, K.; Hulkko, E.; Apkarian, V. A. Orientation-Dependent Handedness of Chiral Plasmons on Nanosphere Dimers: How to Turn a Right Hand into a Left Hand. *ACS Photonics* **2016**, *3*, 2482−2489.

(4) Homberger, M.; Simon, U. On the Application Potential of Gold Nanoparticles in Nanoelectronics and Biomedicine. *Philos. Trans. R. Soc., A* **2010**, *368*, 1405−1453.

(5) Nie, S.; Emory, S. R. Probing Single Molecules and Single Nanoparticles by Surface- Enhanced Raman Scattering. *Science* **1997**, *275*, 1102−1106.

(6) Yampolsky, S.; Fishman, D. A.; Dey, S.; Hulkko, E.; Banik, M.; Potma, E. O.; Apkarian, V. A. Seeing a Single Molecule Vibrate through Time-Resolved Coherent Anti-Stokes Raman Scattering. *Nat. Photonics* **2014**, *8*, 650−656.

(7) Watanabe, K.; Menzel, D.; Nilius, N.; Freund, H.-J. Photochemistry on Metal Nanoparticles. *Chem. Rev.* **2006**, *106*, 4301−4320.

(8) Brongersma, M. L.; Halas, N. J.; Nordlander, P. Plasmon-Induced Hot Carrier Science and Technology. *Nat. Nanotechnol.* **2015**, *10*, 25−34.

(9) Tapio, K.; Leppiniemi, J.; Shen, B.; Hytönen, V. P.; Fritzsche, W.; Toppari, J. J. Toward Single Electron Nanoelectronics Using Self-Assembled DNA Structure. *Nano Lett.* **2016**, *16*, 6780−6786.

(10) Klein, D. L.; McEuen, P. L. An Approach for Electrical Study of Single Nanocrystals. *Appl. Phys. Lett.* **1996**, *68*, 2574−2576.

(11) Quinten, M.; Kreibig, U.; Schönauer, D.; Genzel, L. Optical Absorption Spectra of Pairs of Small Metal Particles. *Surf. Sci.* **1985**, *156*, 741−750.

(12) Wang, X.; Li, G.; Chen, T.; Yang, M.; Zhang, Z.; Wu, T.; Chen, H. Polymer-Encapsulated Gold-Nanoparticle Dimers: Facile Preparation and Catalytical Application in Guided Growth of Dimeric ZnO-Nanowires. *Nano Lett.* **2008**, *8*, 2643−2647.

(13) Kleinman, S. L.; Sharma, B.; Blaber, M. G.; Henry, A.-I.; Valley, N.; Freeman, R. G.; Natan, M. J.; Schatz, G. C.; Van Duyne, R. P. Structure Enhancement Factor Relationships in Single Gold Nanoantennas by Surface-Enhanced Raman Excitation Spectroscopy. *J. Am. Chem. Soc.* **2013**, *135*, 301−308.

(14) Cunningham, A.; Mühlig, S.; Rockstuhl, C.; Bürgi, T. Coupling of Plasmon Resonances in Tunable Layered Arrays of Gold Nanoparticles. *J. Phys. Chem. C* **2011**, *115*, 8955−8960.

(15) Haynes, C. L.; Van Duyne, R. P. Nanosphere Lithography: A Versatile Nanofabrication Tool for Studies of Size-Dependent Nanoparticle Optics. *J. Phys. Chem. B* **2001**, *105*, 5599−5611.

(16) Claridge, S. A.; Liang, H. W.; Basu, S. R.; Fréchet, J. M. J.; Alivisatos, A. P. Isolation of Discrete Nanoparticle - DNA Conjugates for Plasmonic Applications. *Nano Lett.* **2008**, *8*, 1202−1206.

(17) Brousseau, L. C., III; Novak, J. P.; Marinakos, S. M.; Feldheim, D. L. Assembly of Phenylacetylene-Bridged Gold Nanocluster Dimers and Trimers. *Adv. Mater.* **1999**, *11*, 447−449.

(18) Dadosh, T.; Gordin, Y.; Krahne, R.; Khivrich, I.; Mahalu, D.; Frydman, V.; Sperling, J.; Yacoby, A.; Bar-Joseph, I. Measurement of the Conductance of Single Conjugated Molecules. *Nature* **2005**, *436*, 677−680.

(19) Durocher, S.; Rezaee, A.; Hamm, C.; Rangan, C.; Mittler, S.; Mutus, B. Disulfide-Linked, Gold Nanoparticle Based Reagent for Detecting Small Molecular Weight Thiols. *J. Am. Chem. Soc.* **2009**, *131*, 2475−2477.

(20) Tsai, D.-H.; Cho, T. J.; DelRio, F. W.; Gorham, J. M.; Zheng, J.; Tan, J.; Zachariah, M. R.; Hackley, V. A. Controlled Formation and Characterization of Dithiothreitol-Conjugated Gold Nanoparticle Clusters. *Langmuir* **2014**, *30*, 3397−3405.

(21) DeVries, G. A.; Brunnbauer, M.; Hu, Y.; Jackson, A. M.; Long, B.; Neltner, B. T.; Uzun, O.; Wunsch, B. H.; Stellacci, F. Divalent Metal Nanoparticles. *Science* **2007**, *315*, 358−361.

(22) Gadogbe, M.; Chen, M.; Zhao, X.; Saebo, S.; Beard, D. J.; Zhang, D. Can Para-Aryl-Dithiols Cross-Link Two Plasmonic Noble Nanoparticles as Monolayer Dithiolate Spacers. *J. Phys. Chem. C* **2015**, *119*, 6626−6633.

(23) Gang, O. Nanoparticle Assembly: from Fundamentals to Applications: Concluding Remarks. *Faraday Discuss.* **2016**, *186*, 529−537.

(24) Tsukuda, T.; Häkkinen, H. N. *Protected Metal Clusters: From Fundamentals to Applications*; Elsevier: Amsterdam, Netherlands, 2015.

(25) Jin, R.; Zeng, C.; Zhou, M.; Chen, Y. Atomically Precise Colloidal Metal Nanoclusters and Nanoparticles: Fundamentals and Opportunities. *Chem. Rev.* **2016**, *116*, 10346−10413.

(26) Heaven, M. W.; Dass, A.; White, P. S.; Holt, K. M.; Murray, R. W. Crystal Structure of the Gold Nanoparticle $[N(C_8H_{17})_4]$-$[Au_{25}(SCH_2CH_2Ph)_{18}]$. *J. Am. Chem. Soc.* **2008**, *130*, 3754−3755.

(27) Qian, H.; Eckenhoff, W. T.; Zhu, Y.; Pintauer, T.; Jin, R. Total Structure Determination of Thiolate-Protected Au_{38} Nanoparticles. *J. Am. Chem. Soc.* **2010**, *132*, 8280−8281.

(28) Jadzinsky, P. D.; Calero, G.; Ackerson, C. J.; Bushnell, D. A.; Kornberg, R. D. Structure of a Thiol Monolayer-Protected Gold Nanoparticle at 1.1 Å Resolution. *Science* **2007**, *318*, 430−433.

(29) Azubel, M.; Koivisto, J.; Malola, S.; Bushnell, D.; Hura, G. L.; Koh, A. L.; Tsunoyama, H.; Tsukuda, T.; Pettersson, M.; Häkkinen, H.; Kornberg, R. D. Electron Microscopy of Gold Nanoparticles at Atomic Resolution. *Science* **2014**, *345*, 909−912.

(30) Tvedte, L. M.; Ackerson, C. J. Size-Focusing Synthesis of Gold Nanoclusters with *p*-Mercaptobenzoic Acid. *J. Phys. Chem. A* **2014**, *118*, 8124−8128.

(31) Negishi, Y.; Nakazaki, T.; Malola, S.; Takano, S.; Niihori, Y.; Kurashige, W.; Yamazoe, S.; Tsukuda, T.; Häkkinen, H. A Critical Size for Emergence of Nonbulk Electronic and Geometric Structures in Dodecanethiolate-Protected Au Clusters. *J. Am. Chem. Soc.* **2015**, *137*, 1206−1212.

(32) Sakthivel, N. A.; Theivendran, S.; Ganeshraj, V.; Oliver, A. G.; Dass, A. Crystal Structure of Faradaurate-279: $Au_{279}(SPh\text{-}tBu)_{84}$ Plasmonic Nanocrystal Molecules. *J. Am. Chem. Soc.* **2017**, *139*, 15450−15459.

(33) Peterle, T.; Ringler, P.; Mayor, M. Gold Nanoparticles Stabilized by Acetylene-Functionalized Multidentate Thioether Ligands: Building Blocks for Nanoparticle Superstructures. *Adv. Funct. Mater.* **2009**, *19*, 3497−3506.

(34) Yao, H.; Yaomura, S. Emergence of Large Chiroptical Responses by Ligand Exchange Cross-Linking of Monolayer-Protected Gold Clusters with Chiral Dithiol. *Langmuir* **2013**, *29*, 6444−6451.

(35) Compel, W. S.; Wong, O. A.; Chen, X.; Yi, C.; Geiss, R.; Häkkinen, H.; Knappenberger, K. L., Jr; Ackerson, C. J. Dynamic Diglyme-Mediated Self-Assembly of Gold Nanoclusters. *ACS Nano* **2015**, *9*, 11690−11698.

(36) Lahtinen, T.; Hulkko, E.; Sokołowska, K.; Tero, T.-R.; Saarnio, V.; Lindgren, J.; Pettersson, M.; Häkkinen, H.; Lehtovaara, L. Covalently Linked Multimers of Gold Nanoclusters $Au_{102}(p\text{-MBA})_{44}$ and $Au_{\sim 250}$ (p-MBA)$_n$. *Nanoscale* **2016**, *8*, 18665−18674.

(37) Gürtler, A.; Kunz, N.; Gomolka, M.; Hornhardt, S.; Friedl, A. A.; McDonald, K.; Kohn, J. E.; Posch, A. Stain-Free Technology as a Normalization Tool in Western Blot Analysis. *Anal. Biochem.* **2013**, *433*, 105−111.

(38) Kimura, K.; Sugimoto, N.; Sato, S.; Yao, H.; Negishi, Y.; Tsukuda, T. Size Determination of Gold Clusters by Polyacrylamide Gel Electrophoresis in a Large Cluster Region. *J. Phys. Chem. C* **2009**, *113*, 14076−14082.

(39) Ghosh, A.; Hassinen, J.; Pulkkinen, P.; Tenhu, H.; Ras, R. H. A.; Pradeep, T. Simple and Efficient Separation of Atomically Precise Noble Metal Clusters. *Anal. Chem.* **2014**, *86*, 12185−12190.

(40) Salassa, G.; Sels, A.; Mancin, F.; Bürgi, T. Dynamic Nature of Thiolate Monolayer in $Au_{25}(SR)_{18}$ Nanoclusters. *ACS Nano* **2017**, *11*, 12609−12614.

(41) Asua, J. M.; McAuley, K. Y. C.; Kim, B. *Polymer Reaction Engineering*; Blackwell Publishing: Oxford, UK, 2008.

(42) Liu, K.; Nie, Z.; Zhao, N.; Li, W.; Rubinstein, M.; Kumacheva, E. Step-Growth Polymerization of Inorganic Nanoparticles. *Science* **2010**, *329*, 197−200.

(43) Carnall, J. M. A.; Waudby, C. A.; Belenguer, A. M.; Stuart, M. C. A.; Peyralans, J. J.-P.; Otto, S. Mechanosensitive Self-Replication Driven by Self-Organization. *Science* **2010**, *327*, 1502−1506.

(44) Otto, S.; Furlan, R. L. E.; Sanders, J. K. M. Dynamic Combinatorial Libraries of Macrocyclic Disulfides in Water. *J. Am. Chem. Soc.* **2000**, *122*, 12063−12064.

(45) Wang, J.; Xia, H.; Zhang, Y.; Lu, H.; Kamat, R.; Dobrynin, A. V.; Cheng, J.; Lin, Y. Nucleation-Controlled Polymerization of Nano-particles into Supramolecular Structures. *J. Am. Chem. Soc.* **2013**, *135*, 11417−11420.

(46) Sels, A.; Salassa, G.; Pollitt, S.; Guglieri, C.; Rupprecher, G.; Barrabés, N.; Bürgi, T. Structural Investigation of the Ligand Exchange Reaction with Rigid Dithiol on Doped (Pt, Pd) Au_{25} Clusters. *J. Phys. Chem. C* **2017**, *121*, 10919−10926.

(47) Heinecke, C. L.; Ni, T. W.; Malola, S.; Mäkinen, V.; Wong, O. A.; Häkkinen, H.; Ackerson, C. J. Structural and Theoretical Basis for Ligand Exchange on Thiolate Monolayer Protected Gold Nano-clusters. *J. Am. Chem. Soc.* **2012**, *134*, 13316−13322.

III

TOWARDS CONTROLLED SYNTHESIS OF WATER-SOLUBLE GOLD NANOCLUSTERS: SYNTHESIS AND ANALYSIS

by

Karolina Sokołowska, Sami Malola, Manu Lahtinen, Ville Saarnio,
Perttu Permi, Katariina Koskinen, Matti Jalasvuori, Hannu Häkkinen,
Lauri Lehtovaara and Tanja Lahtinen

Towards Controlled Synthesis of Water-Soluble Gold Nanoclusters: Synthesis and Analysis

Karolina Sokołowska,[†] Sami Malola,[‡] Manu Lahtinen,[†] Ville Saarnio,[†] Perttu Permi,[†,§] Katariina Koskinen,[§] Matti Jalasvuori,[§] Hannu Häkkinen,[†,‡] Lauri Lehtovaara,[†] and Tanja Lahtinen*,[†]

[†]Department of Chemistry, Nanoscience Center, [‡]Department of Physics, Nanoscience Center, and [§]Department of Biological and Environmental Science, Nanoscience Center, University of Jyväskylä, P.O. Box 35, 40014 Jyväskylä, Finland

S *Supporting Information*

ABSTRACT: Water-soluble gold nanoclusters with well-defined molecular structures and stability possess particular biophysical properties making them excellent candidates for biological applications as well as for fundamental spectroscopic studies. The currently existing synthetic protocols for atomically monodisperse thiolate-protected gold nanoclusters (AuMPCs) have been widely expanded with organothiolates, yet the direct synthesis reports for water-soluble AuMPCs are still deficient. Here, we demonstrate a wet-chemistry pH-controlled synthesis of two large water-soluble nanoclusters utilizing *p*-mercaptobenzoic acid (*p*MBA), affording different sizes of plasmonic AuMPCs on the preparative scale (∼7 mg). AuMPCs are essentially homogenous in size and are stable in solution and the solid state. Number of characterization methods were used to gain detailed information about the size, symmetry, molecular composition, and structure of these systems, i.e., high-resolution transmission electron microscopy, powder X-ray diffraction, NMR, UV−vis, thermogravimetry, and polyacrylamide gel electrophoresis. On the basis of the conducted experimental analyses and computationally aided predictions it can be evidenced that both clusters exhibit twinned face-centered cubic symmetry with the molecular composition of $Au_{210−230}(pMBA)_{70−80}$ and $Au_{426−442}(pMBA)_{112−115}$, referred from now on as Au250 and Au500, respectively. For future reference, toxicity of both gold clusters in various concentrations on cultures of Gram-positive and Gram-negative bacteria was investigated.
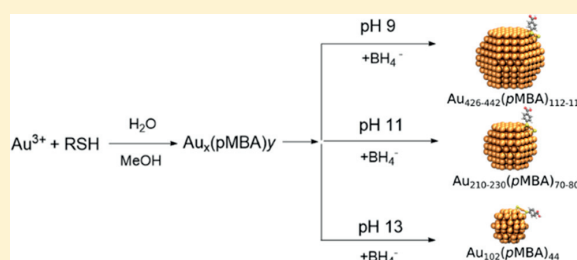
1. INTRODUCTION

The unique properties of gold nanoparticles have been studied extensively.[1−4] The size and shape of the particles define their electronic and physical properties, whereas tuning the nature of the protecting organic layer gives a control of the solubility and chemical functionality of the particles.[1] The versatile surface chemistry and size-dependent properties make them universal materials in high technology applications such as sensory probes, electronic conductors, therapeutic agents, drug delivery in biological and medical applications, and catalysis.[4−11]

Colloidal nanoparticles are not well suited for accurate studies of their chemistry. A typical nanoparticle synthesis produces a polydisperse sample of different sizes, shapes, and surface structures. Therefore, experiments that require atomic-level control are extremely difficult to carry out. In this regard, monolayer-protected gold clusters (AuMPCs) are small (usually <2 nm) nanoparticles with well-defined structures, consisting of a metallic core and a protecting ligand layer.[12−14] The structures range from small, more molecular-like species, with quantized electronic transitions, to larger, more nanoparticle-like clusters with hundreds of metal atoms, exhibiting localized surface plasmon resonance (SPR).[3,15,16] Contrary to colloidal gold nanoparticles, AuMPC synthesis produces a well-organized structure, with a specific number of atoms,

similar to a molecule that has enabled accurate studies of their chemistry, as well as the direct comparison of experimental and theoretical results.[17] Currently, many sizes of organosoluble nanoclusters are widely deployed;[18−23] however, the direct syntheses of larger (>200 gold atoms) water-soluble nanoclusters are still not yet fully understood.

Water-soluble gold nanoclusters were previously reported as universal labeling tools for bioimaging due to contrast properties, low toxicity, and high solubility. For example, $Au_{102}(pMBA)_{44}$ was described as a good tracking candidate for accurate site-specific covalent conjugation to the viral capsid surface where the covalently bound nanoclusters keep the viruses stable, allowing better visualization of their entry into complex endosomal structures.[4] The surface properties, particularly the solvent/organic interface of *p*-mercaptobenzoic acid (*p*MBA)-protected gold clusters, are altered depending on the protonation state of the cluster.[1] The clusters become water-soluble only when the carboxylic group of the *p*MBA-ligand is deprotonated, which is an important aspect for chemical modifications. Moreover, water-soluble clusters do

not require any toxic solvent treatment, which makes them a good candidate for green chemistry approaches, and widen the range of applicability to more polar solvents.

AuMPCs have a great response to light at the resonant wavelength.[23,24] The plasmonic and near-infrared (NIR) absorbance is well detectable in deep-tissue samples. We have previously studied covalently bound multimers of gold nanoclusters and discovered that the examined system displays coupled plasmonic modes in the NIR therapeutic spectral window (650−1350 nm) which could be potentially used for imaging biological samples.[25] Ability to covalently link AuMPCs through the conductive molecule opens up new prospects to study the fundamental physical properties of molecular electronic devices and internal motions of the particles and binding ligands.[26] Recently, Bürgi et al. reported the successful assembly of $Au_{25}(SBut)_{18}$ multimers via ligand exchange and studied electron transfer between clusters.[27] Developments of larger precise analogs of structures that can be modeled with the ab initio (density functional theory) level of theory could expand the knowledge of quantum plasmonics and emergence of bulk properties of metals.

Currently existing synthetic protocols for producing AuMPCs are most extensively carried out using organosoluble ligands, organothiolates, in particular phenylethane-thiol.[18−22,30] The synthesis generally produces a set of heterogeneous particles, requiring etching, size focusing, and/or other methods to narrow size distribution.[18,27−33] The key, to the characteristic stability and the atomically precise size control of those particles is the role of the protecting ligand layer. Covalently bound ligands govern the kinetic control and thermodynamic selection of the robust sizes in synthesis.[3] In contrast to the AuMPCs, the colloidal gold nanoparticles are typically protected by a weakly bound surfactant or even without any protecting ligand layer, significantly affecting their stability leading to extensive aggregation. For water-soluble gold nanoclusters, the synthetic control is obtained by the precise selection of reaction conditions, in a way that the single-sized product is favored.[34,35] To produce a large panel of uniform clusters of chosen sizes, the synthetic parameters of these direct synthesis methods need to be explored thoroughly.[36] Among several water-soluble thiols that can stabilize gold nanoclusters, mercaptobenzoic acid (MBA) has been actively used.[31−41] More specifically, syntheses have been developed for 3-MBA ($mMBA$)[37−40]- and 4-MBA ($pMBA$)[31−36,41,42]-protected clusters, e.g., $Au_{68}(mMBA)_{32}$, $Au_{144}(mMBA)_n$, and $Au_{144}(pMBA)_{60}$, $Au_{102}(pMBA)_{44}$ and $Au_{146}(pMBA)_{57}$. Among $pMBA$-stabilized particles, only $Au_{144}(pMBA)_{60}$ and $Au_{102}(pMBA)_{44}$ were synthesized without any size focusing methods, resulting in the direct synthesis protocol. In this work, we are focusing on $pMBA$-stabilized gold nanoclusters to study synthetic parameters of direct synthesis methods.

Precise characterization of individual gold nanoclusters with respect to their composition and structure has been made by various techniques.[38,40,41] However, despite significant development in structure determination techniques within past few years, atomic-level information of clusters bigger than 100 gold atoms is still a grand challenge to achieve, particularly for water-soluble clusters. Thereby, with the lack of information on structure−property relationship applicability of the clusters remains limited.

In this paper, through the systematic variation of reaction conditions, we synthesized stable, water-soluble $pMBA$-thiolate

gold nanoclusters. We found that controlling pH in different $MeOH/H_2O$ conditions produces different sizes of $pMBA$-clusters. To our knowledge, this is the first straightforward wet-chemistry synthesis to produce larger, water-soluble $pMBA$-protected gold nanoclusters in milligram scale. Experimental and theoretical evidence helped us to predict molecular composition of these larger $pMBA$-clusters to be $Au_{210−230}(pMBA)_{70−80}$ and $Au_{426−442}(pMBA)_{112−115}$ referred further on as Au250 (synthesis previously published by us)[25,42] and Au500, respectively. The synthesized clusters are stable in both solid and solution at room temperature for at least 6 months, as determined by polyacrylamide gel electrophoresis (PAGE) and UV−vis analysis. For future studies, the toxicity of both gold clusters was also studied. As a result, neither Au250 or Au500 caused significant decrease or elevation in the growth densities of *Bacillus thuringiensis* HER1410, *Escherichia coli* HB101, or *Klebsiella pneumoniae*.

2. MATERIALS AND EXPERIMENTAL METHODS

2.1. Materials. All reagents were commercial and used as received unless otherwise mentioned.

2.2. Synthesis and Separation. $pMBA$-thiol-protected AuMPCs were synthesized under pH-controlled conditions. Different solvent compositions were used to fine-tune the reduction kinetics of the MPC growth leading to the discrete cluster size (Figure 1). Smaller nanocluster Au250 was

Figure 1. PAGE bands of Au102, Au250, and Au500 nanoclusters.

synthesized at higher pH (around 11) with a mixed solvent of 26% MeOH (v/v) in water,[25] whereas larger nanocluster Au500 was synthesized at a slightly lower pH (around 9) with a solvent mixture of 24% MeOH in water.

In a typical synthesis, $HAuCl_4$ first reacts with excess $pMBA$-thiol in basic aqueous solution to form colorless $Au(I)SR$ aggregated complexes. Then, $NaBH_4$ is added to reduce $Au(I)SR$ into $Au_x(pMBA)_y$. The synthesis of smaller Au250 nanocluster produces one single size of AuMPCs. Detailed description of the syntheses and purification are given in the Supporting Information (SI).

Due to the lack of crystal structure, several characterization techniques were conducted to gain detailed information about the size, symmetry, molecular composition, and structure of these systems. The as-obtained products were analyzed using polyacrylamide gel electrophoresis (PAGE), thermogravimetric analysis (TGA), powder X-ray diffraction (PXRD), NMR

Scheme 1. Schematic Representation of Gold Nanocluster Synthesis

spectroscopy, high-resolution transmission electron microscopy (HR-TEM), UV–vis spectroscopy, and mass spectrometry. Unfortunately, all the attempts to measure ESI-mass spectrometry have not been successful, most likely due to large amounts of possible charge states of the protective *p*MBA-ligand layer as shown in Scheme 1.

2.3. Polyacrylamide Gel Electrophoresis (PAGE). PAGE was run on a 15% polyacrylamide gel (29:1 acrylamide/bisacrylamide) using 2× TBE run buffer in a Bio-Rad Mini-Protean Tetra System gel electrophoresis apparatus at 130 V.

2.4. Spectroscopy. *2.4.1. NMR.* ^{1}H NMR spectra were recorded on a Bruker Avance III HD 800 MHz spectrometer, equipped with a cryogenically cooled ^{1}H, ^{13}C, ^{15}N triple-resonance PFG Cryoprobe. All spectra were measured at 303 K.

2.4.2. UV–vis Spectroscopy. The spectra of AuMPCs were measured in dH$_2$O using quartz cuvettes and a PerkinElmer Lambda 850 UV/Vis-spectrometer with 2 nm resolution.

2.4.3. Thermogravimetric Analysis (TG). Thermal properties of Au nanoclusters were examined by a PerkinElmer Pyris 1 thermogravimetric analyzer. TG runs were carried out in an open platinum pan under an air atmosphere (flow rate of 60 mL/min) with a heating rate of 10 °C/min in the temperature range of 20–800 °C. Analyses were made twice for each cluster type. Temperature calibration of the analyzer was made by using Curie transition temperatures of Alumel, nickel, Perkalloy, and Fe standards. The weight balance was calibrated by measuring the standard weight of 50 mg at room temperature. The sample weights used in the measurements were about 1–3 mg.

2.4.4. Powder X-ray Diffraction (PXRD) Measurements. The powder X-ray diffraction data were measured by a PANalytical X'Pert PRO diffractometer in Bragg–Brentano geometry using Cu Ka1 radiation (Johannsson type monochromator; λ = 1.5406 Å) with 45 kV and 40 mA power settings. A sample was prepared on a reflection-free silicon-made plate with an aid of petrolatum jelly. Diffraction patterns were recorded from a spinning sample by an X'Celerator detector using a continuous scanning mode in a 2θ range of 2–140° with a step size of 0.017° and with the overall data recording time of ~45 h per pattern. Data processing was made with the PANalytical HighScore Plus version 4.7 program and phase identification data were retrieved from ICDD PD4+ database.[43] Theoretical powder diffraction curves were calculated as described in ref 44.

2.4.5. High-Resolution Transmission Electron Microscopy (HR-TEM). HR-TEM samples were prepared by drop-casting 8 μL of aqueous solution of clusters on a glow discharged 400 mesh lacey carbon copper grid. Solution was allowed to adsorb

for 15 min, after which the excess sample was removed and washed with water and MeOH. Grid was allowed to dry overnight. The samples were imaged with 0.2 nm point resolution using JEOL JEM-2200FS Cs-corrected HR-TEM operated at 200 kV.

Simulated HR-TEM images were created from a cluster model with the following algorithm. A unit vector with random orientation was sampled from uniform angular distribution. Each gold atom in the cluster model was replaced by a Gaussian density distribution with a variance of 1.4 Å and the density was projected onto the plane defined by the random unit vector. Finally, the resulting projected density was converted to a grayscale image.

2.5. Prediction of the Molecular Composition. Computationally aided predictions of the molecular composition were done in three ways. In the first approach, theoretically calculated TG percentages of the selected structurally known reference systems were correlated with the number of Au atoms and the ligands in the systems. In the second approach, the bare Au-cluster models of twinned face-centered cubic (fcc) symmetry were used to estimate the number of metal atoms in the core of the synthesized clusters. In the third approach, compositions were predicted by using linear dependence of the number of gold atoms in the cluster on the volume of the cluster and also by the linear dependence of the number of ligands on the surface area of the cluster. More detailed information is provided in the SI.

2.6. Bacteria/Toxicity Test. Bacterial biotoxicity of Au250 and Au500 was spectroscopically determined against three bacterial species, *B. thuringiensis* strain HER1410 (Gram-positive), common lab-strain *E. coli* K-12 HB101 (Gram-negative), and multidrug-resistant patient isolate *K. pneumoniae.* (Gram-negative). All strains were initially cultured in 5 mL of LB medium in +37 °C and shaken at 210 rpm overnight. Cultures for spectroscopic assay were prepared by adding aqueous solution of Au250 or Au500 in the final concentrations of 0.14, 1.4, 14, or 140 and 0.13, 1.3, 13, or 130 μg/mL, respectively, into 1:1000 diluted bacterial cultures. The absorbance of bacterial cultures was measured at +37 °C at 595 nm in 5 min intervals for 20 h to determine the bacterial growth and the maximum population densities. The absorption of Au250, Au500, and growth media was subtracted from the maximum population densities to measure the bacterial cell-induced absorption under different Au250 and Au500 exposures. Each measurement was conducted three times.

3. RESULTS AND DISCUSSION

3.1. Synthesis Products. Two parameters, pH and MeOH concentrations affected the outcome of the synthesis. Au nanoclusters were synthesized by pH control in different

Table 1. Synthesis Protocols of pMBA-Protected Gold Nanoclusters[a]

nanoclusters	polymerization				reduction		purification MeOH (%)
	pMBA	HAuCl$_4$	MeOH (%)	pH	MeOH (%)	NaBH$_4$	
Au102	3	1	47	13	47	1.1	60
Au250	6	1	28	11	26	1.8	pure product without fractional precipitation
Au500	6	1	25	9	25	1.8	25

[a]The values in columns 2nd, 3rd, and 7th correspond to the molar ratios
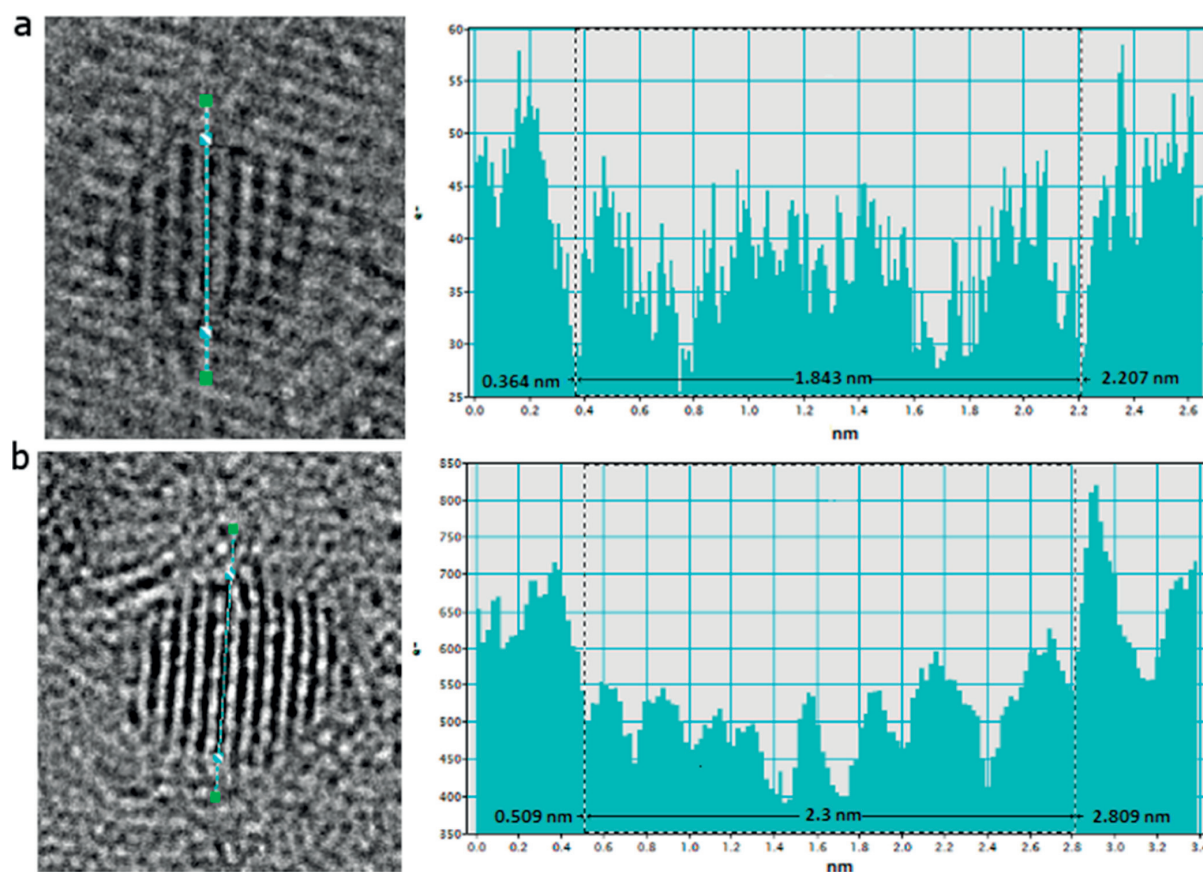

Figure 2. HR-TEM images of the assumed (a) Au250 and (b) Au500 pMBA-protected nanoclusters. Right panel corresponds to the histogram showing the upper size of the selected particle on the left panel.

MeOH compositions yielding two different discrete products of a stable water-soluble cluster protected by pMBA-thiol in milligram scale. These syntheses do not involve any additional size-focusing step and in the case of Au250, the synthesis produces only one discrete size of particle. Additionally, the Au$_{102}$(pMBA)$_{44}$ nanocluster was synthesized as a good reference point to compare synthetic trends, dispersity, and the size of the particles. The reference Au$_{102}$(pMBA)$_{44}$ nanocluster was synthesized following previously reported synthesis.[34] The polymerization step requires a relatively high pH of ~13 and conditions of 47% of MeOH. To enable facile comparison of the reaction conditions, we divided the reaction protocols into 3 stages to extract the information on direct synthesis conditions. The first stage involves the polymerization process, second stage involves reduction, and the last stage involves purification (Table 1).

To synthesize smaller Au250 nanoclusters, HAuCl$_4$ and pMBA-thiol were dissolved in methanol and mixed, leading to the formation of a white precipitate. The initial Au$_x$(pMBA)$_y$ polymerization step requires treatment at a pH of ~11 prior to reduction, nucleating the growth of the metal core. After reduction of Au(I)−pMBA precursors with NaBH$_4$, excess of methanol is added and the reaction is quenched producing one discrete size of particle.

Upon lowering the pH, a larger Au500 nanocluster was found. HAuCl$_4$ and pMBA-thiol were dissolved in 86% of methanol rapidly forming a white precipitate, which was dissolved at pH ~ 9. The final product still contains a polydisperse cluster mixture, similar to Au$_{102}$(pMBA)$_{44}$ synthesis, and requires fractional precipitation. The separation is done at 25% of methanol and centrifuged at 5000g for 15 min. Next, the supernatant is adjusted to 80% methanol and

centrifuged. The pellet from precipitation at 80% methanol is the final product.

The pH value of the pMBA-cluster effects its protonation state and surface properties. The solvent/organic interface of the protecting ligand can be easily altered becoming water-soluble when the carboxylic group of the pMBA-ligand is deprotonated and methanol-soluble when protonated. At the same time, by tuning the pH value during the polymerization step, the size of the cluster can be controlled. The larger Au500 cluster favors slightly lower but still alkaline pH 9 and low MeOH concentration of 25%, whereas Au250 was synthesized at pH 11 and the solvent mixture of 28% (v/v) MeOH in water.

When dissolved in water the new products display different colors (yellowish, brownish, reddish) indicating that they have different sizes. The syntheses of both sizes produced mg-quantities (~7 mg) of solid material. Each reaction product was analyzed using polyacrylamide gel electrophoresis (PAGE) and based on the initial size estimation they were assigned as Au250 and Au500, respectively.

Recently, Azubel and Kornberg reported that apart from the thiol-to-gold ratio, the size and uniformity of mMBA gold particles is highly dependent on the adjustment of pH.[37] In contrast to 4-MBA (pMBA), the mMBA ligand induces different properties for the Au nanocluster mainly due to the meta-position of the acidic group in the phenyl ring, thus resulting in a dissimilar ligand orientation and geometry.[39] Nevertheless, smaller mMBA clusters of 68 and 144 gold atoms were synthesized at pH 13.[37] In the case of 4-MBA clusters, $Au_{102}(pMBA)_{44}$ (Au102) is synthesized also at pH 13 and these larger ones Au250 and Au500 by lowering the pH from 11 to 9. The synthesis conditions for smaller water-soluble MBA-protected nanocluster seem to favor high pH conditions.

3.2. Characterization of AuMPCs. The size range information of the crude product was preliminarily acquired from their mobility in PAGE gel (Figure 2). The size information and the number of gold atoms per product were further examined with HR-TEM. The determined Au contents were further used for estimating number of ligands by thermogravimetry. With UV−vis spectroscopy, new insight into size-dependent evolution of surface plasmon resonance (Figure 3) was obtained. The powder X-ray diffraction (PXRD) technique was used to validate the structural features that were obtained by HR-TEM. Finally, based on all the gathered data about the size, symmetry, molecular composition, and structure of these clusters, computational prediction was developed for representing structural features of water-soluble pMBA-protected Au250 and Au500 nanoclusters.

3.2.1. PAGE. Dispersity and the size of the prepared AuMPCs were compared with the reference cluster $Au_{102}(pMBA)_{44}$ (Figures 1 and S1). The products formed by the wet-chemistry approach showed up as a single well-defined band in PAGE, indicating monodispersity of AuMPCs. The particles were initially analyzed by the determination of electrophoretic mobility. Both products had lower mobility than $Au_{102}(pMBA)_{44}$ in the same PAGE run indicating larger sized clusters. Using Au102 as a reference sample, retention factors (r_f) were determined to be 0.77 and 0.64 for Au250 and Au500, respectively. The product possesses stability in both solid and solution at room temperature for at least 6 months, as determined by PAGE and UV−vis analysis.

3.2.2. HR-TEM. Images of the AuMPCs were acquired by the Gatan software, which was also used to determine the diameter
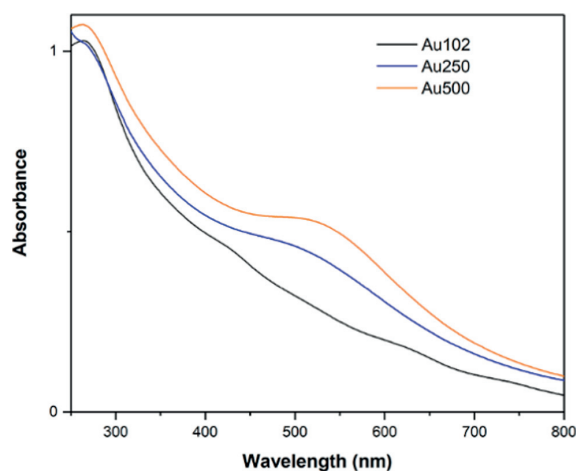

Figure 3. UV−vis spectra of Au102 (black), Au250 (blue), and Au500 (orange) clusters in dH_2O. A distinct absorption feature corresponding to a localized surface plasmon resonance is observed at 530 nm for the Au250 and Au500 nanoclusters.

of the selected particles (Figures 2 and S2−S4). The biggest challenge in HR-TEM measurements is its interpretation due to the number of interferences (and low signal-noise ratio when measuring at atomic resolution). Therefore, edge-to-edge particle size determination is often difficult. The diameters in Figure 2 correspond to the maximum limit of the size, in other words, the size with an error limit of 0.1 nm. We estimated the diameter of the smaller product to be 1.7 ± 0.1 nm, which fits to our previously reported size estimation[25] that was based on the Gaussian fit from low-resolution TEM images, yielding the diameter in the range of 1.6 ± 0.3 nm (Figure 2a). The metal core diameter of the larger product was determined to be 2.2±0.1 nm (Figures 2b and S4).

3.2.3. UV−vis. The optical spectra obtained from the two clusters were also compared to the reference spectrum of $Au_{102}(pMBA)_{44}$ (Figure 3). In contrast to $Au_{102}(pMBA)_{44}$, both clusters exhibited an absorption peak at 530 nm which is consistent with the surface plasmon resonance (SPR).[23] With an increase in the cluster size, the SPR features increases. The same properties were observed in the case of Au250 and Au500 clusters. As far as we know, the prepared particles are the biggest water-soluble nanoclusters synthesized by direct chemical approaches and demonstrating SPR. The spectrum of Au250 is compatible to the recently published spectra of 51,[33] 45,[23] and 53 kDa clusters,[23] with the estimated number of gold atoms at 250, 226, and 253, respectively. In case of Au500, the absorption spectrum is compatible with the reported spectra of 75[23] and 88 kDa clusters[33] with estimated gold atoms at 356 and 459.

3.2.4. ${}^1H$ NMR. ${}^1H$ spectra of Au250 and Au500 exhibit a typical broad signal for gold clusters between 5.2 and 9.2 ppm (Figure S5). Additionally, two sharp signals (doublets) can be seen at 7.60 and 7.79 ppm in both spectra, which fit to the free pMBA-ligand. However, the ${}^1H$ spectrum of Au500 shows an additional fine structure in comparison to Au250, which is relatively featureless. Without considering the free pMBA signals, the Au500 spectrum shows 14 doublet signals (7.92, 7.82, 7.70, 7.65, 7.34, 7.30, 7.14, 6.66, 6.62, 6.55, 6.51, 6.25, 6.19, and 5.79 ppm) and a singlet at 7.61 ppm. These peaks are characteristic for the Au500 nanocluster, but it is still not clear

whether they belong to the cluster structures. In different synthesis products, they appear at the same positions, but with varying intensities.

3.2.5. Thermogravimetric Analysis (TG). The weight loss of organic substance upon heating is commonly used to estimate the number of ligands in monolayer-protected gold clusters (the image of the Au residuals after a TG run, see Figure S6). Thermal stability and number of organosulfur ligands on the Au_n nanoclusters (n = 102, 250, 500) were examined by thermogravimetric analysis (TG). In Figure 4, recorded TG
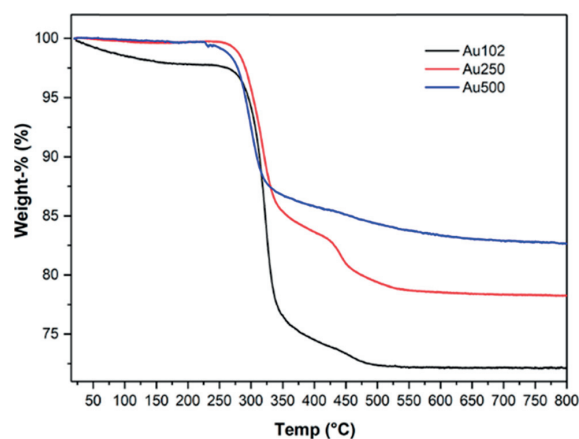

Figure 4. TG curves of Au102, Au250, and Au500 clusters measured with a heating rate of 10 °C/min under an air atmosphere.

curves show gentle descending weight loss (sample dependently 0.4−2 wt %) from 20 up to about 200 °C (Table 2) that is caused by the gradual evaporation of residual surface bound water. Thermal decomposition of all three Au-clusters initiate slowly above 220 °C followed by major weight loss from 270 to 500, 600, and 700 °C along with an increase in the size of the Au-cluster. The observed weight loss of the major steps corresponds to thermal decomposition processes and/or desorption of surface ligands (*p*MBA), and were determined to be 25.92, 21.32, and 19.60 wt % for Au102, Au250, and Au500 clusters, respectively (Table 2).

The number of surface ligands can be estimated via the observed residual weight of each TG run (74.08, 78.68, and 83.11% for Au102, Au250, and Au500, respectively) by calculating those as moles of Au. The number of gold atoms used here are based on computationally aided predictions explained in detail later in Section 3.2.6. The original molar mass of the $Au_x(SR)_y$ cluster can then be calculated based on the expected 1 to 1 stoichiometry between the gold containing residual and the original $Au_x(SR)_y$ cluster, from which the number of surface ligands $(SR)_y$ can then be evaluated by taking into account the molar mass of the (SR) ligand. Functionality of the method was confirmed by the reference

cluster Au102 for which 45 ± 1 surface ligands are determined by the analysis, agreeing well with the number of ligands (44) reported in the single crystal structure of the cluster by Jadzinsky et al.[45] Similarly, 73−80 and 111−116 surface ligands were determined for Au250 and Au500 clusters, respectively. The determined number of ligands also match remarkably well with those obtained by our computational predictions (see Section 3.2.6).

3.2.6. Toxicity on Bacteria. Neither Au250 nor Au500 caused significant decrease or elevation in the growth densities of *B. thuringiensis* HER1410, *E. coli* HB101, or *K. pneumoniae* in concentrations 0.14−14 μg/mL of Au250 or 0.13−13 μg/mL of Au500 (Figure 5). In higher concentrations (140 and 130
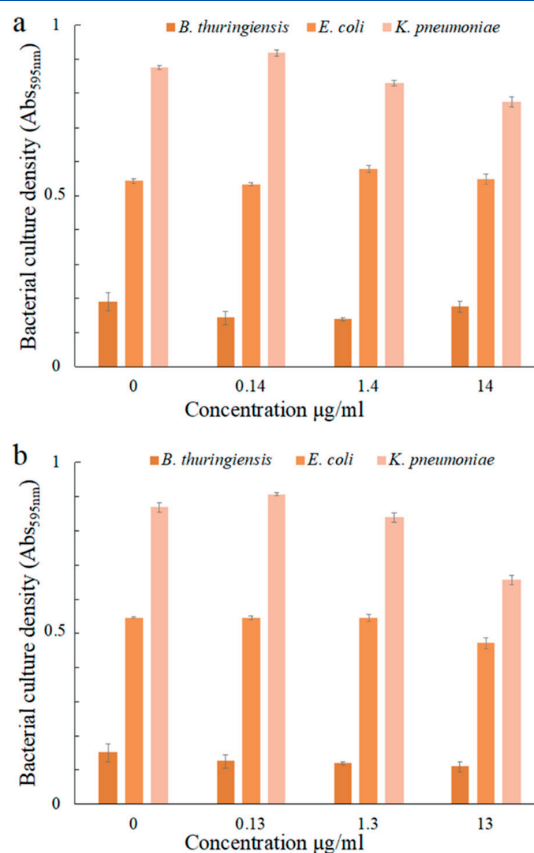

Figure 5. Spectroscopic biotoxicity assay of gold nanoclusters (a) Au250 and (b) Au500 on bacterial species *B. thuringiensis*, *E. coli*, and *K. pneumoniae*. Maximum absorption (595 nm) of bacterial cultures were measured in the presence of either Au250 or Au500 in different concentrations during 20 h of cultivation (N = 3). The slight decline of absorbance in the highest concentration was due to increasing background absorption. Error bars: standard deviation.

Table 2. TG Results for Au102, Au250, and Au500 Nanoclusters

sample name	1st weight loss[a] (%)	temp. (°C)	2nd weight loss[b] (%)	temp. (°C)	residual[c] (%)	no. of ligands	no. of Au atoms
Au102	2.13	24−214	25.92	214−800	74.08	45	102
Au250	0.37	24−190	21.32	190−800	78.68	73−80	210−230
Au500	0.40	24−192	16.90	192−800	83.11	111−116	426−442

[a]Residual water. [b]Ligand removal. [c]Residual weight corresponding to gold content.

μg/mL), the self-absorption of Au250 and Au500 obscured the optical density of the cultures, and thus the changes in bacterial growth could not be reliably observed. Nevertheless, based on the results, Au250 and Au500 do not seem to affect bacterial viability.

3.3. Exploring the Atomic Structure. Before predicting the molecular compositions of the clusters, we first present a short discussion on the structural patterns of water-soluble *p*MBA-protected cluster systems. We compare measured powder X-ray diffraction results of the synthesized clusters with the symmetries of selected, structurally known, thiolate-protected clusters. We also present a range for possible basis for the metal core structure of Au250 and Au500 nanoclusters based on experimental and theoretical data.

3.3.1. Powder X-ray Diffraction (PXRD) Analysis. Comparison of the experimental XRD patterns of Au250 and Au500 nanoclusters with the calculated reference systems of $Au_{146}(pMBA)_{57}$, $Au_{246}(SC_6H_4CH_3)_{80}$, and $Au_{279}(TBBT)_{84}$ is illustrated in Figure 6. The Au_{246} nanocluster displays the
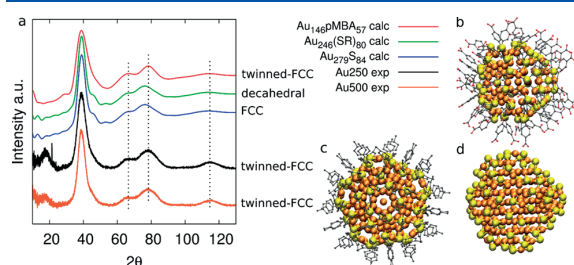

Figure 6. (a) Diffraction patterns of the nanoclusters. Comparison of the experimental patterns of Au250 (black line) and Au500 (orange line) with the calculated patterns of Au146, Au246, and Au279 clusters. The diffraction hump and very sharp peak at 20° 2θ in experimental patterns are caused by the sample holder and the adhesive used for attaching the samples to the holder. Structural models of (b) $Au_{146}(pMBA)_{57}$, (c) $Au_{246}(SR)_8$, and (d) $Au_{279}S_{84}$.

decahedral core and $Au_{146}(pMBA)_{57}$ represents the largest so far solved water-soluble cluster with the fcc-based twinned core.[41] The XRD patterns of both clusters show the strongest diffraction peak at ∼40° 2θ, two relatively broad peaks at ∼60−80° 2θ, and some minor peaks at ∼45 and ∼50° 2θ. With phase identification routine, the observed diffraction peaks are characteristic for gold phase crystallizing in the cubic face-centered crystal system and no additional unindexed peaks remain in the patterns (large hump 15−20° and very sharp

peak at 21.4° 2θ originates from a sample holder/adhesive substance).[43] The calculated XRD pattern of $Au_{146}(pMBA)_{57}$ is remarkably similar to the experimental data of Au250 and Au500 clusters. The diffraction peaks at 38.8, 66.2, and 75.7° in both experimental patterns have similar shape features and are located at the equal diffraction angles compared to that in the Au146 pattern. Instead, the simulated patterns of decahedral Au246 and fcc Au279 clusters show additional minor peaks at ∼45 and ∼50° 2θ that are not visible in the XRD patterns of Au500 and Au250 clusters. Moreover, the peak maximums of the main peaks in Au246 and Au279 are also somewhat shifted to lower 2θ angles and the shape properties of the peaks are subtly different. Described observations suggest that the metal core of both Au250 and Au500 nanoclusters most likely adopts the fcc symmetry, which is also twinned as indicated by the computational analyses represented in the following chapters.

3.3.2. Building Model for Twinned fcc Metal Core Structures of Au250 and Au500. On the basis of the obtained information from powder XRD analysis, we start evaluating possible basis for the metal core structure of Au250 and Au500 nanoclusters. Ranges of possible candidates with the same twinned fcc arrangement are shown in Figure 7. The size range of the clusters was estimated based on PAGE. Furthermore, the estimated diameters of the clusters from HR-TEM, 1.7 ± 0.1 nm for Au250 and 2.2 ± 0.1 nm for Au500 are in agreement with the modeled metal core of Au_{201} and Au_{405}, respectively. Therefore, we believe that they are possible candidates to start building a structural model of the synthesized clusters.

3.3.3. HR-TEM Image versus Twinned fcc Core. HR-TEM images represent further the symmetries of the AuMPCs. The simulated HR-TEM images of the Au_{201} metal core clearly support the imaging experiments of Au250 (Figure 8). The observation of the lattice fringes in Figure 8c clearly shows the effects that can be only seen in both, fcc and twinned fcc arrangements. The experimental Figure 8c shows 7−9 rows of atomic layer giving excellent estimation of structural information at atomic resolution. The uncertainty in image interpretation is often due to poor contrast and number of interferences. Therefore, we simulated images of the Au_{201} metal core and compared them with our experimental findings. In the simulated image, there are 7 rows of the atomic layer (Figure 8c). The simulated images contain only the metal core atoms and the question arises how protected is the gold core under electron beam. In other words, for analysis, it is important to know whether the Au−S layer protecting the gold
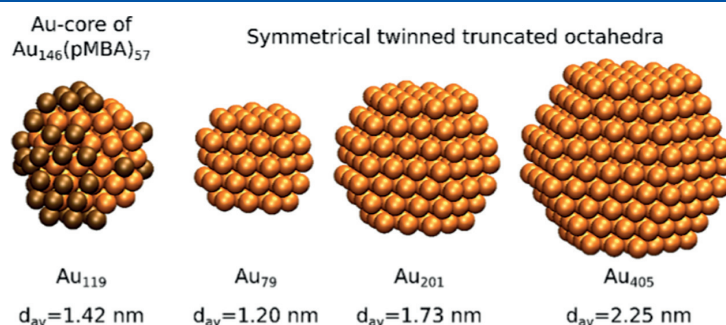

Figure 7. Range for possible basis for a metal core structure in twinned fcc octahedral arrangement. Orange color represents gold atoms and brown color represents the additional layer of atoms on top of symmetrical Au79 (left) representing together the Au-core of $Au_{146}(pMBA)_{57}$.
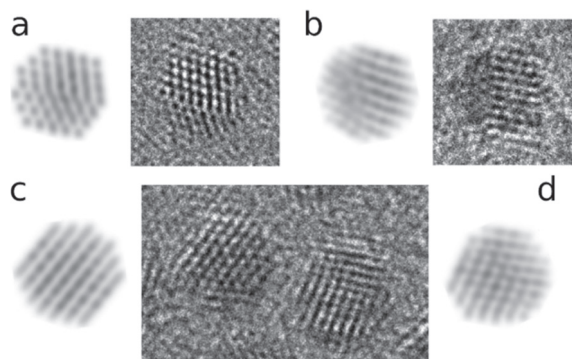
Figure 8. Comparison of HR-TEM images of Au250 and simulated images of the Au201 metal core from different directions.

core is visible in the HR-TEM images. Simulated HR-TEM images and experimental equivalents (Figure 8a,b,d) show the effects that are reproducible only with the stacking fault defect for fcc symmetry. Nevertheless, the symmetry found from powder XRD and HR-TEM are the same, which indicates that the core structure will remain the same under electron beam.

3.4. Predicting Molecular Composition. There is enough complementary experimental information for attempting the determination of the molecular composition of the investigated clusters. Herein, we provide computationally aided predictions for the molecular compositions by reflecting the measured results of the synthesized clusters to the properties of selected, structurally known, thiolate-protected clusters of a similar size. Selected known reference systems include clusters with a close to spherical shape such as $Au_{102}(pMBA)_{44}$, $Au_{146}(pMBA)_{57}$, $Au_{246}(SC_6H_4CH_3)_{80}$, and $Au_{271}(TBBT)_{84}$, matching the overall shape of the synthesized pMBA-protected particles. The clusters are selected from the size ranging from 100–300, including the two known pMBA-clusters. Due to the absence of experimentally resolved structures of larger size water-soluble clusters, we included two of the largest thiolate-protected clusters, despite them being protected with different types of aromatic ligands.

By assuming the pMBA-ligand for the selected known cluster compositions, trends of theoretical TG weight loss percentages can be predicted with respect to the number of Au atoms and the number of ligands as shown in Figure 9. Behavior shown in the figure is quite monotonous and by assuming that the behavior is valid also for the synthesized clusters, the composition $Au_{210}(pMBA)_{72}$ can be predicted for the smaller cluster. It is noteworthy that this composition would match perfectly with the magic electron shell closing of spherical clusters at 138 e, by assuming that gold provides 210 Au(6s)-based free electrons to the system and the Au-pMBA bonding withdraws 72 electrons out from the system.[46]

The second method for size estimation is based on the diameters of the clusters determined from the HR-TEM images, the probable sizes of the metal core of the clusters can be estimated computationally. Figure 10 shows the number of metal atoms as a function of diameter as calculated for the bare metal clusters of twinned fcc symmetry. Model clusters were generated as described in the Materials and Experimental Methods Section. Using the experimentally measured diameters, the two synthesized clusters have approximately 187 ± 30 and 385 ± 50 Au atoms in their metal cores based on the correlation shown in Figure 10. The number of metal atoms in
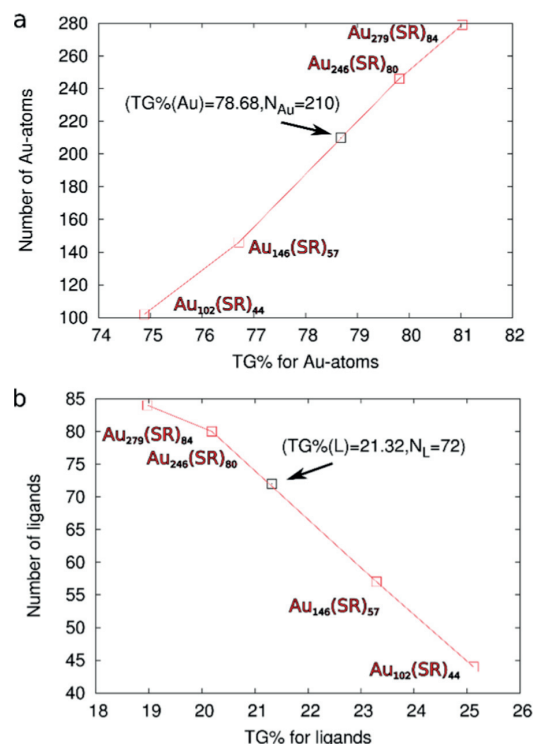

Figure 9. (a) Number of Au atoms in the thiolated clusters as a function of theoretically calculated thermogravimetric (TG) weight loss percentages of Au content. (b) Number of ligands in the thiolated clusters as a function of theoretically calculated ligand TG percentages. Both are drawn using the pMBA-ligand.

the Au−S interface varies from 23 to 40 in the case of the selected four known reference clusters. Assuming further that 30−40 Au atoms would participate in protecting units, the smaller synthesized particle would have approximately 220−230 Au atoms in total, depending on the actual Au−S interface conformation. Furthermore, we can estimate that at least 40 Au atoms should be contributing to the Au−S interface of the larger synthesized cluster increasing the size to >425 Au atoms in total.

Third, we did linear fitting on the properties of the selected known clusters. We correlated the diameter of the cluster including the metal core and the Au−S interface to the number of gold atoms in the cluster as shown in Figure 11a. We also correlated the number of ligands in the cluster to the spherical surface area as shown in Figure 11b. The two linear correlations can be used to predict the molecular composition by relying on experimentally measured diameters or on the estimated total number of gold atoms in the synthesized clusters.

For the smaller Au250 cluster, the size ranging from 210−230 Au atoms was already estimated to be realistic. Fixing the number of gold atoms to 210 gives a prediction of 2.1 nm diameter for the cluster (including the metal core and the Au−S interface) and further 71 ligands for the protecting layer. Both are in agreement with the experimentally measured results. For example, the 1.7 nm diameter of the metal core should be increased at maximum twice the Au−S bond (0.235 nm) when adding the metal−ligand interface. With the same
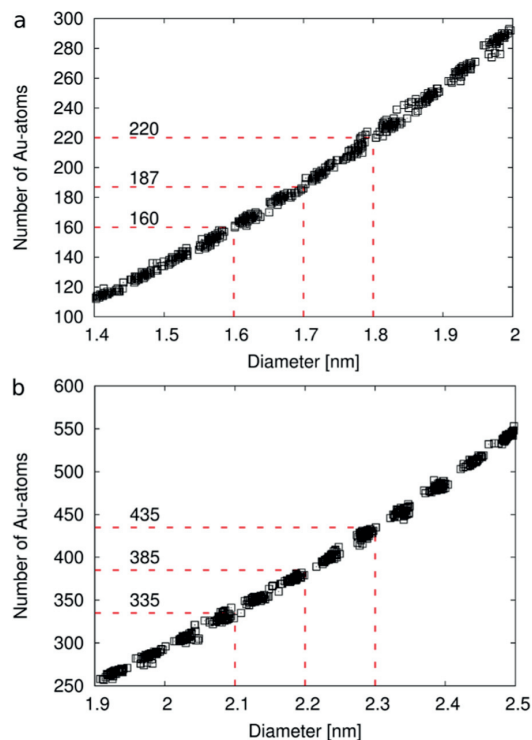
Figure 10. Number of Au atoms of the spherical bare twinned fcc Au-clusters in the size range relevant for the investigated *p*MBA-clusters in (a) and (b). The plausible sizes 187 and 385 of the metal core for the measured diameters are labeled in the figure. On the basis of the 0.1 nm error limits the minimum and maximum values are also given.

Figure 11. (a) Linear fitting done by correlating the number of Au atoms in the cluster to the diameter of the cluster taking into account the metal core and Au−S interface atoms and (b) by correlating the corresponding spherical surface area to the number of ligands. Fitted parameters: (a) $a = 0.328$ nm, $b = 0.129$ nm and (b) $a = 5.40$ nm^{-2}, $b = -2.02$. Diameters of the clusters are determined including the Au-core and the Au−S interface as described in the Materials and Experimental Methods Section.

procedure, the upper size limit for the number of gold atoms at 230 gives a prediction of 2.1 nm diameter and 75 ligands, for which the closest composition matching the measured TG percentages would be $Au_{230}(pMBA)_{80}$.

For the larger Au500 cluster, prediction of the molecular composition can be also made although the reliability is not equally good due to the lack of reference structures. For the larger cluster, we take the measured diameter 2.2 nm of the core and add to it approximately 0.4 nm from the metal−ligand interface. For the 2.6 nm spherical particle, correlations predict that the total number of Au atoms should be 429 and the number of ligands should be 113. Molecular composition would be $Au_{429}(SR)_{113}$, which has a very good match with the measured TG weight loss percentages. All the nearby compositions within 0.1 TG-percentage units from the measured results are included in compositions $Au_{426-442}(pMBA)_{112-115}$. The prediction of 426−442 gold atoms in total is reasonable compared to the estimated core size of 385 Au atoms, which would mean that 40−60 Au atoms were included in the protecting units. The number of single bridged ligands, not resembling a conformation of any protecting unit, increases in the Au−S interface as the cluster size increases. This can be realized by analyzing the structures of the known reference clusters $Au_{102}(SR)_{44}$, $Au_{146}(SR)_{57}$, $Au_{246}(SR)_{80}$, and $Au_{279}(SR)_{84}$. Their Au−S interfaces include respectively 0% (0/44), 12.3% (7/57), 12.5% (10/80), and 21.4% (18/84) of bridged ligands. At the same time the relative number of Au atoms in the Au−S interface decreases
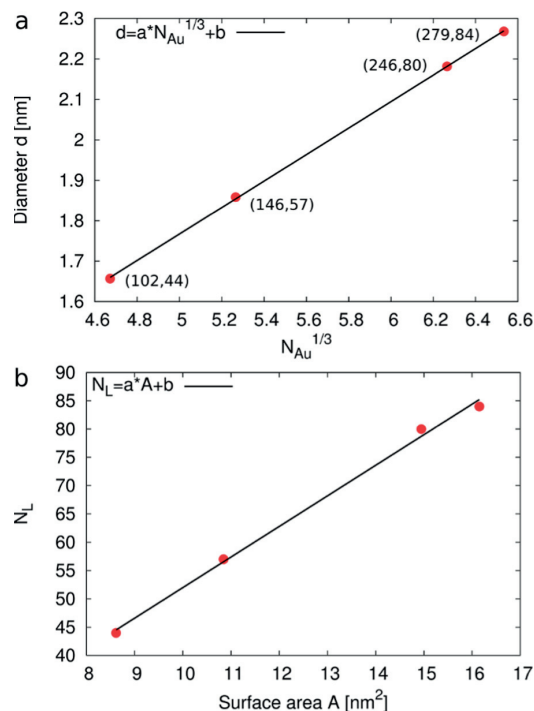
as the cluster size increases, at least within the represented size range.

As a summary, the best computationally aided predictions for the molecular compositions are $Au_{210-230}(pMBA)_{70-80}$ for the smaller cluster and $Au_{426-442}(pMBA)_{112-115}$ for the larger cluster.

4. CONCLUSIONS

In this work, we synthesized, in milligram scale, stable sizes of water-soluble *p*MBA-protected gold nanoclusters by controlling the pH in different MeOH/H$_2$O conditions. The products were carefully analyzed by various analytical techniques and characterized for approximate mass and structural composition. So far, water-soluble clusters have been observed in decahedral $(Au_{102}(pMBA)_{44})$,[45] fcc-like $(Au_{68}(mMBA)_{32}$ and $Au_{144}(mMBA)_n)$[38] and twinned fcc $(Au_{146}(pMBA)_{57})$ symmetries.[41] The results in this paper indicate that twinned fcc symmetry is favored in larger *p*MBA-protected clusters as shown in the case of Au250 and Au500. Combining all the experimental information and computational analysis, we came to the final prediction of the molecular composition of the synthesized clusters, namely $Au_{210-230}(pMBA)_{70-80}$ and $Au_{426-442}(pMBA)_{112-115}$. The structural knowledge of these clusters is crucial when applying these to biological studies. There is still a lack of well-defined, water-soluble particles, which could serve as universal labeling tools for bioimaging. Attaching gold nanoclusters to the biological systems will allow

the investigation of viruses, including their entry mechanism into cells. The development of cluster-based sensors by chemically modifying the ligand layer of the water-soluble gold nanoclusters is one of the possibilities to achieve controllable application in biosciences and to study, for example, the nature of viral genome release in cells (during infection). In addition, in the field of spectroscopy in physical chemistry, the plasmonic nanoclusters are important model systems to study the emergence of bulk properties in metal, and using them as building blocks could deepen the understanding of energy transfer processes, which are of interest in molecular electronics.

This work introduces some overall trends in synthetic methods and structural compositions for two larger water-soluble AuMPCs. These play a crucial role in understanding the relation of their diverse properties and increase the usability of gold nanoclusters.

■ ASSOCIATED CONTENT

⑤ Supporting Information

The Supporting Information is available free of charge on the ACS Publications website at DOI: 10.1021/acs.jpcc.8b11056.

> Detailed experimental procedures and methods for the prediction of molecular composition; PAGE gel showing a fractional precipitation procedure; TEM images taken from Au250 and Au500 nanoclusters; full spectrum of ^{1}H NMR of Au250 and Au500 nanoclusters; image of the residue after TG run (PDF)

■ AUTHOR INFORMATION

Corresponding Author

*E-mail: tanja.m.lahtinen@jyu.fi. Phone: +358 40805 3697.

ORCID ⊙

Manu Lahtinen: 0000-0001-5561-3259

Hannu Häkkinen: 0000-0002-8558-5436

Tanja Lahtinen: 0000-0002-1747-6959

Notes

The authors declare no competing financial interest.

■ ACKNOWLEDGMENTS

■ REFERENCES

(1) Salorinne, K.; Lahtinen, T.; Malola, S.; Koivistoa, J.; Häkkinen, H. Solvation Chemistry of Water-Soluble Thiol Protected Gold Nanocluster Au102 from DOSY NMR Spectroscopy and DFT Calculations. *Nanoscale* **2014**, *6*, 7823−7826.

(2) Plascencia-Villa, G.; Demeler, B.; Whetten, R. L.; Griffith, W. P.; Alvarez, M.; Black, D. M.; José-Yacamán, M. Analytical Characterization of Size-Dependent Properties of Larger Aqueous Gold Nanoclusters. *J. Phys. Chem. C* **2016**, *120*, 8950−8958.

(3) Jin, R. Atomically precise metal nanoclusters: stable sizes and optical properties. *Nanoscale* **2015**, *7*, 1549−1565.

(4) Marjomäki, V.; Lahtinen, T.; Martikainen, M.; Koivisto, J.; Malola, S.; Salorinne, K.; Pettersson, M.; Häkkinen, H. *Proc. Natl. Acad. Sci. U.S.A.* **2014**, *111*, 1277−1281.

(5) Homberger, M.; Simon, U. On the Application Potential of Gold Nanoparticles in Nanoelectronics and Biomedicine. *Philos. Trans. R. Soc., A* **2010**, *368*, 1405−1453.

(6) Nie, S.; Emory, S. R. Probing Single Molecules and Single Nanoparticles by Surface- Enhanced Raman Scattering. *Science* **1997**, *275*, 1102−1106.

(7) Brongersma, M. L.; Halas, N. J.; Nordlander, P. Plasmon-Induced Hot Carrier Science and Technology. *Nat. Nanotechnol.* **2015**, *10*, 25−34.

(8) Tapio, K.; Leppiniemi, J.; Shen, B.; Hytönen, V. P.; Fritzsche, W.; Toppari, J. J. Toward Single Electron Nanoelectronics Using Self-Assembled DNA Structure. *Nano Lett.* **2016**, *16*, 6780−6786.

(9) Martikainen, M.; Salorinne, K.; Lahtinen, T.; Malola, S.; Permi, P.; Häkkinen, H.; Marjomäki, V. Hydrophobic pocket targeting probes for enteroviruses. *Nanoscale* **2015**, *7*, 17457−17467.

(10) Stark, M. C.; Baikoghli, M. A.; Lahtinen, T.; Malola, S.; Xing, L.; Nguyen, M.; Nguyen, M.; Sikaroudi, A.; Marjomäki, V.; Häkkinen, H.; et al. Structural Characterization of Site-Modifed Nanocapsid with Monodispersed Gold Clusters. *Sci. Rep.* **2017**, *7*, No. 17048.

(11) Calard, F.; Wani, I. H.; Hayat, A.; Jarrosson, T.; Lère-Porte, J.-P.; Jafri, S. H. M.; Serein-Spirau, F.; Leifer, K.; Orthaber, A. Designing Sterically Demanding Thiolate Coated AuNPs for Electrical Characterization of BPDT in a NP−Molecule−Nanoelectrode Platform. *Mol. Syst. Des. Eng.* **2017**, *2*, 133−139.

(12) Häkkinen, H. The Gold-Sulfur Interface at the Nanoscale. *Nat. Chem.* **2012**, *4*, 443−455.

(13) Jin, R.; Zeng, C.; Zhou, M.; Chen, Y. Atomically Precise Colloidal Metal Nanoclusters and Nanoparticles: Fundamentals and Opportunities. *Chem. Rev.* **2016**, *116*, 10346−10413.

(14) Chakraborty, I.; Pradeep, T. Atomically Precise Clusters of Noble Metals: Emerging Link between Atoms and Nanoparticles. *Chem. Rev.* **2017**, *117*, 8208−8271.

(15) Sakthivel, N. A.; Theivendran, S.; Ganeshraj, V.; Oliver, A. G.; Dass, A. Crystal Structure of Faradaurate-279: $Au_{279}(SPh-tBu)_{84}$ Plasmonic Nanocrystal Molecules. *J. Am. Chem. Soc.* **2017**, *139*, 15450−15459.

(16) Kumara, C.; Zuo, X.; Ilavsky, J.; Chapman, K.-W.; Cullen, D.-A.; Dass, A. Super-Stable Highly Monodisperse Plasmonic Faradaurate-500 Nanocrystals with 500 Gold Atoms: $Au_{\sim500}(SR)_{\sim120}$. *J. Am. Chem. Soc.* **2014**, *136*, 7410−7417.

(17) Jin, R.; Qian, H.; Wu, Z.; Zhu, Y.; Zhu, M.; Mohanty, A.; Garg, N. Size Focusing: A Methodology for Synthesizing Atomically Precise Gold Nanoclusters. *J. Phys. Chem. Lett.* **2010**, *1*, 2903−2910.

(18) Qian, H.; Zhu, Y.; Jin, R. Size-Focusing Synthesis, Optical and Electrochemical Properties of Monodisperse $Au_{38}(SC_2H_4Ph)_{24}$ Nanoclusters. *ACS Nano* **2009**, *3*, 3795−3803.

(19) Qian, H.; Zhu, Y.; Jin, R. Atomically Precise Gold Nanocrystal Molecules with Surface Plasmon Resonance. *Proc. Natl. Acad. Sci. U.S.A.* **2012**, *109*, 696−700.

(20) Qian, H.; Jin, R. Ambient Synthesis of $Au_{144}(SR)_{60}$ Nanoclusters in Methanol. *Chem. Mater.* **2011**, *23*, 2209−2217.

(21) Schaaff, T.; Whetten, R. Controlled Etching of Au:SR Cluster Compounds. *J. Phys. Chem. B* **1999**, *103*, 9394−9396.

(22) Dharmaratne, A. C.; Krick, T.; Dass, A. Nanocluster Size Evolution Studied by Mass Spectrometry in Room Temperature $Au_{25}(SR)_{18}$ Synthesis. *J. Am. Chem. Soc.* **2009**, *131*, 13604−13605.

(23) Negishi, Y.; Nakazaki, T.; Malola, S.; Takano, S.; Niihori, Y.; Kurashige, W.; Yamazoe, S.; Tsukuda, T.; Häkkinen, H. A Critical Size for Emergence of Nonbulk Electronic and Geometric Structures in Dodecanethiolate-Protected Au Clusters. *J. Am. Chem. Soc.* **2015**, *137*, 1206−1212.

(24) Yi, C.; Zheng, H.; Tvedte, L. M.; Ackerson, C. J.; Knappenberger, K. L. J. Nanometals: Identifying the Onset of Metallic Relaxation Dynamics in Monolayer-Protected Gold Clusters Using Femtosecond Spectroscopy. *J. Phys. Chem. C* **2015**, *119*, 6307−6313.

(25) Lahtinen, T.; Hulkko, E.; Sokołowska, K.; Tero, T.-R.; Saarnio, V.; Lindgren, J.; Pettersson, M.; Häkkinen, H.; Lehtovaara, L.

Covalently Linked Multimers of Gold Nanoclusters Au$_{102}$(pMBA)$_{44}$ and Au ~$_{250}$ (pMBA)$_n$. *Nanoscale* **2016**, *8*, 18665−18674.

(26) Yampolsky, S.; Fishman, D. A.; Dey, S.; Hulkko, E.; Banik, M.; Potma, E. O.; Apkarian, V. A. Seeing a Single Molecule Vibrate Through Time-Resolved Coherent Anti-Stokes Raman Scattering. *Nat. Photonics* **2014**, *8*, 650−656.

(27) Sels, A.; Salassa, G.; Cousin, F.; Lee, L.-T.; Bürgi, T. Covalently Bonded Multimers of Au$_{25}$(SBut)$_{18}$ as a Conjugated System. *Nanoscale* **2018**, *10*, 12754−12762.

(28) Schaaff, T.; Knight, G.; Shafigullin, M.; Borkman, R.; Whetten, R. Isolation and Selected Properties of a 10.4 kDa Gold:Glutathione Cluster Compound. *J. Phys. Chem. B* **1998**, *102*, 10643−10646.

(29) Schaaff, T.; Whetten, R. Controlled Etching of Au:SR Cluster Compounds. *J. Phys. Chem. B* **1999**, *103*, 9394−9396.

(30) Dass, A. Faradaurate Nanomolecules: A Superstable Plasmonic 76.3 kDa Cluster. *J. Am. Chem. Soc.* **2011**, *133*, 19259−19261.

(31) Alvarez, M. M.; Chen, J.; Plascencia-Villa, G.; Black, D. M.; Griffith, W. P.; Garzon, I. L.; Jose-Yacaman, M.; Demeler, B.; Whetten, R. L. Hidden Components in Aqueous "Gold-144" Fractionated by PAGE: High-Resolution Orbitrap ESI-MS Identifies the Gold-102 and Higher All-Aromatic Au-pMBA Cluster Compounds. *J. Phys. Chem. B* **2016**, *120*, 6430−6438.

(32) Plascencia-Villa, G.; Demeler, B.; Whetten, R. L.; Griffith, W. P.; Alvarez, M.; Black, D. M.; Jose-Yacaman, M. Analytical Characterization of Size-Dependent Properties of Larger Aqueous Gold Nanoclusters. *J. Phys. Chem. C* **2016**, *120*, 8950−8958.

(33) Tvedte, L. M.; Ackerson, C. J. Size-Focusing Synthesis of Gold Nanoclusters with p-Mercaptobenzoic Acid. *J. Phys. Chem. A* **2014**, *118*, 8124−8128.

(34) Levi-Kalisman, Y.; Jadzinsky, P. D.; Kalisman, N.; Tsunoyama, H.; Tsukuda, T.; Bushnell, D. A.; Kornberg, R. D. Synthesis and Characterization of Au$_{102}$(pMBA)$_{44}$ Nanoparticles. *J. Am. Chem. Soc.* **2011**, *133*, 2976−2982.

(35) Ackerson, C. J.; Jadzinsky, P. D.; Sexton, J. Z.; Bushnell, D. A.; Kornberg, R. D. Synthesis and Bioconjugation of 2 and 3 nm-Diameter Gold Nanoparticles. *Bioconjugate Chem.* **2010**, *21*, 214−218.

(36) Wong, O. A.; Compel, W. S.; Ackerson, C. J. Combinatorial Discovery of Cosolvent Systems for Production of Narrow Dispersion Thiolate-Protected Gold Nanoparticles. *ACS Comb. Sci* **2015**, *17*, 11−18.

(37) Azubel, M.; Kornberg, R. D. Synthesis of Water-Soluble, Thiolate-Protected Gold Nanoparticles Uniform in Size. *Nano Lett.* **2016**, *16*, 3348−3351.

(38) Azubel, M.; Koivisto, J.; Malola, S.; Bushnell, D.; Hura, G. L.; Koh, A.-L.; Tsunoyama, H.; Tsukuda, T.; Pettersson, M.; Häkkinen, H.; et al. Electron Microscopy of Gold Nanoparticles at Atomic Resolution. *Science* **2014**, *345*, 909−912.

(39) Tero, T.-R.; Malola, S.; Koncz, B.; Pohjolainen, E.; Lautala, S.; Mustalahti, S.; Permi, P.; Groenhof, G.; Pettersson, M.; Häkkinen, H. Dynamic Stabilization of the Ligand−Metal Interface in Atomically Precise Gold Nanoclusters Au$_{68}$ and Au$_{144}$ Protected by *meta*-Mercaptobenzoic Acid. *ACS Nano* **2017**, *11*, 11872−11879.

(40) Azubel, M.; Koh, A.-L.; Koyasu, K.; Tsukuda, T.; Kornberg, R.-D. Structure Determination of a Water-Soluble 144-Gold Atom Particle at Atomic Resolution by Aberration-Corrected Electron Microscopy. *ACS Nano* **2017**, *11*, 11866−11871.

(41) Vergara, S.; Lukes, D. A.; Martynowycz, M. W.; Santiago, U.; Plascencia-Villa, G.; Weiss, S. C.; Cruz, M. J.; Black, D. M.; Alvarez, M. M.; López-Lozano, X.; et al. MicroED Structure of Au$_{146}$(pMBA)$_{57}$ at Subatomic Resolution Reveals a Twinned fcc Cluster. *J. Phys. Chem. Lett.* **2017**, *8*, 5523−5530.

(42) Sokolowska, K.; Hulkko, E.; Lehtovaara, L.; Lahtinen, T. Dithiol-Induced Oligomerization of Thiol-Protected Gold Nanoclusters. *J. Phys. Chem. C* **2018**, *122*, 12524−12533.

(43) International Centre for Diffraction Data, ICDD-PDF4+. http://www.icdd.com/ (accessed Dec 10, 2018).

(44) Lopez-Acevedo, O.; Akola, J.; Whetten, R. L.; Grönbeck, H.; Häkkinen, H. Structure and Bonding in the Ubiquitous Icosahedral Metallic Gold Cluster Au$_{144}$(SR)$_{60}$. *J. Phys. Chem. C* **2009**, *113*, 5035−5038.

(45) Jadzinsky, P. D.; Calero, G.; Ackerson, C. J.; Bushnell, D. A.; Kornberg, R. D. Structure of a Thiol Monolayer-Protected Gold Nanoparticle at 1.1 Å Resolution. *Science* **2007**, *318*, 430−433.

(46) Walter, M.; Akola, J.; Lopez-Acevedo, O.; Jadzinsky, P.-D.; Calero, G.; Ackerson, C.-J.; Whetten, R.-L.; Grönbeck, H.; Häkkinen, H. A Unified View of Ligand-Protected Gold Clusters as Superatom Complexes. *Proc. Natl. Acad. Sci. U.S.A.* **2008**, *105*, 9157−9162.

IV

CHEMICALLY SELECTIVE IMAGING OF INDIVIDUAL BONDS THROUGH SCANNING ELECTRON ENERGY LOSS SPECTROSCOPY: DISULFIDE BRIDGES LINKING GOLD NANOCLUSTERS

by

Karolina Sokołowska, Zhongyue Luan, Eero Hulkko, Christoph Rameshan, Noelia Barrabés, Vartkess Ara Apkarian and Tanja Lahtinen

Submitted manuscript

Request copy from the author